
RiverMamba: A State Space Model for Global River Discharge and Flood Forecasting

Mohamad Hakam Shams Eddin Juergen Gall

Institute of Computer Science, University of Bonn
Lamarr Institute for Machine Learning and Artificial Intelligence
{shams, gall}@iai.uni-bonn.de

Yikui Zhang Stefan Kollet

Institute of Bio- and Geosciences Agrosphere (IBG-3), Research Centre Jülich
Centre for High-Performance Scientific Computing in Terrestrial Systems,
Geoverbund ABC/J, Jülich
{yik.zhang, s.kollet}@fz-juelich.de

Abstract

Recent deep learning approaches for river discharge forecasting have improved the accuracy and efficiency in flood forecasting, enabling more reliable early warning systems for risk management. Nevertheless, existing deep learning approaches in hydrology remain largely confined to local-scale applications and do not leverage the inherent spatial connections of bodies of water. Thus, there is a strong need for new deep learning methodologies that are capable of modeling spatio-temporal relations to improve river discharge and flood forecasting for scientific and operational applications. To address this, we present RiverMamba, a novel deep learning model that is pretrained with long-term reanalysis data and that can forecast global river discharge and floods on a 0.05° grid up to 7 days lead time, which is of high relevance in early warning. To achieve this, RiverMamba leverages efficient Mamba blocks that enable the model to capture global-scale channel network routing and enhance its forecast capability for longer lead times. The forecast blocks integrate ECMWF HRES meteorological forecasts, while accounting for their inaccuracies through spatio-temporal modeling. Our analysis demonstrates that RiverMamba delivers reliable predictions of river discharge, including extreme floods across return periods and lead times, surpassing both operational AI- and physics-based models.

1 Introduction

Riverine floods are one of the most destructive natural disasters, with their risk anticipated to rise in the future as a result of climate change and socioeconomic developments [1–5]. River floods arise from compound effects, including atmospheric conditions like heavy precipitation caused by circulation patterns and snowmelt succeeding high temperature, all shaped by the specific characteristics of the river drainage area [6]. The interaction of these elements influences flood timing, scale, and severity [6]. This complexity complicates future flood risk assessment, as a changing climate may alter these drivers in unpredictable ways [7]. Therefore, early prediction of flood risk, especially for extreme floods, is a key measure for effective flood risk mitigation [8, 9].

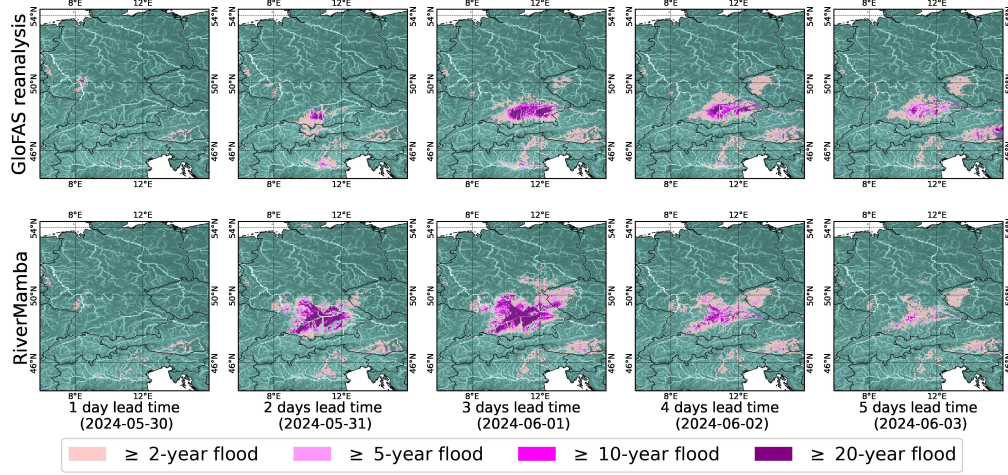


Figure 1: Example of a 5-day forecast of river discharge and flood events. In early June 2024, a significant flood affected Southern Germany. While the top row shows the floods obtained from the GloFAS reanalysis, the bottom row shows the river discharge forecast by our approach. The severity of floods is categorized by the statistical flood return period, i.e., occurring every 10 years.

To support national forecasting initiatives, current operational flood early warning systems can forecast and disseminate river discharge in real-time and consequently, provide flood forecasts at different scales [10–12]. The discharge forecasts derived from these systems can be further processed using inundation models to create anticipated flooded areas [13, 14]. The Global Flood Awareness System (GloFAS) [15, 16], developed under the Copernicus Emergency Management Service (CEMS) and operated by the European Centre for Medium-Range Weather Forecasts (ECMWF), represents the cutting-edge physics-based model for real-time and worldwide hydrological forecasting. However, physics-based hydrological models are expensive to run and require extensive calibration to handle complex catchment characteristics. AI-based early warning systems are thus considered as vital tools to enhance climate risk resilience [17, 18] and to enable flood forecasting without requiring full physical process understanding [19, 20]. While deep-learning approaches for weather forecasting [21–23] have been investigated in recent years, very little work has been done for forecasting river discharge at the global scale since it is very challenging. It requires the combination of sparse gauged river observations with high-resolution land surface, re-analysis, and weather forecast data. Furthermore, floods occur rarely and the goal is to forecast floods of different severity as shown in Fig. 1. Recently, an LSTM-based model has been proposed [24]. While it achieves promising results, it forecasts floods only locally at sparse river basins and cannot provide dense maps as in Fig. 1. Furthermore, modeling spatial relations is very important since river discharge at points near connected bodies of water is highly correlated.

In this work, we propose the first deep learning approach for global river discharge and flood forecasting that is not only capable of forecasting at sparse gauged observation points, but also of forecasting accurate, high-resolution (0.05°) global river discharge maps. In order to deal with the sparseness of gauged river points and the computational complexity of modeling spatio-temporal relations at the global scale, our proposed RiverMamba leverages Mamba blocks, which are bidirectional state space models [25–28], and spatio-temporal forecast blocks. Using a specialized procedure to convert sampled points into 1D sequences, RiverMamba maintains a global receptive field, connecting the routing of the channel networks and the teleconnection of meteorological data globally. The forecast layers are further forced by high-resolution meteorological data (HRES) to generate medium-range river discharge forecasts up to 7 days lead time. To address uncertainty in the meteorological forcing, we built the forecast layers so that they can, for each catchment point, incorporate information about meteorological forcing from the neighboring points and throughout the temporal dimension. Thus, RiverMamba ensures a consistent forecast through space and time.

Our contributions can be summarized as follows:

- We introduce a novel Mamba-based approach, called RiverMamba, for global river discharge and flood forecasting. It is the first deep learning approach that is capable of providing maps

of global river discharge forecasting at 0.05° , and it introduces a novel methodology to hydrology. It is able to integrate sparse gauged observations, river attributes, high-resolution reanalysis data, and weather forecast. The efficient structure allows to model spatio-temporal relations at global scale.

- We evaluate RiverMamba on both long-term real-world reanalysis and observational data. RiverMamba outperforms state-of-the-art AI- and physics-based operational systems for global flood forecasting.

2 Related works

Flood forecasting. Conventionally, floods can be categorized into three main types; first type is the *Fluvial* or *riverine flood* [29]. It occurs when the water level in a stream rises and overflows onto the adjacent land. The second type is *coastal flood*, also known as storm surges [30]; third is *Pluvial flood*, often referred to as *flash flood* [31–33] that can occur i.e., with extreme rainfalls. Machine learning (ML) has become a solid bedrock field for the development of hydrological simulation and flood models [34, 35]. Each type of flood has unique drivers and impacts. Consequently, ML methods require different strategies to forecast them. Related tasks to flood forecasting are urban flood modeling [36–39], flood inundation [40, 41], and flood extension and susceptibility mapping [42–45]. In this work, we are interested in forecasting riverine floods (fluvial) based on river discharge.

River discharge forecasting. River discharge can be used to detect fluvial flood signals when the magnitude of the flow exceeds certain thresholds. Current deep learning methods for forecasting river discharge are primarily based on locally lumped models [46, 47], hypothesizing that a single model can generalize across many catchments without considering the spatial-temporal information over grids [48]. The dominating backbone is the LSTM model [49] which is used in most recent studies such as EA-LSTM [50, 51], ED-LSTM [52, 53], Hydra-LSTM [54], MC-LSTM [55], and MF-LSTM [56]. That is, these models learn features specific to individual rivers or entities and lack spatial and topological information. However, river networks have spatio-temporal causal relations [57]. Only a few studies diverged from this conventional modeling and proposed to model the network topology with Graph Neural Networks [58, 59]. However, they were limited to small scales and in most cases, the graph model failed to capture topological information [58]. Moreover, the relations that can be learned from a graph are not dynamic and are fixed by the graph definition. Others applied an LSTM model on a coarse grid to estimate runoff and then coupled it with a river routing model to produce daily discharge at coarse resolution [60]. The most relevant work to us is the Encoder-Decoder LSTM [50] developed for the Google global operational forecasting system [24], which is a locally lumped model. In our work, distinct from previous works, we aim toward developing a vision based model that is able to forecast medium-range river discharge at grid-scale and with higher accuracy.

State space model (SSMs) and the Mamba family. Linear SSMs [25] and structured SSMs (S4) [26] and (S5) [27] were primarily introduced to handle long-sequence modeling in NLP. Recently, Mamba [28] introduced the selective scan mechanism, enabling efficient training and linear-time inference. Built upon Mamba, VMamba [61] and Vim [62] in the vision domain were introduced as appealing alternatives to the quadratic complexity of Vision Transformer [63] while improving scaling efficiency on long token sequences. A series of works were then conducted for tasks like image generation [64, 65], image classification [66, 67], video understanding [68, 69], motion generation [70], dense action anticipation [71], and point cloud processing [72, 73]. In this work, we model river points as one sequence and apply SSM Mamba to connect the routing of channel networks globally.

3 RiverMamba

In this work, we present the first deep learning approach that not only forecasts flood events at sparse gauged river observations, but that is capable of forecasting accurate, high-resolution (i.e., at 0.05°) maps of river discharge up to few days at global scale, as shown in Figs. 1 and 2. These maps are essential to forecast flood events of various severity like a flood that re-occurs statistically within a 1.5-year return period or a ‘flood of the century’. This is very challenging since it requires a model that models spatial-temporal relations in an efficient way and integrates different sources of data (Fig. 2).

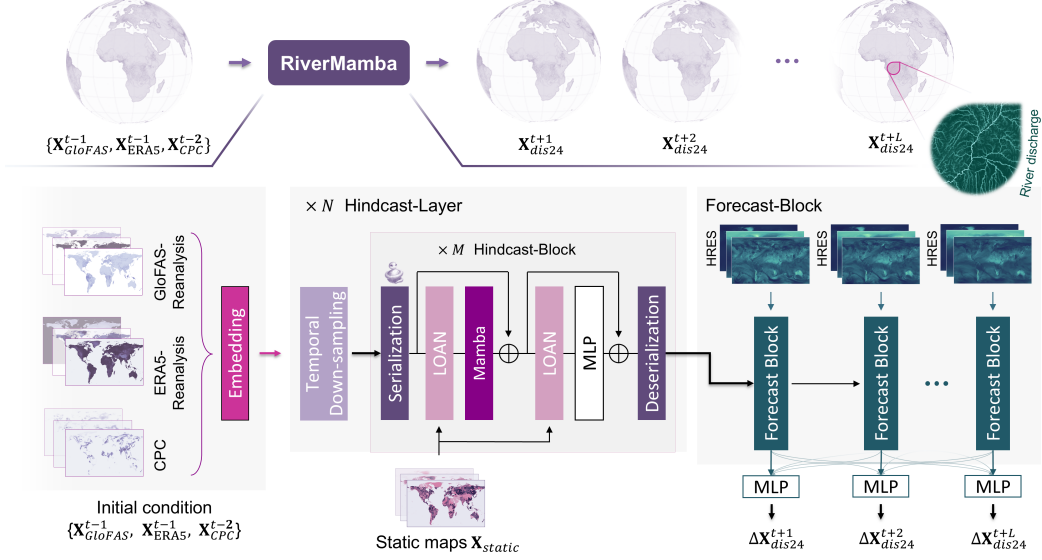


Figure 2: An overview of the proposed RiverMamba model for river discharge forecasting. The model forecasts at time t , high-resolution river discharge maps $\mathbf{X}_{dis24}^{t+1:t+L}$ from initial conditions ($\mathbf{X}_{ERA5}^{t-T:t-1}$, $\mathbf{X}_{GloFAS}^{t-T:t-1}$, $\mathbf{X}_{CPC}^{t-T:t-2}$), static river attributes (\mathbf{X}_{static}), and meteorological forecasts ($\mathbf{X}_{HRES}^{t+1:t+L}$).

As input, we use the initial condition of the forecasts from ERA5-Land reanalysis [74], denoted by $\mathbf{X}_{ERA5}^{t-T:t-1} = \{\mathbf{X}_{ERA5}^{t-T}, \dots, \mathbf{X}_{ERA5}^{t-2}, \mathbf{X}_{ERA5}^{t-1}\}$, the initial condition $\mathbf{X}_{GloFAS}^{t-T:t-1}$ from the GloFAS reanalysis data [75], and the initial condition $\mathbf{X}_{CPC}^{t-T:t-2}$ from the operational global unified gauge-based analysis of daily precipitation [76–78]. We also include data from weather forecasts, where we use the high-resolution meteorological forcing forecasts $\mathbf{X}_{HRES}^{t+1:t+L}$ from the ECMWF Integrated Forecast System (IFS), where L is the lead time for the forecast. We generate the river discharge forecast at t , using 00:00 UTC as reference time, for $t+1$ until $t+L$. This means that we do not address nowcasting but only forecasting as it is more relevant. We also do not include any nowcasts (\mathbf{X}_{HRES}^t) as input. To ensure that we do not include any data after 00:00 UTC and thus mimic a realistic deployment of RiverMamba, we shift \mathbf{X}_{GloFAS} and \mathbf{X}_{ERA5} by -1 day and \mathbf{X}_{CPC} by -2 days. Additionally, we include river attributes \mathbf{X}_{static} like catchment morphology from LISFLOOD [79]. The input variables are described in details in the suppl. material.

Given these inputs, RiverMamba forecasts changes of the daily mean river discharge $\Delta \mathbf{X}_{dis24}^{t+1:t+L}$ relative to the daily mean river discharge at $t-1$, i.e., \mathbf{X}_{dis24}^{t-1} . The forecast daily mean river discharge is thus given by $\mathbf{X}_{dis24}^{t+l} = \mathbf{X}_{dis24}^{t-1} + \Delta \mathbf{X}_{dis24}^{t+l}$.

An overview of RiverMamba is shown in Fig. 2. For training, we sample P points that are on the land surface and near water bodies. The details are described in the suppl. material. For each point p , we obtain a temporal sequence of embedding vectors $\mathbf{X}_{embed}^{t-T:t-1}(p)$:

$$\mathbf{X}_{embed}^t(p) = \text{LN}\left(\text{Tanh}\left(\text{Concat}\left(\text{Linear}(\mathbf{X}_{ERA5}^t(p)), \text{Linear}(\mathbf{X}_{GloFAS}^t(p)), \text{Linear}(\mathbf{X}_{CPC}^{t-1}(p))\right)\right)\right), \quad (1)$$

where LN is the layer norm and Linear is the projection layer. The dimensions of the input are $\mathbf{X}_{ERA5} \in \mathbb{R}^{B \times T \times P \times V_e}$, $\mathbf{X}_{GloFAS} \in \mathbb{R}^{B \times T \times P \times V_g}$, and $\mathbf{X}_{CPC} \in \mathbb{R}^{B \times T \times P \times 1}$, where B is the batch size, V_e is the number of variables from ERA5, and V_g is the number of variables from GloFAS. The embedding $\mathbf{X}_{embed} \in \mathbb{R}^{B \times T \times P \times K}$, where $K = 192$ is the dimensionality of the embedding, is then the input to the encoder defined by the hindcast layers.

The hindcast layers model spatio-temporal relations and aggregate the observations over time such that the output of the last hindcast layer $\mathbf{X}_{hindcast} \in \mathbb{R}^{B \times 1 \times P \times K}$ has a temporal resolution of $T = 1$, where the temporal resolution is down-sampled by a factor of 2 with a linear layer at the beginning of each hindcast layer, except for the 1st layer which processes the full temporal resolution. The hindcast layers further integrate the static river attributes \mathbf{X}_{static} that contain additional information

like catchment morphology, which is relevant for flood forecasting. While we analyze the impact of the different inputs, in particular the river attributes, in the suppl. material, another key aspect of the hindcast blocks is the specialized serialization of the spatio-temporal points and the Mamba blocks [28, 61, 62]. The serialization defines the way the sampled points are connected, and the Mamba block efficiently updates the features of each point based on the spatio-temporal structure. This is a very important design choice since transformer blocks are computationally infeasible for global flood forecasting, whereas [24] does not consider spatial relations at all. In the suppl. material, we also show that an alternative using Flash-Attention [80, 81] is inferior in terms of inference time and accuracy compared to our approach.

The output of the last hindcast layer is then processed along with the HRES meteorological forcing by forecast blocks, and MLP-based regression heads predict for each lead time l the difference of daily mean river discharge $\Delta \mathbf{X}_{dis24}^{t+l}$ with respect to the daily mean river discharge at $t-1$. In the following, we describe the components of RiverMamba in details.

Hindcast block. As shown in Fig. 2, the hindcast block has three main components: serialization and deserialization, location-aware adaptive normalization layers (LOAN) to integrate static river attributes, and the Mamba block.

Serialization. The serialization defines the spatio-temporal scanning path over all sampled points for the following Mamba block. For this, we propose space-filling curves that sequentially traverse through all points. The concept was introduced in [82] and the space-filling can be defined as a bijective function $\Phi : \mathbb{Z}^3 \rightarrow \mathbb{N}$, where every point in the discrete space corresponds to a unique index within the sequence. We call this mapping the serialized encoding. The serialized decoding is done as $\Phi^{-1} : \mathbb{N} \rightarrow \mathbb{Z}^3$, where every index is mapped back into its corresponding position. We call this deserialization. We investigated three curves: the Generalized Hilbert (Gilbert) curve, which is a generalized version of the Hilbert curve [83], as well as the Sweep and Zigzag curves in vertical and horizontal directions. Examples of space-filling curves in 2D are illustrated in Fig. 3. As shown in the suppl. material, a combination of Sweep and Gilbert curves performs best. To this end, each hindcast block has its own curve. As shown in Fig. 3, we sweep in the first block over the horizontal direction. The spatial curves are connected over time by continuing the last point of the curve at t with the first point of the curve at $t+1$. The second block then sweeps over the vertical direction and we continue with the Gilbert curve and its transposed. These four space-filling curves are iterated. By altering the curves sequentially through the hindcast blocks, the sampled points will be connected and scanned from diverse spatial perspectives, enabling RiverMamba to capture different contextual features.

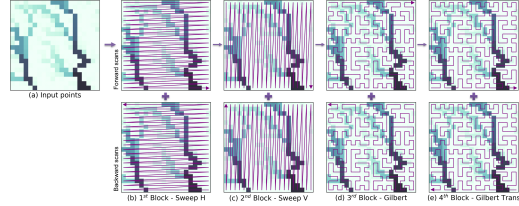


Figure 3: Illustration of the spatial scans in RiverMamba. Larger images are in the suppl. material.

Location-aware adaptive normalization layer. In order to condition the model on static river attributes \mathbf{X}_{static} , the location-aware adaptive normalization layer (LOAN) [84] modulates the features \mathbf{X} within the hindcast block:

$$\text{LOAN}(\mathbf{X}) = \left(\frac{\mathbf{X} - \mu}{\sigma} \right) + \text{GELU}(\text{Linear}(\mathbf{X}_{static})), \quad (2)$$

where a linear layer projects $\mathbf{X}_{static} \in \mathbb{R}^{B,1,P,V_s}$, with V_s being the number of static variables, to $\mathbb{R}^{B,1,P,K}$. $\mu \in \mathbb{R}^{B,T,P,1}$ and $\sigma \in \mathbb{R}^{B,T,P,1}$ are the mean and standard deviation of \mathbf{X} along the channel dimension, respectively, and $\mathbf{X} \in \mathbb{R}^{B,T,P,K}$ is the input to the LOAN layer. The layer normalizes the features and adds a systematic bias based on the attributes. For instance, the features are normalized and biased based on location attributes that have an impact on drainage and floods.

Mamba block. Fig. 4 shows a more detailed structure of the hindcast block with the elements of the Mamba block. After the input is serialized into a 1D sequence based on the block-specific space-filling curve and the features are normalized by the LOAN layer, the Mamba block processes the features of the sampled points along the sequence.

The Mamba block is based on a state-space model that transform a 1D sequence of states $x(t)$ into another representation $y(t)$ through an implicit hidden latent state $h(t)$ and a first-order ordinary

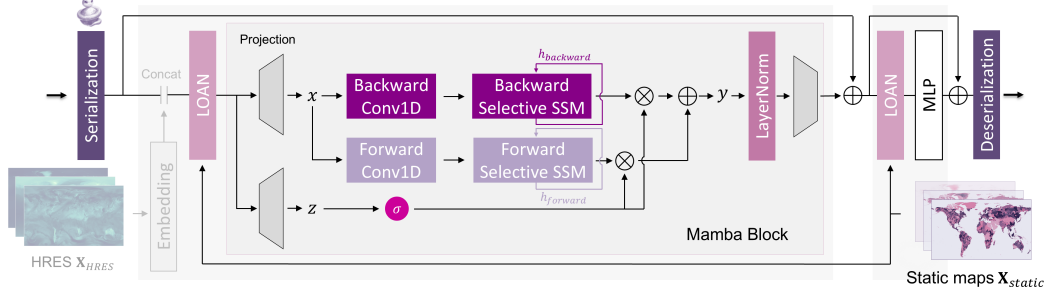


Figure 4: The structure of the hindcast block and forecast block. Both use a bidirectional Mamba block and the forecast block has the same structure as the hindcast block, but it additionally incorporates meteorological forecasts HRES by concatenation. The forecast block also includes LOAN layers although it is not shown in Fig. 2

differential equation:

$$h'(t) = \mathbf{A}h(t-1) + \mathbf{B}x(t), \quad y(t) = \mathbf{C}h(t) + \mathbf{D}x(t). \quad (3)$$

To integrate Eq. (3) into a deep learning framework, S4 [26] parametrized the system with the matrices $(\mathbf{A}, \mathbf{B}, \mathbf{C}, \mathbf{D})$ and discretized it with a timescale parameter Δ :

$$h_t = \bar{\mathbf{A}}h_{t-1} + \bar{\mathbf{B}}x_t, \quad y_t = \mathbf{C}h_t + \mathbf{D}x_t, \quad (4)$$

$$\bar{\mathbf{A}} = e^{(\Delta\mathbf{A})}, \quad \bar{\mathbf{B}} = (\Delta\mathbf{A})^{-1}(e^{(\Delta\mathbf{A})} - \mathbf{I})\Delta\mathbf{B}, \quad (5)$$

where $\bar{\mathbf{A}}$ and $\bar{\mathbf{B}}$ are the discretized versions of the system. Recently, S6 [28] proposed to make Eqs. (4) and (5) time-variant. To this end, the parameters $\mathbf{B}(x)$, $\mathbf{C}(x)$, and $\Delta(x)$ become dependent on the input state x . This representation of a state-space model is called Mamba, which is an efficient alternative to transformers [85], particularly when processing many points as in our case.

Fig. 4 illustrates the steps of the Mamba block. The normalized sequence $\mathbf{X} \in \mathbb{R}^{B \times (T \times P) \times K}$ is projected into $\mathbf{x} \in \mathbb{R}^{B \times (T \times P) \times K}$ and $\mathbf{z} \in \mathbb{R}^{B \times (T \times P) \times K}$, where $T \times P$ is the length of the sequence. Note that the order of the elements in the sequence depends on the serialization, which differs between the hindcast blocks. We use a bi-directional approach that converts \mathbf{x} into \mathbf{x}'_o using a forward and a backward 1-D causal convolution, where $o \in \{f, b\}$ denotes the forward or backward pass. For each direction, \mathbf{B}_o , \mathbf{C}_o , and Δ_o are obtained by projection layers from \mathbf{x}'_o , and \mathbf{A}_o and \mathbf{B}_o are computed using Eq. (5). The selective SSM then uses Eq. (4) to obtain $\mathbf{y}_{forward}$ and $\mathbf{y}_{backward}$ for the forward and backward pass, respectively. The final output \mathbf{y} is obtained by gating $\mathbf{y}_{forward}$ and $\mathbf{y}_{backward}$ via $\text{SiLU}(\mathbf{z})$ and adding them up. Finally, \mathbf{y} is normalized and projected back linearly to $\mathbb{R}^{B \times (T \times P) \times K}$. The complete algorithm for the Mamba block is described in the suppl. material.

After the Mamba block, the hindcast block includes another LOAN layer followed by an MLP. The final output \mathbf{X} is then deserialized at the end since the next hindcast block uses a different serialization.

Forecasting layer. While the hindcast layers encode the sequence of past input variables into a K -dimensional vector per sampled point, i.e., $\mathbf{X}_{hindcast} \in \mathbb{R}^{B \times 1 \times P \times K}$, the forecasting layers forecast the difference of daily mean river discharge $\Delta\mathbf{X}_{dis24}^{t+l}$ for each lead time l , using $\mathbf{X}_{hindcast}$ and meteorological forecasts $\mathbf{X}_{HRES}^{t+1:t+L}$ as input, as shown in Fig. 2. The forecast blocks have the same structure as the hindcast blocks except that the forecast block incorporates the meteorological forcing (HRES). This is done by projecting $\mathbf{X}_{HRES}^{t+1:t+L}$ with a linear layer to 64 dimensions, serializing it, and concatenating it with the input \mathbf{X} as illustrated in Fig. 4. The processing of HRES is done sequentially, i.e., we have L forecast blocks and the l -th forecast block processes \mathbf{X}_{HRES}^{t+l} . We argue that this design is crucial to ensure that the temporal relationships between the meteorological forcing and the initial conditions are maintained.

The output of all forecast blocks is processed by L regression heads implemented as multi-layer perceptrons (MLP) where the output for the lead time $t+l$ is obtained as:

$$\Delta\mathbf{X}_{dis24}^{t+l} = \text{Linear}\left(\text{ReLU}\left(\text{Concat}\left(\text{Linear}(\mathbf{X}_{forecast}^{t+l}), \text{Linear}(\mathbf{X}_{forecast}^{t+1:t+L \setminus t+l})\right)\right)\right), \quad (6)$$

where $\mathbf{X}_{forecast}^{t+l}$ are the features from the l -th forecast block and $\mathbf{X}_{forecast}^{t+1:t+L\setminus t+l}$ are the concatenated features from all forecast blocks except of the l -th block. The linear layers project the input $\mathbf{X}_{forecast}^{t+l}$ or $\mathbf{X}_{forecast}^{t+1:t+L\setminus t+l}$ to 32 dimensions and the last linear projection estimates finally $\Delta\mathbf{X}_{dis24}^{t+l} \in \mathbb{R}^{B \times 1 \times P \times 1}$.

Training. As already mentioned, we sample P points around the globe for training. As a target value for training, we first use the river discharge data from the GloFAS reanalysis as ground truth and then fine-tune on sparse observations using data from Global Runoff Data Centre (GRDC). We obtain the target values by $\Delta\hat{\mathbf{X}}_{dis24}^{t+l}(p) = \hat{\mathbf{X}}_{dis24}^{t+l}(p) - \hat{\mathbf{X}}_{dis24}^{t-1}(p)$, where $\hat{\mathbf{X}}$ are the values from GloFAS or GRDC. For the training loss, we propose a weighted version of the mean-squared error (MSE) loss:

$$\mathcal{L} = \frac{1}{B \times P \times L} \sum_{b=1}^B \sum_{p=1}^P \sum_{l=1}^L w^{b,t+l}(p) \|\Delta\hat{\mathbf{X}}_{dis24}^{b,t+l}(p) - \Delta\mathbf{X}_{dis24}^{b,t+l}(p)\|_2^2, \quad (7)$$

where B is the batch size. Since the severity of a flood is highly important for flood forecasting and severe floods occur rarely, the weighting factor $w^{b,t+l}(p)$ takes this into account. The severity of a flood is ranked by the statistical flood return period in years, which we denote by r and ranges from 1.5 to 500. The severity of a flood is thus given by $\hat{r}^{t+l}(p) = \max_r \left\{ r : \hat{\mathbf{X}}_{dis24}^{t+l}(p) \geq \theta_r(p) \right\}$, where θ_r is the statistical threshold for a given flood return period r . We also include the case $r=0$ with $\theta_r=0$ for defining events that are not floods. Using this notation, the weighting is thus given by

$$\hat{w}^{b,t+l}(p) = \begin{cases} \hat{r}^{b,t+l}(p) & \text{if } \hat{r}^{b,t+l}(p) > 1 \\ 1 & \text{otherwise.} \end{cases} \quad (8)$$

We thus weight the loss based on the flood return period if a flood occurred at location p and time $t+l$, and we use 1 if there has been no flood. We further weight the loss with $\hat{u}^{b,t+l} = e^{\alpha(L-l+1)}$, where we give a higher weight to a shorter lead time l and use $\alpha=0.25$. This compensates for the sequential structure of the forecast blocks where each forecast block takes the features of the previous block as input. The final weight is thus given by $w^{b,t+l}(p) = \hat{u}^{b,t+l} \hat{w}^{b,t+l}(p)$. Since river discharge exhibits a very large dynamic with varying orders of magnitude, we transform the discharge values by $\text{sign}(\Delta\hat{x}) \log(1 + |\Delta\hat{x}|)$. We evaluate the impact of the weighting and provide more details in the suppl. material. For inference, we can forecast floods for any set of points or densely as in Fig. 1.

4 Experimental results

We obtain data for river discharge from the ECMWF GloFAS reanalysis [75]. It is generated by forcing the LISFLOOD hydrological model [86] using meteorological data from ERA5 [87]. GloFAS reanalysis combines physics-based simulation with observations to generate a consistent reconstruction of the past. The dataset is provided as a daily averaged discharge on a global coverage at 3 arcmin grid (0.05°). We use the GloFAS reanalysis as a target discharge for training and testing the model in Sec. 4.1. The ablation studies are done using GloFAS reanalysis over Europe. In addition, we fine-tune and test the model on observational GRDC river discharge data in Sec. 4.2. Flood thresholds are determined using return periods for individual points and are calculated from the long-term data. The thresholds allow for the identification of a flood when the threshold is surpassed.

We evaluate the performance of RiverMamba on both GloFAS reanalysis and GRDC, where diagnostic GRDC stations are available (3366 stations). For evaluation, we use common metrics like the coefficient of determination (R2), Kling–Gupta efficiency (KGE), and the averaged F1-score for floods with return periods of $\{1.5 - 20\}$ years. We train on the years 1979-2018, validate on 2019-2020, and test on 2021-2024. All evaluation points are gauged stations and temporally out-of-sample. The metrics are calculated on the time series at single grid points and then averaged over all points.

We compare RiverMamba to persistence, climatology, and the state-of-the-art deep learning Encoder-Decoder LSTM of Google’s operational flood forecasting system [24]. For evaluation on GRDC observations, we additionally compare our approach to the reforecast version of the state-of-the-art operational GloFAS forecasting system operated by ECMWF [15, 16]. More details about dataset, evaluation metrics and baselines are provided in the suppl. material.

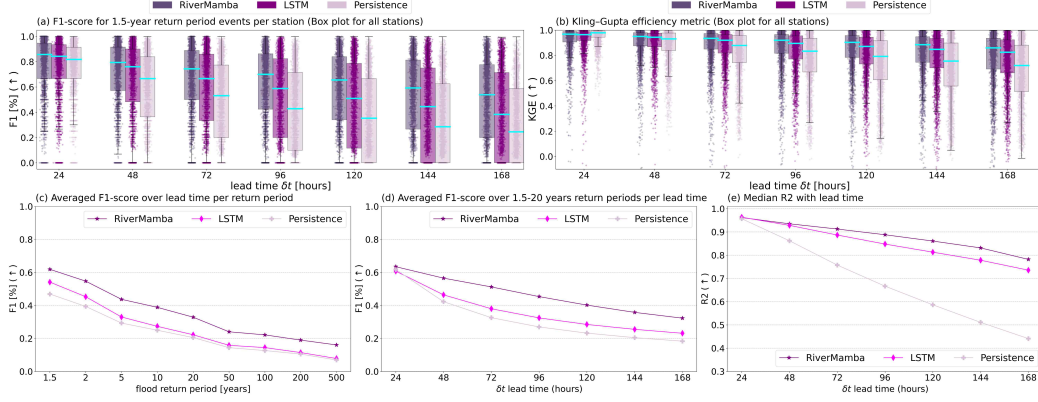


Figure 5: Results on GloFAS reanalysis across lead times and flood return periods.

Table 1: Results on GloFAS-Reanalysis. (\pm) denotes the standard deviation for 3 runs.

	Validation (2019-2020)			Test (2021-2024)		
Model	R2 (\uparrow)	KGE (\uparrow)	F1 (\uparrow)	R2 (\uparrow)	KGE (\uparrow)	F1 (\uparrow)
Climatology	11.75	26.18	—	13.52	24.49	—
Persistence	67.78	83.80	31.38	68.33	84.12	32.23
LSTM [24]	85.39 \pm 0.31	89.31 \pm 0.34	35.11 \pm 0.68	84.85 \pm 0.21	89.24 \pm 0.29	35.82 \pm 0.58
RiverMamba	88.03\pm0.43	91.37\pm0.26	45.40\pm0.56	87.28\pm0.13	91.25\pm0.08	45.89\pm0.80

4.1 Experiments on GloFAS river discharge Reanalysis

The quantitative results are shown in Table 1. As can be seen, the climatology baseline performs poorly, as the dynamic in local river discharge varies a lot over time, highlighting the difficulty in predicting flows. We therefore exclude it in Fig. 5 (a) that shows F1-score for floods with a 1.5-year return period and (b) KGE for river discharge for different lead times from 24 to 168 hours. The boxes show distribution quartiles and the evaluation points are represented as points along the y-axis. Fig. 5 (d) shows the F1-score averaged over return periods of 1.5 to 20 years and (e) shows the median R2 for river discharge. The persistence baseline predicts the future discharge as the same value of the discharge at time t . This achieves good prediction for the short-term forecast, however, the prediction skill drops with lead time. While LSTM [24] outperforms the persistence baseline, RiverMamba outperforms all baselines and methods on all metrics as shown in Table 1. In particular for lead times above 48 hours, the performance gap between RiverMamba and LSTM is large. We attribute this to the receptive field and the spatio-temporal modeling of RiverMamba. Fig. 5 (c) plots the F1-score averaged over 24 to 168 hours lead time for different flood return periods. The results show that RiverMamba outperforms the other approaches both for more frequent floods and rare severe floods that occur statistically only every 500 years. More results are in the suppl. material. In the following, we discuss a set of ablation studies that are not performed globally but over Europe.

Objective functions. In Table 2 (a), we evaluate the impact of the weighting factor in the loss (7), which is based on \hat{w} (8) and \hat{u} . The results show that both terms improve the results. \hat{w} is important to focus on rare and more severe floods. \hat{u} gives more weight to the forecast in the near future where \mathbf{X}_{HRES} is more reliable, which is important due to the sequential structure of the forecast module.

Table 2: Ablation studies on the validation set over Europe.

(a) Objective function		(b) Location Embedding			(c) Forecasting strategy			
\hat{w}	\hat{u}	KGE F1 (\uparrow)	LOAN _(hind)	LOAN _(forc)	KGE F1 (\uparrow)	S-HRES	T-HRES	KGE F1 (\uparrow)
\times	\times	90.86 22.36	\times	\times	91.83 27.90	\times	✓	88.62 20.30
✓	\times	91.27 28.59	✓	\times	91.60 28.27	✓	\times	88.69 22.68
✓	✓	92.05 28.75	✓	✓	92.05 28.75	✓	✓	92.05 28.75

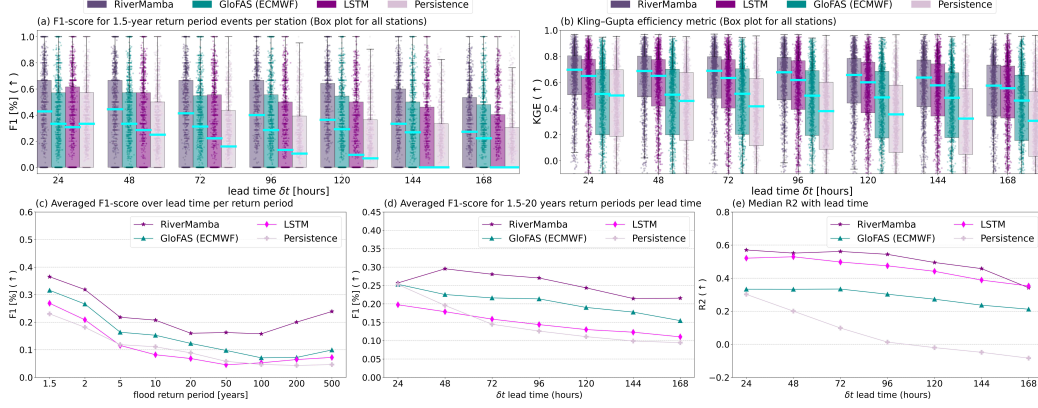


Figure 6: Results on gauged GRDC observations across lead times and flood return periods.

Table 3: Results on GRDC gauged stations. (\pm) denotes the standard deviation for 3 runs.

	Validation (2019-2020)			Test (2021-2023)		
Model	R2 (\uparrow)	KGE (\uparrow)	F1 (\uparrow)	R2 (\uparrow)	KGE (\uparrow)	F1 (\uparrow)
Climatology	-0.02	13.42	—	-0.13	08.70	—
Persistence	16.82	45.69	16.26	06.60	39.18	14.62
GloFAS [16]	37.13	54.12	21.35	28.92	49.44	20.44
LSTM [24]	54.37 \pm 0.25	65.72 \pm 0.10	17.24 \pm 0.17	46.15 \pm 0.39	61.41 \pm 0.18	14.75 \pm 0.14
RiverMamba	59.43 \pm 0.16	70.15 \pm 0.07	25.77 \pm 0.46	50.57 \pm 0.28	66.12 \pm 0.10	24.27 \pm 1.11

Location embedding. In Table 2 (b), we show the benefit of using LOAN. In the first row, we duplicate the static features along T dimension and concatenate them with the dynamic input. The performance becomes better with the proposed incorporation of the static river attributes in the hindcast (second row) and forecast (last row) blocks.

Forecasting strategy. Table 2 (c) evaluates the impact of spatio-temporal modeling in the forecast module. In the first row, we remove the spatial relations in the forecast module by replacing the forecast blocks by point-wise MLPs. In this way, the data is processed after the last hindcast layer temporally but not spatially. This makes the model unaware of the spatial biases in the meteorological forcing \mathbf{X}_{HRES} . The second row denotes a setup where the forecast blocks do not get the features from the previous forecast block (Fig. 2) but directly from the last hindcast layer. In this case, we forecast river discharge for each lead time independently. The results show that in both cases the performance drops compared to our approach (third row), demonstrating the importance of spatio-temporal modeling. More ablation studies can be found in the suppl. material.

4.2 Experiments on GRDC observational river discharge

Table 3 reports the performance on GRDC river discharge observations at gauged stations, which also includes the physics-based GloFAS reforecast model. As previously, Fig. 6 compares the forecast performance across multiple lead times and flood return periods. Compared to the results on GloFAS reanalysis (Table 1), all models show a noticeable drop in performance when evaluated on GRDC observations (Table 3). This decline likely stems from the fact that GloFAS simulates primarily naturalized discharge, with simplified representations of major reservoirs [75, 88], whereas GRDC reflects fully regulated flow, influenced by complex and unobserved human activities, such as dam operations and irrigation. This introduces biases that models cannot learn, especially in the absence of globally available data representing human water management, highlighting the challenge of predicting discharge under human-modified conditions. The results show that traditional baselines such as Climatology and Persistence perform poorly. GloFAS performs much better than the baselines, but the R2 and KGE values are rather low due to the mentioned differences of physics-based models and observations. RiverMamba consistently outperforms the other methods for all metrics. Notably,

RiverMamba shows less degradation in F1-score with increasing lead time, highlighting its strength in medium-range flood forecasting. More results are in the suppl. material.

5 Conclusions and limitations

We introduced RiverMamba, a novel deep learning approach for global, medium-range river discharge and flood forecasting. Due to its efficient structure and specialized scanning paths, RiverMamba maintains a global receptive field, while scaling linearly with respect to the number of sampled points. As a result, RiverMamba is capable of forecasting high-resolution (0.05°) global river discharge maps. Further, the spatio-temporal modeling of the forecast blocks incorporates meteorological forcing and ensures a consistent forecast through space and time. Our analysis reveals that RiverMamba outperforms operational state-of-the-art deep learning and physics-based models on both reanalysis and observational data. While the results show major advancements in river discharge and flood forecasting, the approach has some limitations. Observational data are affected by human interventions like dams and there is a need to integrate such interventions in the model. As it is the case for operational systems, floods are not always correctly forecast. The causes of the errors need to be analyzed more in detail. The forecast errors can be caused by human interventions, errors in the weather forecast for meteorological forcing or river attributes, the rarity of floods, or bias in the data and re-analysis. Given such errors, it is desirable to extend the model such that it estimates its uncertainty for the forecast as well. Besides these limitations, RiverMamba has the potential for an operational medium-range river discharge and flood forecasting system that predicts flood risks, in particular extreme floods, more accurately and at higher resolution than existing systems. This is essential for stakeholders to make decisions for an effective flood risk mitigation and an early warning system to protect citizens.

References

- [1] Francesco Dottori, Wojciech Szewczyk, Juan-Carlos Ciscar, Fang Zhao, Lorenzo Alfieri, Yukiko Hirabayashi, Alessandra Bianchi, Ignazio Mongelli, Katja Frieler, Richard A Betts, et al. Increased human and economic losses from river flooding with anthropogenic warming. *Nature Climate Change*, 8(9):781–786, 2018.
- [2] Bruno Merz, Günter Blöschl, Sergiy Vorogushyn, Francesco Dottori, Jeroen CJH Aerts, Paul Bates, Miriam Bertola, Matthias Kemter, Heidi Kreibich, Upmanu Lall, et al. Causes, impacts and patterns of disastrous river floods. *Nature Reviews Earth & Environment*, 2(9):592–609, 2021.
- [3] Heidi Kreibich, Anne F Van Loon, Kai Schröter, Philip J Ward, Maurizio Mazzoleni, Nivedita Sairam, Gita Wakbulcho Abeshu, Svetlana Agafonova, Amir AghaKouchak, Hafzullah Aksoy, et al. The challenge of unprecedented floods and droughts in risk management. *Nature*, 608(7921):80–86, 2022.
- [4] Jun Rentschler, Melda Salhab, and Bramka Arga Jafino. Flood exposure and poverty in 188 countries. *Nature communications*, 13(1):3527, 2022.
- [5] Myanna Lahsen and Jesse Ribot. Politics of attributing extreme events and disasters to climate change. *WIREs Climate Change*, 13(1):e750, 2022.
- [6] S. Jiang, E. Bevacqua, and J. Zscheischler. River flooding mechanisms and their changes in europe revealed by explainable machine learning. *Hydrology and Earth System Sciences*, 26(24):6339–6359, 2022.
- [7] Shijie Jiang, Larisa Tarasova, Guo Yu, and Jakob Zscheischler. Compounding effects in flood drivers challenge estimates of extreme river floods. *Science Advances*, 10(13):ead14005, 2024.
- [8] Florian Pappenberger, Hannah L. Cloke, Dennis J. Parker, Fredrik Wetterhall, David S. Richardson, and Jutta Thielen. The monetary benefit of early flood warnings in europe. *Environmental Science & Policy*, 51:278–291, 2015.
- [9] Gustau Camps-Valls, Miguel-Ángel Fernández-Torres, Kai-Hendrik Cohrs, Adrian Höhl, Andrea Castelletti, Aytac Pacal, Claire Robin, Francesco Martinuzzi, Ioannis Papoutsis, Ioannis Prapas, et al. Artificial intelligence for modeling and understanding extreme weather and climate events. *Nature Communications*, 16(1):1919, 2025.

- [10] Rebecca E. Emerton, Elisabeth M. Stephens, Florian Pappenberger, Thomas C. Pagano, Albrecht H. Weerts, Andy W. Wood, Peter Salamon, James D. Brown, Niclas Hjerdt, Chantal Donnelly, Calum A. Baugh, and Hannah L. Cloke. Continental and global scale flood forecasting systems. *WIREs Water*, 3(3):391–418, 2016.
- [11] H. A. P. Hapuarachchi, M. A. Bari, A. Kabir, M. M. Hasan, F. M. Woldemeskel, N. Gamage, P. D. Sunter, X. S. Zhang, D. E. Robertson, J. C. Bennett, and P. M. Feikema. Development of a national 7-day ensemble streamflow forecasting service for australia. *Hydrology and Earth System Sciences*, 26(18):4801–4821, 2022.
- [12] F. Dottori, M. Kalas, P. Salamon, A. Bianchi, L. Alfieri, and L. Feyen. An operational procedure for rapid flood risk assessment in europe. *Natural Hazards and Earth System Sciences*, 17(7):1111–1126, 2017.
- [13] S. Nevo, E. Morin, A. Gerzi Rosenthal, A. Metzger, C. Barshai, D. Weitzner, D. Voloshin, F. Kratzert, G. Elidan, G. Dror, G. Begelman, G. Nearing, G. Shalev, H. Noga, I. Shavitt, L. Yuklea, M. Royz, N. Giladi, N. Peled Levi, O. Reich, O. Gilon, R. Maor, S. Timnat, T. Shechter, V. Anisimov, Y. Gigi, Y. Levin, Z. Moshe, Z. Ben-Haim, A. Hassidim, and Y. Matias. Flood forecasting with machine learning models in an operational framework. *Hydrology and Earth System Sciences*, 26(15):4013–4032, 2022.
- [14] Husain Najafi, Pallav Kumar Shrestha, Oldrich Rakovec, Heiko Apel, Sergiy Vorogushyn, Rohini Kumar, Stephan Thober, Bruno Merz, and Luis Samaniego. High-resolution impact-based early warning system for riverine flooding. *Nature communications*, 15(1):3726, 2024.
- [15] L. Alfieri, P. Burek, E. Dutra, B. Krzeminski, D. Muraro, J. Thielen, and F. Pappenberger. Glofas - global ensemble streamflow forecasting and flood early warning. *Hydrology and Earth System Sciences*, 17(3):1161–1175, 2013.
- [16] S. Harrigan, E. Zsoter, H. Cloke, P. Salamon, and C. Prudhomme. Daily ensemble river discharge reforecasts and real-time forecasts from the operational global flood awareness system. *Hydrology and Earth System Sciences*, 27(1):1–19, 2023.
- [17] Anne Jones, Julian Kuehnert, Paolo Fraccaro, Ophélie Meuriot, Tatsuya Ishikawa, Blair Edwards, Nikola Stoyanov, Sekou L Remy, Kommy Weldemariam, and Solomon Assefa. Ai for climate impacts: applications in flood risk. *npj Climate and Atmospheric Science*, 6(1):63, 2023.
- [18] Markus Reichstein, Vitus Benson, Jan Blunk, Gustau Camps-Valls, Felix Creutzig, Carina J Fearnley, Boran Han, Kai Kornhuber, Nasim Rahaman, Bernhard Schölkopf, et al. Early warning of complex climate risk with integrated artificial intelligence. *Nature Communications*, 16(1):2564, 2025.
- [19] Grey S. Nearing, Frederik Kratzert, Alden Keefe Sampson, Craig S. Pelissier, Daniel Klotz, Jonathan M. Frame, Cristina Prieto, and Hoshin V. Gupta. What role does hydrological science play in the age of machine learning? *Water Resources Research*, 57(3):e2020WR028091, 2021. e2020WR028091.10.1029/2020WR028091.
- [20] J. M. Frame, F. Kratzert, D. Klotz, M. Gauch, G. Shalev, O. Gilon, L. M. Qualls, H. V. Gupta, and G. S. Nearing. Deep learning rainfall–runoff predictions of extreme events. *Hydrology and Earth System Sciences*, 26(13):3377–3392, 2022.
- [21] Jaideep Pathak, Shashank Subramanian, Peter Harrington, Sanjeev Raja, Ashesh Chattopadhyay, Morteza Mardani, Thorsten Kurth, David Hall, Zongyi Li, Kamyar Azizzadenesheli, et al. Fourcastnet: A global data-driven high-resolution weather model using adaptive fourier neural operators. *arXiv preprint arXiv:2202.11214*, 2022.
- [22] Ilan Price, Alvaro Sanchez-Gonzalez, Ferran Alet, Tom R Andersson, Andrew El-Kadi, Dominic Masters, Timo Ewalds, Jacklynn Stott, Shakir Mohamed, Peter Battaglia, et al. Probabilistic weather forecasting with machine learning. *Nature*, 637(8044):84–90, 2025.
- [23] Kaifeng Bi, Lingxi Xie, Hengheng Zhang, Xin Chen, Xiaotao Gu, and Qi Tian. Accurate medium-range global weather forecasting with 3d neural networks. *Nature*, 619(7970):533–538, 2023.
- [24] Grey Nearing, Deborah Cohen, Vusumuzi Dube, Martin Gauch, Oren Gilon, Shaun Harrigan, Avinatan Hassidim, Daniel Klotz, Frederik Kratzert, Asher Metzger, et al. Global prediction of extreme floods in ungauged watersheds. *Nature*, 627(8004):559–563, 2024.
- [25] Albert Gu, Isys Johnson, Karan Goel, Khaled Saab, Tri Dao, Atri Rudra, and Christopher Ré. Combining recurrent, convolutional, and continuous-time models with linear state space layers. In M. Ranzato, A. Beygelzimer, Y. Dauphin, P.S. Liang, and J. Wortman Vaughan, editors, *Advances in Neural Information Processing Systems*, volume 34, pages 572–585. Curran Associates, Inc., 2021.

- [26] Albert Gu, Karan Goel, and Christopher Ré. Efficiently modeling long sequences with structured state spaces. *arXiv preprint arXiv:2111.00396*, 2021.
- [27] Jimmy TH Smith, Andrew Warrington, and Scott W Linderman. Simplified state space layers for sequence modeling. *arXiv preprint arXiv:2208.04933*, 2022.
- [28] Albert Gu and Tri Dao. Mamba: Linear-time sequence modeling with selective state spaces. *arXiv preprint arXiv:2312.00752*, 2023.
- [29] Anouk Bomers and Suzanne J. M. H. Hulscher. Neural networks for fast fluvial flood predictions: Too good to be true? *River Research and Applications*, 39(8):1652–1658, 2023.
- [30] J. Green, I. D. Haigh, N. Quinn, J. Neal, T. Wahl, M. Wood, D. Eilander, M. de Ruiter, P. Ward, and P. Camus. Review article: A comprehensive review of compound flooding literature with a focus on coastal and estuarine regions. *Natural Hazards and Earth System Sciences*, 25(2):747–816, 2025.
- [31] T. Cache, M. S. Gomez, T. Beucler, J. Blagojevic, J. P. Leita, and N. Peleg. Enhancing generalizability of data-driven urban flood models by incorporating contextual information. *Hydrology and Earth System Sciences*, 28(24):5443–5458, 2024.
- [32] Julian Hofmann and Holger Schüttrumpf. floodgan: Using deep adversarial learning to predict pluvial flooding in real time. *Water*, 13(16), 2021.
- [33] Tim Busker, Bart van den Hurk, Hans de Moel, and Jeroen CJH Aerts. The value of precipitation forecasts to anticipate floods. *Bulletin of the American Meteorological Society*, 2025.
- [34] Amir Mosavi, Pinar Ozturk, and Kwok-wing Chau. Flood prediction using machine learning models: Literature review. *Water*, 10(11):1536, 2018.
- [35] R. Bentivoglio, E. Isufi, S. N. Jonkman, and R. Taormina. Deep learning methods for flood mapping: a review of existing applications and future research directions. *Hydrology and Earth System Sciences*, 26(16):4345–4378, 2022.
- [36] Zifeng Guo, João P. Leitão, Nuno E. Simões, and Vahid Moosavi. Data-driven flood emulation: Speeding up urban flood predictions by deep convolutional neural networks. *Journal of Flood Risk Management*, 14(1):e12684, 2021.
- [37] Alexander Y. Sun, Zhi Li, Wonhyun Lee, Qixing Huang, Bridget R. Scanlon, and Clint Dawson. Rapid flood inundation forecast using fourier neural operator. In *2023 IEEE/CVF International Conference on Computer Vision Workshops (ICCVW)*, pages 3735–3741, 2023.
- [38] Omar Seleem, Georgy Ayzel, Arthur Costa Tomaz de Souza, Axel Bronstert, and Maik Heistermann. Towards urban flood susceptibility mapping using data-driven models in berlin, germany. *Geomatics, Natural Hazards and Risk*, 13(1):1640–1662, 2022.
- [39] Benjamin Burrichter, Julian Hofmann, Juliana Koltermann da Silva, Andre Niemann, and Markus Quirmbach. A spatiotemporal deep learning approach for urban pluvial flood forecasting with multi-source data. *Water*, 15(9), 2023.
- [40] Haibo Chu, Wenyan Wu, Q.J. Wang, Rory Nathan, and Jiahua Wei. An ann-based emulation modelling framework for flood inundation modelling: Application, challenges and future directions. *Environmental Modelling & Software*, 124:104587, 2020.
- [41] Fazlul Karim, Mohammed Ali Armin, David Ahmedt-Aristizabal, Lachlan Tychsen-Smith, and Lars Petersson. A review of hydrodynamic and machine learning approaches for flood inundation modeling. *Water*, 15(3), 2023.
- [42] Björn Lütjens, Brandon Leshchinskiy, Océane Boulais, Farrukh Chishtie, Natalia Díaz-Rodríguez, Margaux Masson-Forsythe, Ana Mata-Payerro, Christian Requena-Mesa, Aruna Sankaranarayanan, Aaron Piña, Yarin Gal, Chedy Raïssi, Alexander Lavin, and Dava Newman. Generating physically-consistent satellite imagery for climate visualizations. *IEEE Transactions on Geoscience and Remote Sensing*, 62:1–11, 2024.
- [43] Saeid Janizadeh, Subodh Chandra Pal, Asish Saha, Indrajit Chowdhuri, Kouros Ahmadi, Sajjad Mirzaei, Amir Hossein Mosavi, and John P. Tiefenbacher. Mapping the spatial and temporal variability of flood hazard affected by climate and land-use changes in the future. *Journal of Environmental Management*, 298:113551, 2021.

- [44] Antara Dasgupta, Renaud Hostache, RAAJ Ramsankaran, Guy J.-P. Schumann, Stefania Grimaldi, Valentijn R. N. Pauwels, and Jeffrey P. Walker. A mutual information-based likelihood function for particle filter flood extent assimilation. *Water Resources Research*, 57(2):e2020WR027859, 2021. e2020WR027859 2020WR027859.
- [45] Nikolaos Ioannis Bountos, Maria Sdraka, Angelos Zavras, Ilektra Karasante, Andreas Karavias, Themistocles Herekakis, Angeliki Thanasou, Dimitrios Michail, and Ioannis Papoutsis. Kuro siwo: 33 billion m² under the water. a global multi-temporal satellite dataset for rapid flood mapping. In A. Globerson, L. Mackey, D. Belgrave, A. Fan, U. Paquet, J. Tomczak, and C. Zhang, editors, *Advances in Neural Information Processing Systems*, volume 37, pages 38105–38121. Curran Associates, Inc., 2024.
- [46] Wahid Palash, Ali S Akanda, and Shafiqul Islam. A data-driven global flood forecasting system for medium to large rivers. *Scientific Reports*, 14(1):8979, 2024.
- [47] Liangjin Zhong, Huimin Lei, Zhiyuan Li, and Shijie Jiang. Advancing streamflow prediction in data-scarce regions through vegetation-constrained distributed hybrid ecohydrological models. *Journal of Hydrology*, 645:132165, 2024.
- [48] F. Kratzert, M. Gauch, D. Klotz, and G. Nearing. Hess opinions: Never train a long short-term memory (lstm) network on a single basin. *Hydrology and Earth System Sciences*, 28(17):4187–4201, 2024.
- [49] Sepp Hochreiter and Jürgen Schmidhuber. Long short-term memory. *Neural Computation*, 9(8):1735–1780, 1997.
- [50] F. Kratzert, D. Klotz, G. Shalev, G. Klambauer, S. Hochreiter, and G. Nearing. Towards learning universal, regional, and local hydrological behaviors via machine learning applied to large-sample datasets. *Hydrology and Earth System Sciences*, 23(12):5089–5110, 2019.
- [51] Benedikt Heudorfer, Hoshin V. Gupta, and Ralf Loritz. Are deep learning models in hydrology entity aware? *Geophysical Research Letters*, 52(6):e2024GL113036, 2025. e2024GL113036 2024GL113036.
- [52] Yikui Zhang, Silvan Ragetti, Peter Molnar, Olga Fink, and Nadav Peleg. Generalization of an encoder-decoder lstm model for flood prediction in ungauged catchments. *Journal of Hydrology*, 614:128577, 2022.
- [53] Binlan Zhang, Chaojun Ouyang, Peng Cui, Qingsong Xu, Dongpo Wang, Fei Zhang, Zhong Li, Linfeng Fan, Marco Lovati, Yanling Liu, and Qianqian Zhang. Deep learning for cross-region streamflow and flood forecasting at a global scale. *The Innovation*, 5(3):100617, 2024.
- [54] Karan Ruparell, Robert J Marks, Andy Wood, Kieran MR Hunt, Hannah L Cloke, Christel Prudhomme, Florian Pappenberger, and Matthew Chantry. Hydra-lstm: A semi-shared machine learning architecture for prediction across watersheds. *arXiv preprint arXiv:2410.16343*, 2024.
- [55] Yihan Wang, Lujun Zhang, N. Benjamin Erichson, and Tiantian Yang. Investigating the streamflow simulation capability of a new mass-conserving long short-term memory (mc-lstm) model across the contiguous united states. *Journal of Hydrology*, 658:133161, 2025.
- [56] E. Acuña Espinoza, F. Kratzert, D. Klotz, M. Gauch, M. Álvarez Chaves, R. Loritz, and U. Ehret. Technical note: An approach for handling multiple temporal frequencies with different input dimensions using a single lstm cell. *Hydrology and Earth System Sciences*, 29(6):1749–1758, 2025.
- [57] Gideon Stein, Maha Shadaydeh, Jan Blunk, Niklas Penzel, and Joachim Denzler. Causalrivers—scaling up benchmarking of causal discovery for real-world time-series. *arXiv preprint arXiv:2503.17452*, 2025.
- [58] Nikolas Kirschstein and Yixuan Sun. The merit of river network topology for neural flood forecasting. In *International Conference on Machine Learning*, pages 24713–24725. PMLR, 2024.
- [59] Naghmeh Shafiee Roudbari, Shubham Rajeev Puneekar, Zachary Patterson, Ursula Eicker, and Charalambos Poullis. From data to action in flood forecasting leveraging graph neural networks and digital twin visualization. *Scientific reports*, 14(1):18571, 2024.
- [60] Yuan Yang, Dapeng Feng, Hylke E Beck, Weiming Hu, Agniv Sengupta, Luca Delle Monache, Robert Hartman, Peirong Lin, Chaopeng Shen, and Ming Pan. Global daily discharge estimation based on grid-scale long short-term memory (lstm) model and river routing. *Authorea Preprints*, 2023.
- [61] Yue Liu, Yunjie Tian, Yuzhong Zhao, Hongtian Yu, Lingxi Xie, Yaowei Wang, Qixiang Ye, Jianbin Jiao, and Yunfan Liu. Vmamba: Visual state space model. In A. Globerson, L. Mackey, D. Belgrave, A. Fan, U. Paquet, J. Tomczak, and C. Zhang, editors, *Advances in Neural Information Processing Systems*, volume 37, pages 103031–103063. Curran Associates, Inc., 2024.

- [62] Lianghui Zhu, Bencheng Liao, Qian Zhang, Xinlong Wang, Wenyu Liu, and Xinggang Wang. Vision mamba: Efficient visual representation learning with bidirectional state space model. In *Forty-first International Conference on Machine Learning*, 2024.
- [63] Alexey Dosovitskiy, Lucas Beyer, Alexander Kolesnikov, Dirk Weissenborn, Xiaohua Zhai, Thomas Unterthiner, Mostafa Dehghani, Matthias Minderer, Georg Heigold, Sylvain Gelly, et al. An image is worth 16x16 words: Transformers for image recognition at scale. *arXiv preprint arXiv:2010.11929*, 2020.
- [64] Hao Phung, Quan Dao, Trung Dao, Hoang Phan, Dimitris N. Metaxas, and Anh Tran. Dimsum: Diffusion mamba - a scalable and unified spatial-frequency method for image generation. In A. Globerson, L. Mackey, D. Belgrave, A. Fan, U. Paquet, J. Tomczak, and C. Zhang, editors, *Advances in Neural Information Processing Systems*, volume 37, pages 32947–32979. Curran Associates, Inc., 2024.
- [65] Vincent Tao Hu, Stefan Andreas Baumann, Ming Gui, Olga Grebenkova, Pingchuan Ma, Johannes Fischer, and Björn Ommer. Zigma: A dit-style zigzag mamba diffusion model. In Aleš Leonardis, Elisa Ricci, Stefan Roth, Olga Russakovsky, Torsten Sattler, and Gül Varol, editors, *Computer Vision – ECCV 2024*, pages 148–166, Cham, 2025. Springer Nature Switzerland.
- [66] Yicheng Xiao, Lin Song, Shaoli Huang, Jiangshan Wang, Siyu Song, Yixiao Ge, Xiu Li, and Ying Shan. Mambatree: Tree topology is all you need in state space model. In A. Globerson, L. Mackey, D. Belgrave, A. Fan, U. Paquet, J. Tomczak, and C. Zhang, editors, *Advances in Neural Information Processing Systems*, volume 37, pages 75329–75354. Curran Associates, Inc., 2024.
- [67] Abdelrahman Shaker, Syed Talal Wasim, Salman Khan, Jürgen Gall, and Fahad Shahbaz Khan. Group-mamba: Parameter-efficient and accurate group visual state space model. *arXiv preprint arXiv:2407.13772*, 2024.
- [68] Kunchang Li, Xinhao Li, Yi Wang, Yanan He, Yali Wang, Limin Wang, and Yu Qiao. Videomamba: State space model for efficient video understanding. In Aleš Leonardis, Elisa Ricci, Stefan Roth, Olga Russakovsky, Torsten Sattler, and Gül Varol, editors, *Computer Vision – ECCV 2024*, pages 237–255, Cham, 2025. Springer Nature Switzerland.
- [69] Guo Chen, Yifei Huang, Jilan Xu, Baoqi Pei, Zhe Chen, Zhiqi Li, Jiahao Wang, Kunchang Li, Tong Lu, and Limin Wang. Video mamba suite: State space model as a versatile alternative for video understanding. *arXiv preprint arXiv:2403.09626*, 2024.
- [70] Zeyu Zhang, Akide Liu, Ian Reid, Richard Hartley, Bohan Zhuang, and Hao Tang. Motion mamba: Efficient and long sequence motion generation. In Aleš Leonardis, Elisa Ricci, Stefan Roth, Olga Russakovsky, Torsten Sattler, and Gül Varol, editors, *Computer Vision – ECCV 2024*, pages 265–282, Cham, 2025. Springer Nature Switzerland.
- [71] Olga Zatsarynna, Emad Bahrami, Yazan Abu Farha, Gianpiero Francesca, and Juergen Gall. Manta: Diffusion mamba for efficient and effective stochastic long-term dense anticipation. *arXiv preprint arXiv:2501.08837*, 2025.
- [72] Dingkan Liang, Xin Zhou, Wei Xu, Xingkui Zhu, Zhikang Zou, Xiaoqing Ye, Xiao Tan, and Xiang Bai. Pointmamba: A simple state space model for point cloud analysis. In A. Globerson, L. Mackey, D. Belgrave, A. Fan, U. Paquet, J. Tomczak, and C. Zhang, editors, *Advances in Neural Information Processing Systems*, volume 37, pages 32653–32677. Curran Associates, Inc., 2024.
- [73] Guowen Zhang, Lue Fan, Chenhang He, Zhen Lei, Zhaoxiang Zhang, and Lei Zhang. Voxel mamba: Group-free state space models for point cloud based 3d object detection. In A. Globerson, L. Mackey, D. Belgrave, A. Fan, U. Paquet, J. Tomczak, and C. Zhang, editors, *Advances in Neural Information Processing Systems*, volume 37, pages 81489–81509. Curran Associates, Inc., 2024.
- [74] J. Muñoz Sabater, E. Dutra, A. Agustí-Panareda, C. Albergel, G. Arduini, G. Balsamo, S. Boussetta, M. Choulga, S. Harrigan, H. Hersbach, B. Martens, D. G. Miralles, M. Piles, N. J. Rodríguez-Fernández, E. Zsoter, C. Buontempo, and J.-N. Thépaut. Era5-land: a state-of-the-art global reanalysis dataset for land applications. *Earth System Science Data*, 13(9):4349–4383, 2021.
- [75] S. Harrigan, E. Zsoter, L. Alfieri, C. Prudhomme, P. Salamon, F. Wetterhall, C. Barnard, H. Cloke, and F. Pappenberger. Glofas-era5 operational global river discharge reanalysis 1979–present. *Earth System Science Data*, 12(3):2043–2060, 2020.
- [76] Pingping Xie, M Chen, and W Shi. Cpc unified gauge-based analysis of global daily precipitation. In *Preprints, 24th Conf. on Hydrology, Atlanta, GA, Amer. Meteor. Soc.*, volume 2, 2010.

- [77] Pingping Xie, Mingyue Chen, Song Yang, Akiyo Yatagai, Tadaihiro Hayasaka, Yoshihiro Fukushima, and Changming Liu. A gauge-based analysis of daily precipitation over east asia. *Journal of Hydrometeorology*, 8(3):607–626, 2007.
- [78] Mingyue Chen, Wei Shi, Pingping Xie, Viviane BS Silva, Vernon E Kousky, R Wayne Higgins, and John E Janowiak. Assessing objective techniques for gauge-based analyses of global daily precipitation. *Journal of Geophysical Research: Atmospheres*, 113(D4), 2008.
- [79] M. Choulga, F. Moschini, C. Mazzetti, S. Grimaldi, J. Disperati, H. Beck, P. Salamon, and C. Prudhomme. Technical note: Surface fields for global environmental modelling. *Hydrology and Earth System Sciences*, 28(13):2991–3036, 2024.
- [80] Tri Dao, Dan Fu, Stefano Ermon, Atri Rudra, and Christopher Ré. Flashattention: Fast and memory-efficient exact attention with io-awareness. *Advances in neural information processing systems*, 35:16344–16359, 2022.
- [81] Tri Dao. FlashAttention-2: Faster attention with better parallelism and work partitioning. In *International Conference on Learning Representations (ICLR)*, 2024.
- [82] Giuseppe Peano and G Peano. *Sur une courbe, qui remplit toute une aire plane*. Springer, 1990.
- [83] David Hilbert and David Hilbert. Über die stetige abbildung einer linie auf ein flächenstück. *Dritter Band: Analysis· Grundlagen der Mathematik· Physik Verschiedenes: Nebst Einer Lebensgeschichte*, pages 1–2, 1935.
- [84] Mohamad Hakam Shams Eddin, Ribana Roscher, and Juergen Gall. Location-aware adaptive normalization: A deep learning approach for wildfire danger forecasting. *IEEE Transactions on Geoscience and Remote Sensing*, 61:1–18, 2023.
- [85] Ashish Vaswani, Noam Shazeer, Niki Parmar, Jakob Uszkoreit, Llion Jones, Aidan N Gomez, Łukasz Kaiser, and Illia Polosukhin. Attention is all you need. In I. Guyon, U. Von Luxburg, S. Bengio, H. Wallach, R. Fergus, S. Vishwanathan, and R. Garnett, editors, *Advances in Neural Information Processing Systems*, volume 30. Curran Associates, Inc., 2017.
- [86] J. M. Van Der Knijff, J. Younis, and A. P. J. De Roo and. Lisflood: a gis-based distributed model for river basin scale water balance and flood simulation. *International Journal of Geographical Information Science*, 24(2):189–212, 2010.
- [87] Hans Hersbach, Bill Bell, Paul Berrisford, Shoji Hirahara, András Horányi, Joaquín Muñoz-Sabater, Julien Nicolas, Carole Peubey, Raluca Radu, Dinand Schepers, Adrian Simmons, Cornel Soci, Saleh Abdalla, Xavier Abellan, Gianpaolo Balsamo, Peter Bechtold, Gionata Biavati, Jean Bidlot, Massimo Bonavita, Giovanna De Chiara, Per Dahlgren, Dick Dee, Michail Diamantakis, Rossana Dragani, Johannes Flemming, Richard Forbes, Manuel Fuentes, Alan Geer, Leo Haimberger, Sean Healy, Robin J. Hogan, Elías Hólm, Marta Janisková, Sarah Keeley, Patrick Laloyaux, Philippe Lopez, Cristina Lupu, Gabor Radnoti, Patricia de Rosnay, Iryna Rozum, Freja Vamborg, Sebastien Villaume, and Jean-Noël Thépaut. The era5 global reanalysis. *Quarterly Journal of the Royal Meteorological Society*, 146(730):1999–2049, 2020.
- [88] Zuzanna Zajac, Beatriz Revilla-Romero, Peter Salamon, Peter Burek, Feyera A. Hirpa, and Hylke Beck. The impact of lake and reservoir parameterization on global streamflow simulation. *Journal of Hydrology*, 548:552–568, 2017.

RiverMamba: A State Space Model for Global River Discharge and Flood Forecasting



Technical Appendices and Supplementary Material

Table of Contents

A Dataset	18
A.1 GloFAS reanalysis data	18
A.2 GRDC observational river discharge data	18
A.3 ERA5-Land data	20
A.4 HRES	20
A.5 CPC data	21
A.6 LISFLOOD static features	22
A.7 Diagnostic river points	22
B Return periods and flood definition	24
C Implementation and training details	24
D Mamba Block	26
E Evaluation metrics	27
F Ablation studies	29
F.1 Mamba vs. Transformer	29
F.2 Feature importance	29
F.3 Pretraining on Reanalysis	30
F.4 Space-filling curves	30
G Baselines	32
G.1 Climatology	32
G.2 Persistence	32
G.3 LSTM	32
G.4 GloFAS Forecast	33
G.5 GloFAS Reforecast	33
H Space-filling curves	34
I Experiments on HydroRIVERS	37

J	Additional results	38
J.1	Comparison with Google reforecast on ungauged GRDC	38
J.2	Comparison with Google reforecast on gauged GRDC	41
J.3	Additional results on gauged GloFAS reanalysis	44
J.4	Additional results on gauged GRDC	53
J.5	Comparison to operational GloFAS forecasts on gauged GRDC	62
J.6	Case studies of extreme flood events	63
J.6.1	2021 Western Europe flood	63
J.6.2	2024 Southeast Europe floods	64
J.6.3	2024 Central European floods	65
J.6.4	2024 Spanish floods	65
J.6.5	2024 Saarland Germany flood	66
J.6.6	2024 Kenya-Tanzania flood	66
J.6.7	2024 California flood	67
J.6.8	2024 Central-South China floods	67
K	Code and data availability	68
L	Broader impacts	68

A Dataset

A.1 GloFAS reanalysis data

The Global Flood Awareness System (GloFAS) is an operational system developed by the European Commission’s Joint Research Centre (JRC) and operated by ECMWF under the Copernicus Emergency Management Service (CEMS) [15]. It provides real-time global-scale flood forecasts and a long-term hydrological reanalysis dataset, a key resource for flood risk assessment, climate impact studies, and machine learning applications. Fig. 7 shows the workflow of GloFAS to forecast river discharge and flood events. The GloFAS-ERA5 reanalysis is the long-term retrospective component of GloFAS [75]. It delivers daily river discharge estimates from 1979 to present at a spatial resolution of 0.05° (~ 5 km) and a global coverage (90°N - 60°S , 180°W - 180°E). The reanalysis is generated by coupling surface and subsurface runoff from the ERA5 reanalysis, produced by the H-TESSEL and surface model [91] with the LISFLOOD hydrological and river routing model [86]. While ERA5 runoff is computed at ~ 31 km resolution and lacks spatial connectivity, it is downscaled to 0.05° using a nearest-neighbour approach and routed through LISFLOOD to simulate realistic river discharge (dis_{24} , in m^3s^{-1}) across the global river network. The daily GloFAS reanalysis discharge data represents the mean value between 00:00 UTC previous day and 00:00 UTC current day. Similarly to GloFAS, there exists an early warning system for Europe (EFAS) with higher resolution [12]. In our work, GloFAS v4.0 is used for a global application. The dataset is publicly available on Climate Data Store and Early Warning Data Store (EWDs) <https://doi.org/10.24381/cds.a4fdd6b9>. Table 4 explains the details of four variables we took from the GloFAS reanalysis dataset as the model inputs. The GloFAS-ERA5 reanalysis supports the derivation of flood thresholds (i.e., 2-, 5-, and 20-year return periods) and serves as the initial condition for real-time forecasts such as GloFAS-30d and GloFAS-Seasonal. More details about GloFAS can be found in [75].

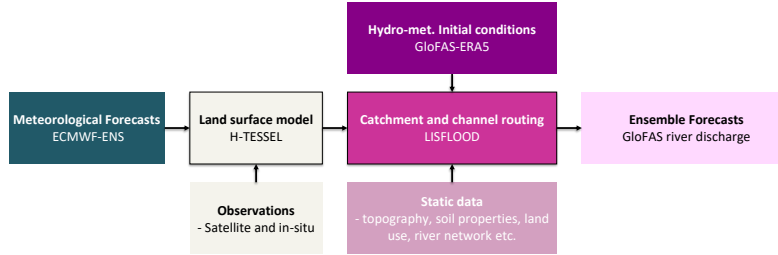


Figure 7: An overview of the key modules in the GloFAS forecasting system. GloFAS-ERA5 reanalysis uses ERA5 meteorological reanalysis data instead of ECMWF ensemble forecasts (ENS). Figure outline from [75].

Despite its broad applicability, the GloFAS-ERA5 reanalysis is subject to several limitations that researchers should be aware of. Regional biases have been identified, which may stem from uncertainties in the meteorological forcing provided by ERA5, the representation of runoff generation processes within the H-TESSEL land surface model, and limitations in the calibration of the LISFLOOD routing model. When sufficient observational discharge data are available, the LISFLOOD model is calibrated locally for each river catchment larger than 500 km^2 , and each calibrated catchment has its own optimized parameter set. This could give the model better performance at the local scale but reduce its generalization ability. Additionally, anthropogenic influences such as dams and reservoirs are incorporated using simplified operational rules, largely due to the lack of globally available real-time release data. Finally, as the dataset is entirely driven by ERA5, it inherits known deficiencies of the reanalysis, including biases in precipitation and the absence of river discharge data assimilation, which may affect the realism of simulated hydrological conditions in some regions.

A.2 GRDC observational river discharge data

We obtain observational river discharge from the Global Runoff Data Centre (GRDC) which is an international data repository that provides access to quality-controlled river discharge observation

Table 4: Details about the processed variables from GloFAS reanalysis [75].

Variable	Long name	Unit	Height	Surface parameters
acc_rod24	runoff water equivalent	kg/m ²	surface and subsurface	accumulated
dis24	river discharge in the last 24 hours	m ³ /s	surface	averaged over 24 hours
sd	snow depth water equivalent	kg/m ²	surface	instantaneous
swi	soil wetness index	-	root zone	instantaneous

data from around the world. GRDC dataset contains time series of daily and monthly river discharge data from over 10000 hydrological gauging stations across more than 160 countries from small headwater catchments ($\sim 10 \text{ km}^2$ drainage area) to very large river catchment like Amazon river (5 million km^2 drainage area). GRDC data can be obtained from <https://grdc.bafg.de/>. All GRDC daily time series measured the value set at 00:00 of the beginning of the day (left-labeled). To keep our evaluation consistent with [24], we used the GRDC dataset as the benchmark to evaluate the model performance and followed a similar data processing workflow as in [16, 24]. We first removed the catchments with a drainage area smaller than 500 km^2 and obtained 5524 GRDC stations to avoid very big discrepancies between the drainage area defined in GRDC and in the GloFAS dataset (A.1). Next, we geo-located the GRDC stations to compare them with the GloFAS drainage network and removed the GRDC stations with more than 10% of drainage area differences. For geo-location, we projected the points on the GloFAS grid, compared each point with its 9 nearest points, and took the location with the highest KGE value. Finally, the GRDC stations with no ERA5-Land reanalysis data were discarded. This resulted in 3366 stations for the global evaluation. This narrowed down the global median drainage area difference to 2.21% with an interquartile range of 0.86% to 4.73%. The discharge observations are recorded at a daily time scale, with the unit m^3s^{-1} and converted from local time zone to 00:00 UTC via linear interpolation.

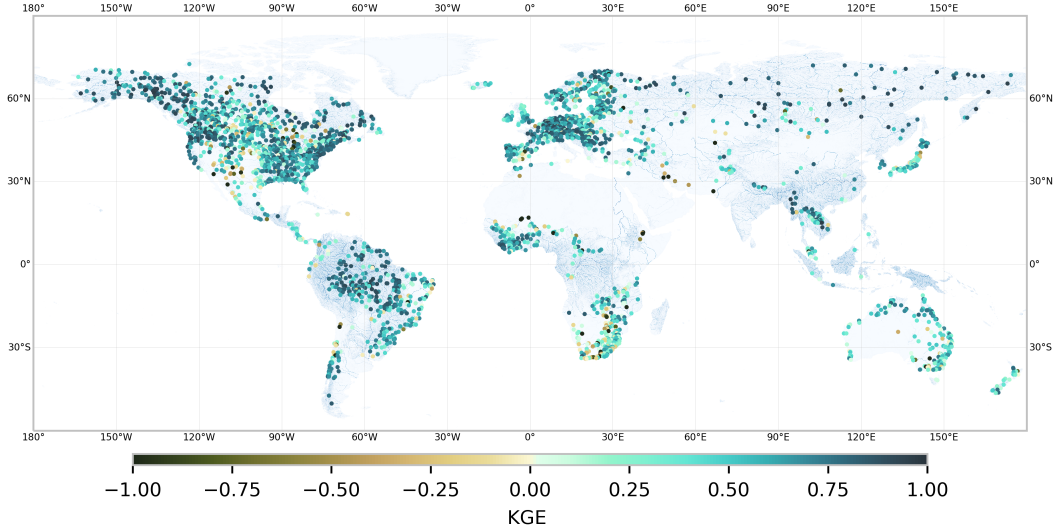


Figure 8: Locations of selected 3366 GRDC stations used for training and evaluating the RiverMamba model. The colorbar shows the KGE value of GloFAS reanalysis discharge data against the GRDC discharge observations.

Fig. 8 shows the KGE values of GloFAS reanalysis data against the GRDC observation at the locations of all 3366 selected stations. In general, there is a good agreement between GloFAS and GRDC data globally, with a median KGE at 0.61 and an interquartile range of 0.36 to 0.77. In regions like south America, south Africa and Australia, the GloFAS reanalysis data have more inconsistency compared to the observations. Fig. 9 shows an exemplar hydrograph for a gauged station.

It is important to note that, compared to the GRDC observations, the GloFAS reanalysis dataset only simulates the naturalized flow without considering realistic human interventions such as dams,

reservoirs, diversions, irrigation withdrawals, and other water management practices, and this can be a major source of bias in GloFAS compared to the GRDC data.

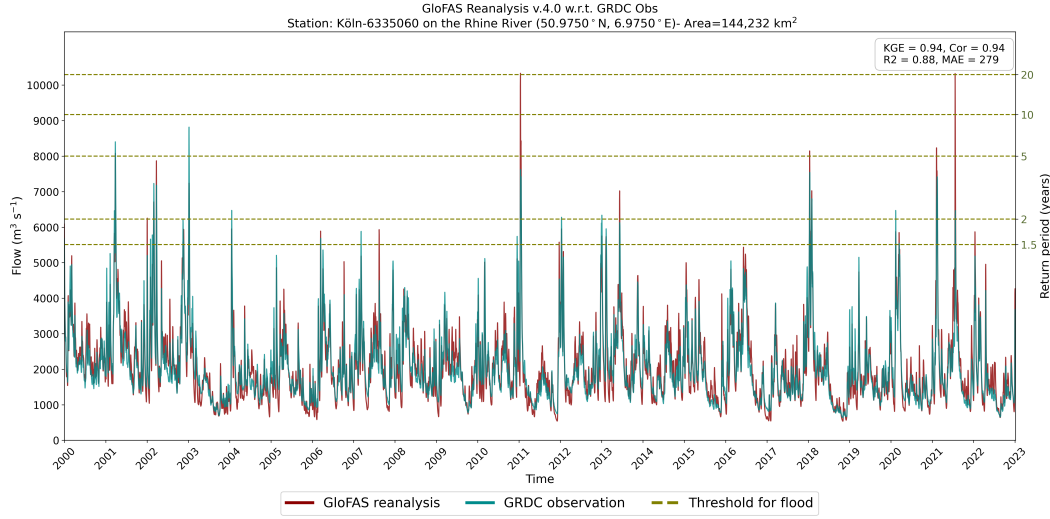


Figure 9: Hydrograph for GloFAS-reanalysis (red line) from 1 January 2000 to 31 December 2023 and observations (dark cyan line), for a gauging station on the Rhine River. The top-right box displays summary statistics from the reanalysis's evaluation against the observations.

A.3 ERA5-Land data

In contrast to operational GloFAS which uses ERA5 as forcing data, we use ERA5-Land as an initial land surface condition for the forecast. The ERA5-Land reanalysis data are described in [74] and retrieved from the Copernicus Climate Change Service (C3S) Climate Data Store (CDS), <https://doi.org/10.24381/cds.e2161bac>. We processed 14 instantaneous state variables at 00:00 UTC and 18 daily accumulated state variables (00:00 UTC previous day to 00:00 UTC current day). More details are provided in Table 5. ERA5-Land is provided at $0.1^\circ \times 0.1^\circ$. We mapped the data onto the GloFAS regular latitude and longitude (Plate Carrée projection) using bilinear mapping and implemented by Zhuang et. al [97].

A.4 HRES

Meteorological conditions serve as the driving forces behind hydrological processes. These are necessary for forecasting the river discharge and potential floods. We use the deterministic forecast of the ECMWF Integrated Forecast System (IFS) High Resolution (HRES) atmospheric model. The HRES data were obtained from the ECMWF Archive Catalogue <https://www.ecmwf.int/en/forecasts/dataset/operational-archive>. We use HRES up to 7 days lead time and once per day at 00:00 UTC. This is different to GloFAS which uses input from ECMWF ensemble forecasts (ENS) twice per day at 00:00 UTC and at 12:00 UTC. The processed data are similar to [24] except that we used total evaporation as an additional forcing variable. In addition, we do not use any forecast for nowcasting at time step t . The processed data include 2 instantaneous and 5 daily accumulated variables at the surface level forecasts. It is worth to note that GloFAS forecasting system uses more meteorological forcing to drive its forecasting. Technical details regarding the meteorological forcing variables are provided in Tables 6.

While the operational archive provides data from 1985, the quality and the resolution of the forecasts in the earlier years are not sufficient for our application. Therefore, we only processed and used data from 2010 to 2024. Data before 2010 were replaced by ERA5-Land. To match the resolution of the target GloFAS grid, we regridded HRES to $0.05^\circ \times 0.05^\circ$ regular grid.

Table 5: Details about the processed variables from ERA5-Land reanalysis [74].

Variable	Long name	Unit	Height	Surface parameters
d2m	2m dewpoint temperature	K	2m	instantaneous
e	total evaporation	m of water equivalent	surface	accumulated
es	snow evaporation	m of water equivalent	surface	accumulated
evabs	evaporation from bare soil	m of water equivalent	surface	accumulated
evaow	evaporation from open water surfaces excluding oceans	m of water equivalent	surface	accumulated
evatc	evaporation from the top of canopy	m of water equivalent	surface	accumulated
evavt	evaporation from vegetation transpiration	m of water equivalent	surface	accumulated
lai_hv	leaf area index high vegetation	m ² /m ²	2m	instantaneous
lai_lv	leaf area index low vegetation	m ² /m ²	2m	instantaneous
pev	potential evaporation	m	2m	accumulated
sf	Snowfall	m of water equivalent	surface	accumulated
skt	skin temperature	K	surface	instantaneous
slhf	surface latent heat flux	J/m ²	surface	accumulated
smlt	snowmelt	m of water equivalent	surface	accumulated
sp	surface pressure	Pa	surface	instantaneous
src	skin reservoir content	m of water equivalent	surface	instantaneous
sro	surface runoff	m	surface	accumulated
sshf	surface sensible heat flux	J/m ²	surface	accumulated
ssr	surface net solar radiation	J/m ²	surface	accumulated
ssrd	surface solar radiation downwards	J/m ²	surface	accumulated
ssro	subsurface runoff	m	subsurface	accumulated
stl1	soil temperature	K	soil layer (0 - 7 cm)	instantaneous
str	surface net thermal radiation	J/m ²	surface	accumulated
strd	surface thermal radiation downwards	J/m ²	surface	accumulated
swvl1	volumetric soil water	m ³ /m ³	soil layer (0 - 7 cm)	instantaneous
swvl2	volumetric soil water	m ³ /m ³	soil layer (7 - 28 cm)	instantaneous
swvl3	volumetric soil water	m ³ /m ³	soil layer (28 - 100 cm)	instantaneous
swvl4	volumetric soil water	m ³ /m ³	soil layer (100 - 289 cm)	instantaneous
t2m	2m temperature	K	2m	instantaneous
tp	total precipitation	m	surface	accumulated
u10	10 metre U wind component	m/s	10m	instantaneous
v10	10 metre V wind component	m/s	10m	instantaneous

Table 6: Details about the processed variables from the ECMWF Integrated Forecast System (IFS) High Resolution (HRES) atmospheric model.

Variable	Long name	Unit	Height	Surface parameters
e	total evaporation	m of water equivalent	surface	accumulated
sf	snowfall	m of water equivalent	surface	accumulated
sp	surface pressure	Pa	surface	instantaneous
ssr	surface net solar radiation	J/m ²	surface	accumulated
str	surface net thermal radiation	J/m ²	surface	accumulated
t2m	2m temperature	K	2m	instantaneous
tp	total precipitation	m	surface	accumulated

A.5 CPC data

Relying solely on the precipitation products from ERA5-Land reanalysis makes the model prone to the biases of the data assimilation which was used to derive the reanalysis. Similar to [24], we use precipitation estimates as observational input from the National Oceanic and Atmospheric

Administration (NOAA), Climate Prediction Center (CPC). The product is called Global Unified Gauge-Based Analysis of Daily Precipitation. The CPC precipitation product is accumulated daily and provided globally at $0.5^\circ \times 0.5^\circ$. To match the resolution of the target river discharge, we mapped CPC data onto the GloFAS domain using nearest point algorithm which preserves the original coarse grid structure but refines the resolution. We did not do any modification for the CPC time zones since it will be shifted two days in the past (see Sec. C). More details regarding the construction of the daily gauge analysis, the interpolation algorithm, and the gauge algorithm evaluation can be found in [76–78]. Operational CPC data can be obtained from <https://psl.noaa.gov/data/gridded/data.cpc.globalprecip.html>.

A.6 LISFLOOD static features

River attributes and static maps are crucial to capture the sub-grid variability for the river discharge. For consistency and to make a fair comparison with GloFAS, we used LISFLOOD input static maps [79] similar to the operational GloFAS. This includes 96 time-invariant variables from 7 different categories (Table 7). The maps are provided at the same resolution as GloFAS at 3 arcmin and covering the globe (90°N-60°S, 180°W-180°E). We excluded the lakes, reservoirs and some static water demand maps.

In addition, we add the Cartesian coordinates for the points on the WGS-84 ellipsoid to enhance the positional encoding:

$$x = (N + H) \cos \phi \cos \lambda, \quad y = (N + H) \cos \phi \sin \lambda, \quad z = ((1 - e^2) + H) \sin \phi, \quad (9)$$

$$N = \frac{a}{\sqrt{(1 - e^2 \sin^2(\phi))}}, \quad e^2 = \frac{a^2 - b^2}{a^2}, \quad (10)$$

where N is the radius of curvature in the prime vertical, H is the height from the elevation model, ϕ and λ are the geographic latitude and longitude, respectively, a and b are the semi-major and semi-minor axes of the ellipse, and e is the eccentricity. We set $a = 6,378.137$ km and $b = 6,356.752$ km.

The LISFLOOD static maps can be obtained from the Joint Research Centre Data Catalogue <http://data.europa.eu/89h/68050d73-9c06-499c-a441-dc5053cb0c86>.

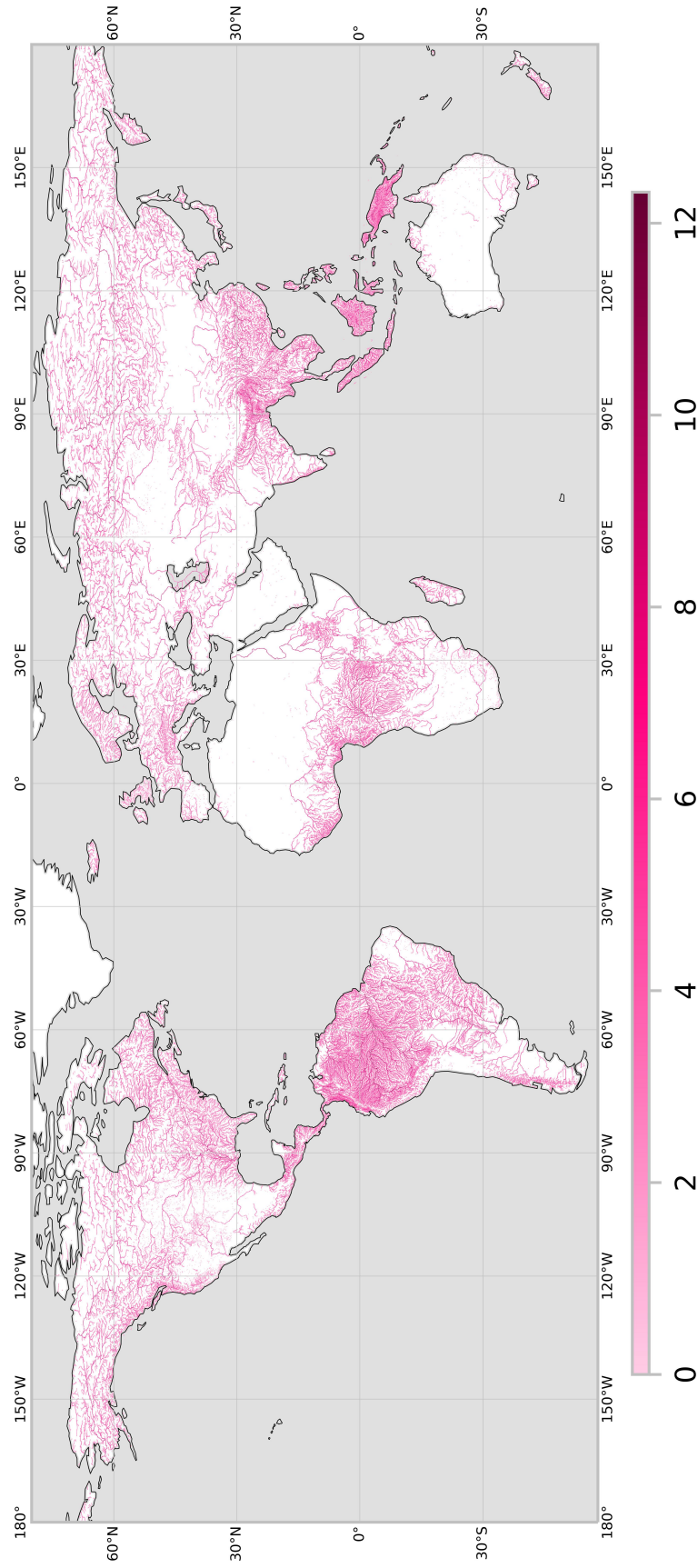
In Sec. I, we show experiments using the widely used HydroRIVERS river attributes data [102, 103].

Table 7: The processed LISFLOOD static and parameter maps [79].

Category	# Static features
catchment morphology and river network	12
grid	2
land use	6
vegetation properties	45
soil properties	14
water demand	3
GloFASv4.0 calibrated parameters	14

A.7 Diagnostic river points

The original resolution of GloFAS v.4.0 is 3 arcmin with an image resolution of 3000×7200 (21 million pix). In order to run experiments efficiently, we sampled points. For this, we remove all points that are not located on the land surface, i.e., points over ocean or sea. This reduced the points from 21,000,000 to 6,221,926 points. We excluded points with median river discharge less than $10 \text{ m}^3 \text{ s}^{-1}$ since river discharge is more relevant where there is a water flow, i.e., points that are located near to water bodies and not located over desert or glacier regions. Points which are close to rivers (distance 1 pix to points with discharge $> 10 \text{ m}^3 \text{ s}^{-1}$) were not excluded. We also do not exclude points defined as GRDC stations. This reduced the points further to 1,529,667 diagnostic river points on which we train and test. Figure 10 gives an overview of the filtered diagnostic river points used in this study. Note that the trained model can generate river discharge maps at full resolution as can be seen in Sec. J.6.



River discharge [$\text{m}^3 \text{s}^{-1}$] (log scale)

Figure 10: Overview of the selected river points.

B Return periods and flood definition

In hydrology, the return period (also known as the recurrence interval) is a statistical measure that estimates how often a given hydrological event such as a flood, drought, or heavy rainfall is expected to occur on average over a long period. In this study, the return periods refer to the flood frequency. For example, a 2-year flood has a 50% chance of being exceeded in any given year. The return period (RP) is defined as the inverse of the annual exceedance probability (AEP):

$$RP = \frac{1}{AEP}. \quad (11)$$

In practice, flood return periods are used to define flood thresholds, i.e., a flood warning is triggered when discharge exceeds the 2-year threshold. In this study, we adopt the GloFAS approach to define flood thresholds corresponding to selected return periods (or recurrence intervals) of 1.5, 2, 5, 10, 20, 50, 100, 200, and 500 years. These thresholds are derived from the LISFLOOD reanalysis simulations, which are forced with ERA5 meteorological data. The return levels are estimated by fitting a Gumbel extreme value distribution to the annual maxima for the period 1979–2022, using the L-moments method. For the evaluation on GloFAS reanalysis data, we use the pre-defined return periods data from Copernicus Emergency Management Service (<https://confluence.ecmwf.int/display/CEMS/Auxiliary+Data>). For the GRDC observation dataset, we calculated the return periods at individual stations from the first available observation date to 2022. To allow a fair evaluation of GloFAS reanalysis data on GRDC observation, the return period of GloFAS data is also calculated at GRDC stations but on the local available observation time period. Fig. 9 shows the flood thresholds defined by different return periods.

C Implementation and training details

The training was done on clusters with NVIDIA A100 80GB and 48GB GPUs. In Table 8, we highlight the main hyperparameters used for training RiverMamba.

To mimic a real operational setting, we shift CPC data by 2 days, GLoFAS reanalysis by 1 day, and ERA5-Land reanalysis by 1 day in the past. All input data are normalized based on the computed mean and standard deviation from the training set. To handle missing data in the reanalysis, we first use the pre-computed statistics to normalize the data. Then, we replace the invalid pixels with zero values. HRES data is always used for validating and testing. During training, we replace IFS meteorological forcing by ERA5 if they are unavailable, i.e., before 2010. The training, validation, and testing splits are shown in Fig. 11.

To accelerate training and to fit the data into the memory, we use bfloat16 floating point precision. During inference, we use float32 floating point precision. Pre-training RiverMamba took about 3 days on 16 GPUs. Finetuning on GRDC data took about 4 hours on 16 GPUs.

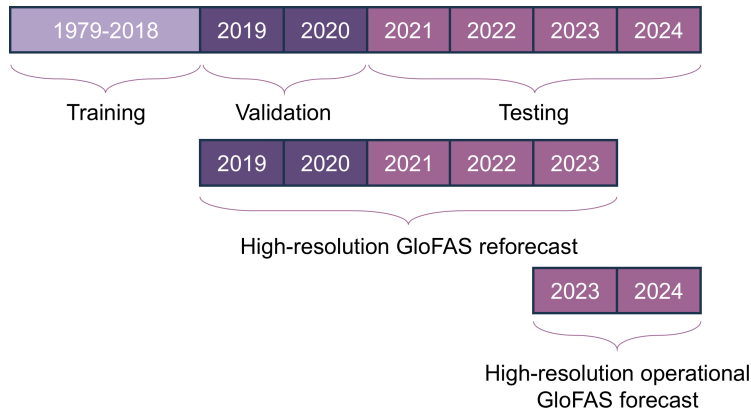


Figure 11: Details about the data splits.

Table 8: Implementation details of RiverMamba

Configuration	Pre-training (GloFAS-Reanalysis)	Training (GRDC)
Optimizer	AdamW	AdamW
Learning rate	0.0006	0.0001
Minimum learning rate	0.00009	0.00009
Batch size (B)	1	1
Learning rate scheduler	Cosine annealing	Cosine annealing
Weight decay	0.001	0.01
Training epochs	60	20
Warmup epochs	4	6
Gradient clip	10	10
Input hindcast length (T)	4	4
Lead time (L)	7	7
α for \hat{u}	0.25	0.25
Number of input point sequence P	245,954	245,954
Embedding dimension for GloFAS reanalysis	48	48
Embedding dimension for ERA5-Land reanalysis	128	128
Embedding dimension for CPC	16	16
Number of hindcast layers	3	3
Hidden dimension in hindcast block (K)	192	192
Depth of hindcast layers	[2, 2, 2]	[2, 2, 2]
Curves in hindcast layers	{Sweep_H, Sweep_V, Gilbert, Gilbert trans}	{Sweep_H, Sweep_V, Gilbert, Gilbert trans}
Grouping size in hindcast block	[(4, 254945), (2, 254945), (1, 254945)]	[(4, 254945), (2, 254945), (1, 254945)]
Dropout in hindcast block	0.2	0.4
D_state in hindcast block	16	16
D_conv in hindcast block	4	4
Hidden dimension in forecast block (K)	192+64	192+64
Embedding dimension for HRES (K_{HRES})	64	64
Number of forecast layers	7	7
Depth of forecast layers	[1, 1, 1, 1, 1, 1, 1]	[1, 1, 1, 1, 1, 1, 1]
Curves in forecast layers	{Sweep_H, Sweep_V, Gilbert, Gilbert trans}	{Sweep_H, Sweep_V, Gilbert, Gilbert trans}
Grouping size in forecast block	[(1, 254945)] * 7	[(1, 254945)] * 7
Dropout in forecast block	0.2	0.4
D_state in forecast block	16	16
D_conv in forecast block	4	4
Hidden dimension in forecasting head (K_{head})	64	64
Dropout in head	0.1	0.3

D Mamba Block

Algorithm 1 Mamba block

Require:

- 1: token sequence $\mathbf{X}^l : (\mathbf{B}, \mathbf{T}, \mathbf{P}, \mathbf{K})$
- 2: token sequence $\mathbf{X}_{static} : (\mathbf{B}, \mathbf{P}, \mathbf{K})$
- 3: curve ID (S_{block}) specific to the block l

Result:

- 4: transformed token sequence $\mathbf{X}^{l+1} : (\mathbf{B}, \mathbf{T}, \mathbf{P}, \mathbf{K})$
-
- 5: # serialize the input sequence along the P dimension
 - 6: $\mathbf{X}^l : (\mathbf{B}, \mathbf{T}, \mathbf{P}, \mathbf{K}), \mathbf{X}_{static} : (\mathbf{B}, \mathbf{P}, \mathbf{V}_s) \leftarrow \text{Serialization}(\mathbf{X}^l, S_{block}), \text{Serialization}(\mathbf{X}_{static}, S_{block})$
 - 7: # adaptively normalize the input sequence \mathbf{X}^l
 - 8: $\mathbf{X}^{l'} : (\mathbf{B}, \mathbf{T}, \mathbf{P}, \mathbf{K}) \leftarrow \text{LOAN}_1(\mathbf{X}^l, \mathbf{X}_{static})$
 - 9: # projection of $\mathbf{X}^{l'}$ into \mathbf{x} and \mathbf{z} , here E is equal to K in our work since we do not expand the dimension
 - 10: $\mathbf{x} : (\mathbf{B}, \mathbf{T}, \mathbf{P}, \mathbf{E}), \mathbf{z} : (\mathbf{B}, \mathbf{T}, \mathbf{P}, \mathbf{E}) \leftarrow \text{Linear}^{\mathbf{xz}}(\mathbf{X}^{l'})$
 - 11: # process with different direction
 - 12: **for** o in {forward, backward} **do**
 - 13: # flip the curve along the spatial dimension P
 - 14: **if** $d = \text{'backward'}$ **then**
 - 15: $\mathbf{x} : (\mathbf{B}, \mathbf{T}, \mathbf{P}, \mathbf{E}) \leftarrow \text{Flip}(\mathbf{x})$
 - 16: **end if**
 - 17: # flatten the curve along the temporal dimension 'spatial-first'
 - 18: $\mathbf{x}' : (\mathbf{B}, (\mathbf{T} \times \mathbf{P}), \mathbf{E}) \leftarrow \text{Flatten}(\mathbf{x})$
 - 19: # selective state space model, here N is the D_{state}
 - 20: $\mathbf{x}'_o : (\mathbf{B}, (\mathbf{T} \times \mathbf{P}), \mathbf{E}) \leftarrow \text{SiLU}(\text{Conv1d}_o(\mathbf{x}'))$
 - 21: $\mathbf{B}_o : (\mathbf{B}, (\mathbf{T} \times \mathbf{P}), \mathbf{N}), \mathbf{C}_o : (\mathbf{B}, (\mathbf{T} \times \mathbf{P}), \mathbf{N}) \leftarrow \text{Linear}_o^{\mathbf{B}}(\mathbf{x}'_o), \text{Linear}_o^{\mathbf{C}}(\mathbf{x}'_o)$
 - 22: # initialize D_o with ones
 - 23: $\mathbf{D}_o : (\mathbf{E}) \leftarrow \text{Parameter Ones} : (\mathbf{E})$
 - 24: # softplus ensures positive Δ_o
 - 25: $\Delta_o : (\mathbf{B}, (\mathbf{T} \times \mathbf{P}), \mathbf{E}) \leftarrow \log(1 + \exp(\text{Linear}_o^{\Delta}(\mathbf{x}'_o) + \text{Parameter}_o^{\Delta}))$
 - 26: # shape of $\text{Parameter}_o^{\Delta}$ is (\mathbf{E}, \mathbf{N})
 - 27: $\overline{\mathbf{A}}_o : (\mathbf{B}, (\mathbf{T} \times \mathbf{P}), \mathbf{E}, \mathbf{N}) \leftarrow \Delta_o \otimes \text{Parameter}_o^{\Delta}$
 - 28: $\overline{\mathbf{B}}_o : (\mathbf{B}, (\mathbf{T} \times \mathbf{P}), \mathbf{E}, \mathbf{N}) \leftarrow \Delta_o \otimes \mathbf{B}_o$
 - 29: # initialize h_o and y_o with Zeros
 - 30: $h_o : (\mathbf{B}, \mathbf{E}, \mathbf{N}) \leftarrow \text{Zeros} : (\mathbf{B}, \mathbf{E}, \mathbf{N})$
 - 31: $y_o : (\mathbf{B}, (\mathbf{T} \times \mathbf{P}), \mathbf{E}) \leftarrow \text{Zeros} : (\mathbf{B}, (\mathbf{T} \times \mathbf{P}), \mathbf{E})$
 - 32: # SSM recurrent
 - 33: **for** i in $\{0, \dots, L-1\}$ **do**
 - 34: $h_o = \overline{\mathbf{A}}_o[:, i, :, :] \odot h_o + \overline{\mathbf{B}}_o[:, i, :, :] \odot \mathbf{x}'_o[:, i, :, \text{None}]$
 - 35: $y_o[:, i, :] = h_o \otimes \mathbf{C}_o[:, i, :] + \mathbf{D}_o[\text{None}, :] \odot \mathbf{x}'_o[:, i, :]$
 - 36: **end for**
 - 37: # reshape $(\mathbf{T} \times \mathbf{P})$ to (\mathbf{T}, \mathbf{P})
 - 38: $y_o : (\mathbf{B}, \mathbf{T}, \mathbf{P}, \mathbf{E}) \leftarrow \text{Reshape}(y_o)$
 - 39: # flip the curve along the spatial dimension P
 - 40: **if** $o = \text{'backward'}$ **then**
 - 41: $y_o : (\mathbf{B}, \mathbf{T}, \mathbf{P}, \mathbf{E}) \leftarrow \text{Flip}(y_o)$
 - 42: **end if**
 - 43: **end for**
 - 44: # get gated y
 - 45: $y'_{forward} : (\mathbf{B}, \mathbf{T}, \mathbf{P}, \mathbf{E}), y'_{backward} : (\mathbf{B}, \mathbf{T}, \mathbf{P}, \mathbf{E}) \leftarrow y_{forward} \odot \text{SiLU}(\mathbf{z}), y_{backward} \odot \text{SiLU}(\mathbf{z})$
 - 46: # post normalization and residual connection
 - 47: $\mathbf{X}^{l+1'} : (\mathbf{B}, (\mathbf{T} \times \mathbf{P}), \mathbf{K}) \leftarrow \text{Linear}^{\mathbf{X}}(\text{LayerNorm}((y'_{forward} + y'_{backward})/2)) + \mathbf{X}^l$
 - 48: # adaptively normalize the output sequence $\mathbf{X}^{l+1'}$
 - 49: $\mathbf{X}^{l+1} : (\mathbf{B}, \mathbf{T}, \mathbf{P}, \mathbf{K}) \leftarrow \text{LOAN}_2(\mathbf{X}^{l+1'}, \mathbf{X}_{static})$
 - 50: # feed-forward layer and residual connection
 - 51: $\mathbf{X}^{l+1} : (\mathbf{B}, \mathbf{T}, \mathbf{P}, \mathbf{K}) \leftarrow \text{MLP}(\mathbf{X}^{l+1}) + \mathbf{X}^{l+1'}$
 - 52: # resort the input sequence along the P dimension
 - 53: $\mathbf{X}^{l+1} : (\mathbf{B}, \mathbf{T}, \mathbf{P}, \mathbf{K}) \leftarrow \text{Resort}(\mathbf{X}^{l+1}, S_{block})$
 - 54: **Return:** \mathbf{X}^{l+1}
-

E Evaluation metrics

To assess model performance, we used 8 metrics that are commonly used for hydrological modeling and flood forecasting evaluation [104]. This includes MAE (Mean Absolute Error), RMSE (Root Mean Square Error), R (Pearson Correlation Coefficient), R2 (Coefficient of Determination), KGE (Kling–Gupta Efficiency), Precision, Recall and F1 score. Below are the details about the individual metrics:

Mean Absolute Error (MAE) represents the average of the absolute differences between the predicted and observed values. It provides a straightforward measure of model accuracy. MAE is less sensitive to outliers than RMSE:

$$\text{MAE} = \frac{1}{P} \sum_{p=1}^P \left| \mathbf{X}_p^{\text{obs}} - \mathbf{X}_p^{\text{pred}} \right|, \quad (12)$$

where $\mathbf{X}_p^{\text{obs}}$ is the observed river discharge at point p , $\mathbf{X}_p^{\text{pred}}$ is the predicted river discharge, and P is the total number of points.

Root Mean Square Error (RMSE) measures the square root of the average squared differences between predicted and observed values. It penalizes large errors more heavily than MAE:

$$\text{RMSE} = \sqrt{\frac{1}{P} \sum_{p=1}^P (X_p^{\text{obs}} - X_p^{\text{pred}})^2}. \quad (13)$$

Pearson Correlation Coefficient (R) measures the linear relationship between observed and predicted values, ranging from -1 (perfect negative correlation) to $+1$ (perfect positive correlation):

$$R = \frac{\sum_{p=1}^P (X_p^{\text{obs}} - \bar{X}^{\text{obs}})(X_p^{\text{pred}} - \bar{X}^{\text{pred}})}{\sqrt{\sum_{p=1}^P (X_p^{\text{obs}} - \bar{X}^{\text{obs}})^2} \sqrt{\sum_{p=1}^P (X_p^{\text{pred}} - \bar{X}^{\text{pred}})^2}}, \quad (14)$$

where \bar{X}^{pred} is the mean of predicted river discharge, and \bar{X}^{obs} is the mean of observed river discharge.

Coefficient of Determination (R2) evaluates the predictive power of a model relative to the observed mean. It has the same meaning as Nash–Sutcliffe Efficiency (NSE) which is commonly used in hydrological modeling forecast. Values closer to 1 indicate better performance, while values below 0 suggest that the model performs worse than using the observed mean:

$$\text{R2} = 1 - \frac{\sum_{p=1}^P (X_p^{\text{obs}} - X_p^{\text{pred}})^2}{\sum_{p=1}^P (X_p^{\text{obs}} - \bar{X}^{\text{obs}})^2}. \quad (15)$$

Kling–Gupta Efficiency (KGE) is a composite metric that combines correlation, bias, and variability. It addresses some weaknesses of NSE by ensuring balance across multiple aspects of model performance. Like NSE, values near 1 indicate good performance, while values below 0 indicate performance worse than the observed mean:

$$\text{KGE} = 1 - \sqrt{(r - 1)^2 + (\beta - 1)^2 + (\gamma - 1)^2}, \quad (16)$$

$$\beta = \frac{\bar{X}^{\text{pred}}}{\bar{X}^{\text{obs}}}, \quad \gamma = \frac{\text{CV}^{\text{pred}}}{\text{CV}^{\text{obs}}}, \quad r = \text{Pearson correlation coefficient}. \quad (17)$$

where r is the Pearson correlation between observed and simulated, β is the bias ratio, γ is the variability ratio, and $\text{CV}^{\text{obs}} = \sigma^{\text{obs}} / \bar{X}^{\text{obs}}$ and $\text{CV}^{\text{pred}} = \sigma^{\text{pred}} / \bar{X}^{\text{pred}}$ are the coefficients of variation, where σ^{obs} and σ^{pred} are the standard deviations of the observed and predicted river discharge, respectively. In this work, we multiple KGE by 100 in the tables for a better comparison.

Precision is the proportion of correctly identified positive cases (i.e., flood events) among all predicted positives. High precision indicates a low false-positive rate:

$$\text{Precision} = \frac{TP}{TP + FP}, \quad (18)$$

where TP is the number of true positives and FP is the number of false positives.

Recall is the proportion of correctly identified positives among all actual positives. High recall indicates a low false-negative rate:

$$\text{Recall} = \frac{TP}{TP + FN}, \quad (19)$$

where FN is the number of false negatives.

F1-score is the harmonic mean of precision and recall, particularly useful in imbalanced classification tasks (i.e., flood detection where flood events are rare):

$$F1 = 2 \cdot \frac{\text{Precision} \cdot \text{Recall}}{\text{Precision} + \text{Recall}}. \quad (20)$$

In this work, we multiple F1-score in the tables by 100 for a better comparison.

In this study, the metrics (12)-(16) are used to evaluate the agreement between observed and forecast discharge time series. During the evaluation, these metrics are calculated on the time series at single grid points and then averaged over all the grid points. The metrics (18)-(20) are applied to assess the model's ability to detect flood events at different return periods. For example, on a day classified as exceeding the 2-year return period threshold, a correct prediction of discharge above this threshold is considered a true positive. If not otherwise specified, we report F1-score averaged over 1.5-20 year return periods and all 3366 points.

F Ablation studies

For the ablation studies, we conducted experiments over the European domain (60°N 30°S, −10°W 40°E) which has 82,804 points from the filtered diagnostic river points defined in Sec. A.7 and includes 675 GRDC stations for evaluation.

F.1 Mamba vs. Transformer

In Fig. 12, we compare the model using Mamba blocks to a variant using Transformer blocks with Flash-Attention [80, 81]. Both Mamba and Flash-Attention have linear complexity. However, Mamba scales better with number of input tokens (Fig. 12 (left)), important for global modeling. The Transformer-based approach becomes computationally infeasible for a larger number of input points. Both approaches have similar memory consumption except that using the bidirectional Mamba block increases the memory consumption slightly (Fig. 12 (right)).

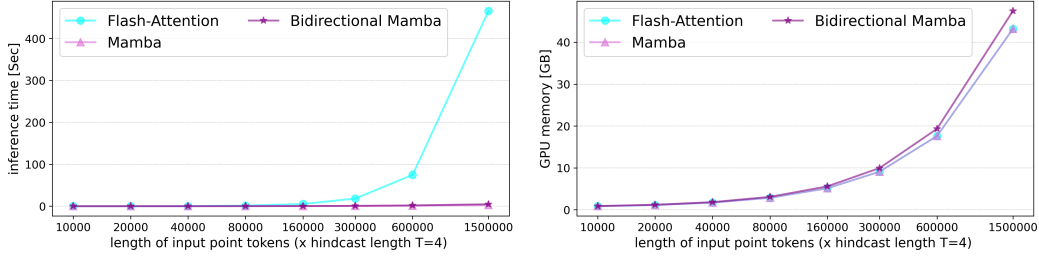


Figure 12: Comparison between Mamba and Transformer-based backbones.

Table 9 shows a comparison between Mamba and Flash-Attention regarding training time with different configurations. Since Flash-Attention does not scale with global data, we split the space-filling curve and do a local modeling (see Fig.14 (b)). This requires rearranging the curves at each block, which becomes the main bottleneck for Flash-Attention compared to Mamba.

Table 9: Training time on the reanalysis data for 1 epoch (1,529,667 points).

Model	Time (min)	GPUs	CPUs
Flash-Attention	~ 145	16 × A100	64 × 4
Mamba	~ 82	16 × A100	64 × 4

Table 10 shows the results for RiverMamba with different backbones. Flash-Attention and Mamba2 [107] achieve slightly lower performance compared to Mamba.

Table 10: Ablation studies for the RiverMamba backbone on the validation set over Europe.

Backbone	# Params	KGE F1 (↑)
Flash-Attention	5.03 M	91.61 28.04
Mamba	4.38 M	92.05 28.75
Mamba2	4.02 M	91.69 27.93

F.2 Feature importance

In Table 11, we study the performance of RiverMamba with different input features. All input features have an impact on the performance. Removing the observational CPC data only slightly reduces the results for GloFAS reanalysis, but the decrease is larger for observational GRDC. Removing GloFAS reanalysis and ERA5-Land initial conditions reduces the performance as well, but GloFAS reanalysis is more important. Removing the meteorological forcing forecasts HRES has the biggest impact since weather forecasting is an important source of information. The best performance is achieved when we use all input variables.

Table 11: Ablation studies for feature importance on the validation set over Europe.

Static (LISFLOOD)	CPC	ERA5	GloFAS-reanalysis	HRES	KGE F1 (\uparrow) (Reanalysis)	KGE F1 (\uparrow) (GRDC Obs)
\times	\checkmark	\checkmark	\checkmark	\checkmark	90.91 25.05	76.33 11.18
\checkmark	\times	\checkmark	\checkmark	\checkmark	91.51 28.42	76.81 11.02
\checkmark	\checkmark	\times	\checkmark	\checkmark	90.77 25.21	77.31 11.10
\checkmark	\checkmark	\checkmark	\times	\checkmark	90.60 24.50	75.21 12.26
\checkmark	\checkmark	\checkmark	\checkmark	\times	79.72 12.76	67.57 06.40
\checkmark	\checkmark	\checkmark	\checkmark	\checkmark	92.05 28.75	78.38 13.35

F.3 Pretraining on Reanalysis

In Table 12, we show the value of pretraining on GloFAS reanalysis data for the GRDC prediction. From our experiments, we can see a clear benefit of training on river discharge reanalysis before training the model on GRDC observations.

Table 12: Ablation studies for pretraining on GloFAS reanalysis on the validation set over Europe.

Pretrained on GloFAS reanalysis	KGE F1 (\uparrow)
\times	74.06 08.82
\checkmark	78.38 13.35

F.4 Space-filling curves

In Table 13, we investigate the impact of various serialization patterns for RiverMamba. Our experiments show that sweep curves perform better than the other curves. Iterating between sweep and Gilbert curves (fourth column) improves the F1-score further. Iterating over all curves improves F1-score, but decreases KGE. For simplicity, we use thus the combination of sweep and Gilbert curves for our experiments.

Table 13: Ablation studies for space-filling curves on the validation set over Europe. The columns indicate the serialization patterns: G for Gilbert, Z for Zigzag, S for Sweep, Shuffle represents shuffling the order inside the hindcast layers. S and Z Curves use both direction H and V and G uses both regular and trans versions.

Space-filling curve	G	Z	S	S + G	S + G + Z
KGE F1 (\uparrow)	91.56 27.33	91.56 27.19	92.05 28.26	92.05 28.75	91.63 29.62

In Table 14, we remove the spatial modeling in RiverMamba completely and do the scanning only along the temporal dimension (first row). The results show the importance of spatiotemporal modeling.

Table 14: Ablation regarding the spatiotemporal modeling on the validation set over Europe.

Temporal modeling	Spatiotemporal modeling	KGE F1 (\uparrow)
\checkmark	\times	87.26 19.52
\times	\checkmark	92.05 28.75

The design of the scanning also plays a role. From Table 15 (a), we found that sequential scanning along the spatial dimension (P) works better. This is represented as scanning from P to T ($P \rightarrow T$). In other words, the points are connected over time by scanning at time step t and continuing the scan at $t + 1$. In the second case ($T \rightarrow P$), each point will be scanned along the time dimension (T) and then connected to the next point along the spatial dimension P .

Table 15: Ablation studies for scan patterns on the validation set over Europe.

(a) Curve order			(b) Curve type			(c) Bidirectional Curve		
T→P	P→T	KGE F1 (↑)	Local	Global	KGE F1 (↑)	SSM	Bi-SSM	KGE F1 (↑)
✓	✗	91.53 28.07	✓	✗	91.64 28.93	✓	✗	91.13 24.82
✗	✓	92.05 28.75	✗	✓	92.05 28.75	✗	✓	92.05 28.75

In Table 15 (b), we split the curve into local curves similar to PointTransformer [108] (Fig. 14 (b)). Using a global receptive field gives the model more capability to extract up- and downstream features and to model adjacent catchments. In addition, local modeling needs more computations along the network i.e., sorting, resorting and padding. Finally, bidirectional Mamba (Table 15 (c)) collects information about the streamflow from both side of the curve thus covering the whole domain and achieving a better performance than unidirectional Mamba.

For training and inference on the global dataset, it is impractical to fit all the input points (~ 6 million points) into the memory. For this, we first define a Gilbert space-filling curve on the globe and then we split the curve into smaller curves along the space-filling curve, i.e., we split the curve into sequences with ~ 311 K points for each. A simplified version of the splits is shown in Fig. 13.



Figure 13: A simplified view of splitting along Gilbert space-filling curve.

G Baselines

G.1 Climatology

We followed [16] to define the climatology baseline. For this, we computed climatology for the long-term record of river discharge data (1979-2018) with a moving window of 31 days centered on the day-of-the-year. Then, we computed 11 fixed quantiles at 10% interval for each day-of-the-year. As a result, the climate distribution changes with lead time, reflecting the dynamic changes in local river discharge patterns over time. Climatology is commonly applied to medium- and extended range lead times, where seasonal patterns predominantly influence the river discharge forecast [16].

G.2 Persistence

We defined the persistence baseline as the daily river discharge of GloFAS reanalysis from the day preceding the day at which the forecast was issued, i.e., for a forecast starting at 00:00 UTC \mathbf{X}^t , the persistence is defined as the averaged river discharge between 00:00 UTC \mathbf{X}^{t-1} and 00:00 UTC \mathbf{X}^t . This value was used as a prediction for the entire lead time. Persistence is primarily applied to short lead times, where the correlation of sequential river discharge values predominantly influences the forecasts [16]. Note that this baseline is unrealistic since no reanalysis is available directly at time t .

G.3 LSTM

To ensure fair comparison and benchmarking, we adopted the same LSTM architecture as described in [24]. The model follows an encoder–decoder structure, where the encoder is a bi-directional “hindcast” LSTM that processes historical input data, and the decoder is a uni-directional “forecast” LSTM that generates predictions over a 7-day forecast horizon based on forecast inputs. We used the same dataset, train–test split, and normalization strategies as in the RiverMamba model. To remain consistent with [24], we trained the model only at locations with available gauge observations—specifically the 3366 GRDC stations (see Sec. A.2) rather than using a global training setup. The model leverages both dynamic and static inputs. For the hindcast LSTM, we used a 14-day sequence of dynamic inputs including CPC precipitation, GloFAS reanalysis, and ERA5-Land reanalysis data. At each time step, static attributes derived from the LISFLOOD model are embedded and concatenated with the dynamic inputs. For the forecast LSTM, we used ECMWF HRES forecasts as dynamic inputs over the 7-day horizon, with the static attributes concatenated in the same manner.

To connect the encoder and decoder, we employed a “state” layer consisting of two transfer networks: a linear cell-state transfer network and a nonlinear hidden-state transfer network (a fully connected layer with hyperbolic tangent activation). A linear output head is applied at each forecast step to predict streamflow, and the model is trained using the mean squared error (MSE) loss. Unlike [24], we focus on deterministic prediction, so we do not implement a probabilistic output head or probabilistic loss function. In total, the model has 834,421 parameters.

The reported LSTM results are averaged over an ensemble of three independently trained models, each initialized with a different random seed. Each training batch contains data from all 3366 GRDC stations at a given time step, with a batch size of 1—effectively training on 3366 samples per mini-batch. Training takes approximately 12 hours on four NVIDIA A100 GPUs for 35 epochs. More details about the model architecture can be found in Extended Data Fig. 4 and the Methods section of [24], as well as in the NeuralHydrology GitHub repository (<https://neuralhydrology.github.io/>). Table 16 summarizes the key hyperparameters used in our implementation of the LSTM model.

It is important to note that [24] did not release the full code or the full hyperparameter configurations of their final model—only the pretrained checkpoints were made available. We therefore used the published checkpoints and the NeuralHydrology GitHub repository.

In Sections J.1 and J.2, we compare with the generated reforecast obtained from [24]. In [24], an input sequence length of 365 days was used. In our experiments, we also trained the LSTM model using a range of input sequence lengths from 4 to 90 days. We observed only marginal performance gains beyond a certain point, and identified 14 days as an optimal input sequence length.

Table 16: Implementation details of the LSTM model.

Configuration	Value
Hidden size in hindcast LSTM	256
Hidden size in forecast LSTM	128
Hidden size in static embedding layer	20
Hidden size in dynamic embedding layer	20
Hidden size in state layer	128
Number of layers	1
Dropout at output regression head	0.4
Dropout at state layer	0.1
Learning rate	0.0003
Learning rate scheduler	Cosine annealing
Batch size	1 with (3366 samples)
Optimizer	Adam
beta1 momentum term	0.9
beta2 momentum term	0.999
weight decay	0

G.4 GloFAS Forecast

Operational forecast from GloFAS was obtained from the ECMWF Early Warning Data Store (EWDS) <https://doi.org/10.24381/cds.ff1aef77>. This represents real-time data from the official system for operational flood forecasting from the Copernicus Emergency Management Service (CEMS) and managed and developed by the European Commission’s Joint Research Centre. GloFAS forecast is produced by forcing the LISFLOOD model with the ECMWF ensemble forecast (ENS) up to 30 days. Note that GloFAS forecast uses ENS meteorological forcing twice a day at 00:00 UTC and 12:00 UTC. The high-resolution GloFAS v.4.0 forecast is available from 2023-07-26. We compare to this baseline in Sec. J.5.

G.5 GloFAS Reforecast

This baseline is similar to GloFAS forecast (Sec. G.4), however, GloFAS reforecast are forecasts run over the past with the new system version 4.0. The reforecast is available until 2023 and does not span the full testing split. We use this baseline for the main comparison with GloFAS in the main paper and in Sec. J.4.

H Space-filling curves

Serialized encoding maps a point’s position into an integer index representing its order within the given space-filling curve. Each point is stored as a 64-bit integer. For simplicity, we define the curves on the 2D PlateCarree projection of the Earth. As illustrated in Figs. 15 and 16, the serialization is done according to the sorted serialized encoding of all points with $\Phi : \mathbb{Z}^3 \rightarrow \mathbb{N}$.

Due to the nature of the bijective transformation, there is an inverse mapping $\Phi^{-1} : \mathbb{N} \rightarrow \mathbb{Z}^3$ which allows for the mapping of the encoded index back into the point’s position $p_i \in \mathbb{Z}^3$ (or $p_i \in \mathbb{R}^3$ in case of a continuous space). This inverse mapping is called the serialized decoding or the deserialization.

In the following, we describe the mapping for each curve:

Sweep. This curve fills in the space like a spherical helix or a Luxodrome around the sphere.

Zigzag. This curve is similar to the Sweep curve. The main difference is that the transformation ensures that every neighboring points on the curve are also neighboring in the physical space.

Generalized Hilbert. Generalized Hilbert (Gilbert) is a Hilbert space-filling curve [83] for a rectangular domains of arbitrary non-power of two sizes [110]. We used the numpy implementation of (<https://github.com/jakubcerveny/gilbert>) to generate the curves.

Transposed Gilbert is generated as $y_{(transpose)} = H - y$, where $y \in [1, H]$.

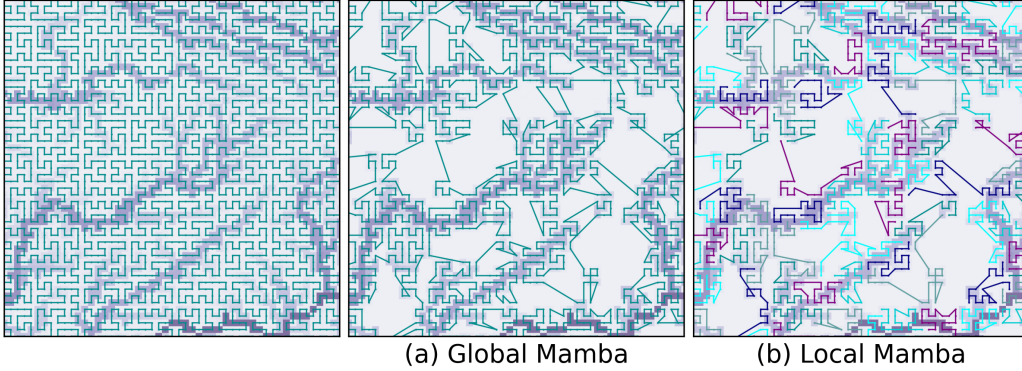


Figure 14: Illustration of the difference between global curve (middle) and grouped local curves (right). The left image shows a Gilbert space-filing curve for all points. In our experiments, the global curve is used (middle). For the experiments with Flash-Attention, we use the local curves (right).

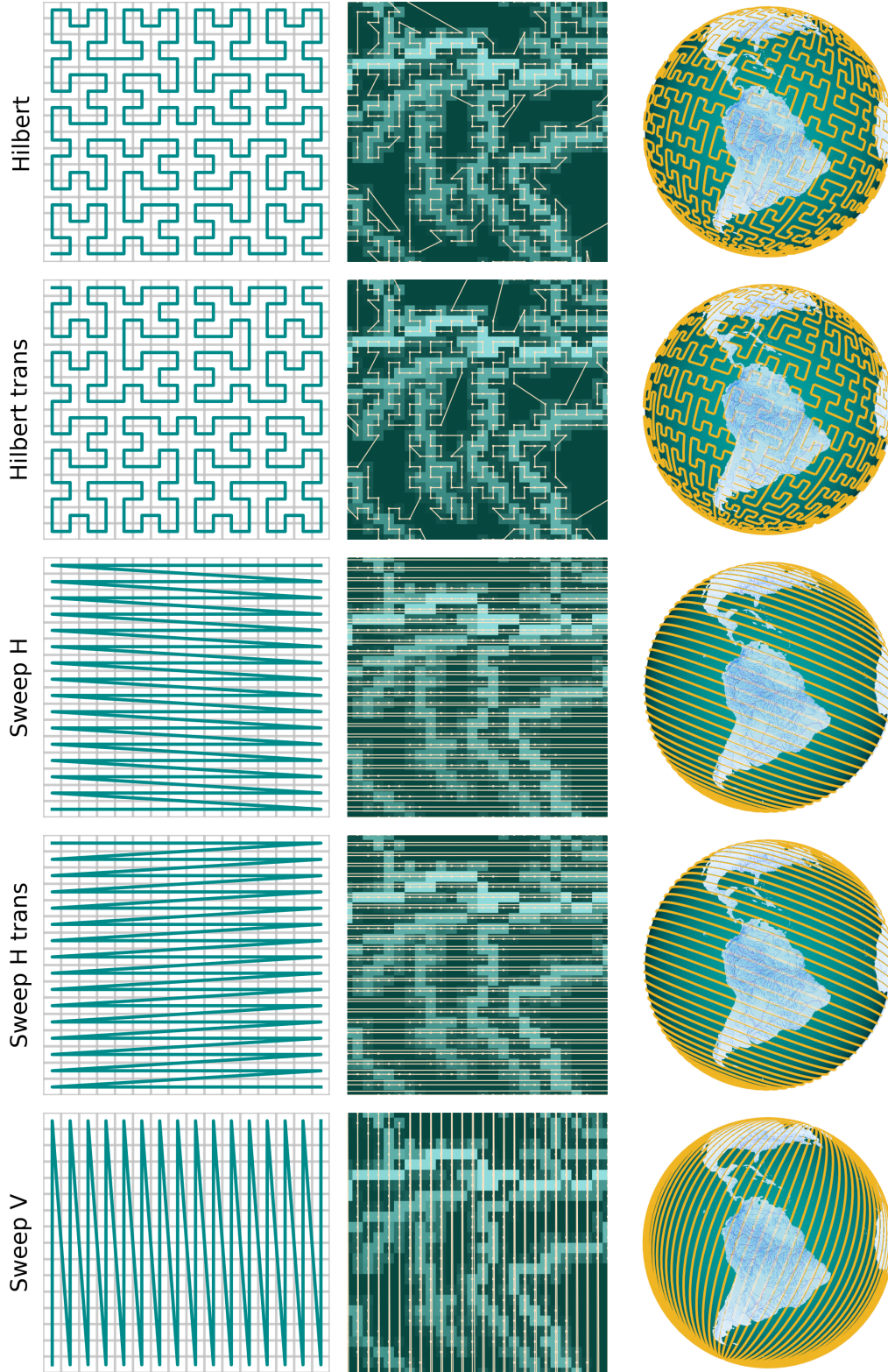


Figure 15: Visualization of different types of space-filling curves. For each type, we show the space-filling curve over a 2D discrete space (left), zoomed in version over the Earth where the points are sorted via a specific serialization order within the space-filling curve (middle), and simplified 3D visualization of the curve over the Earth (right).

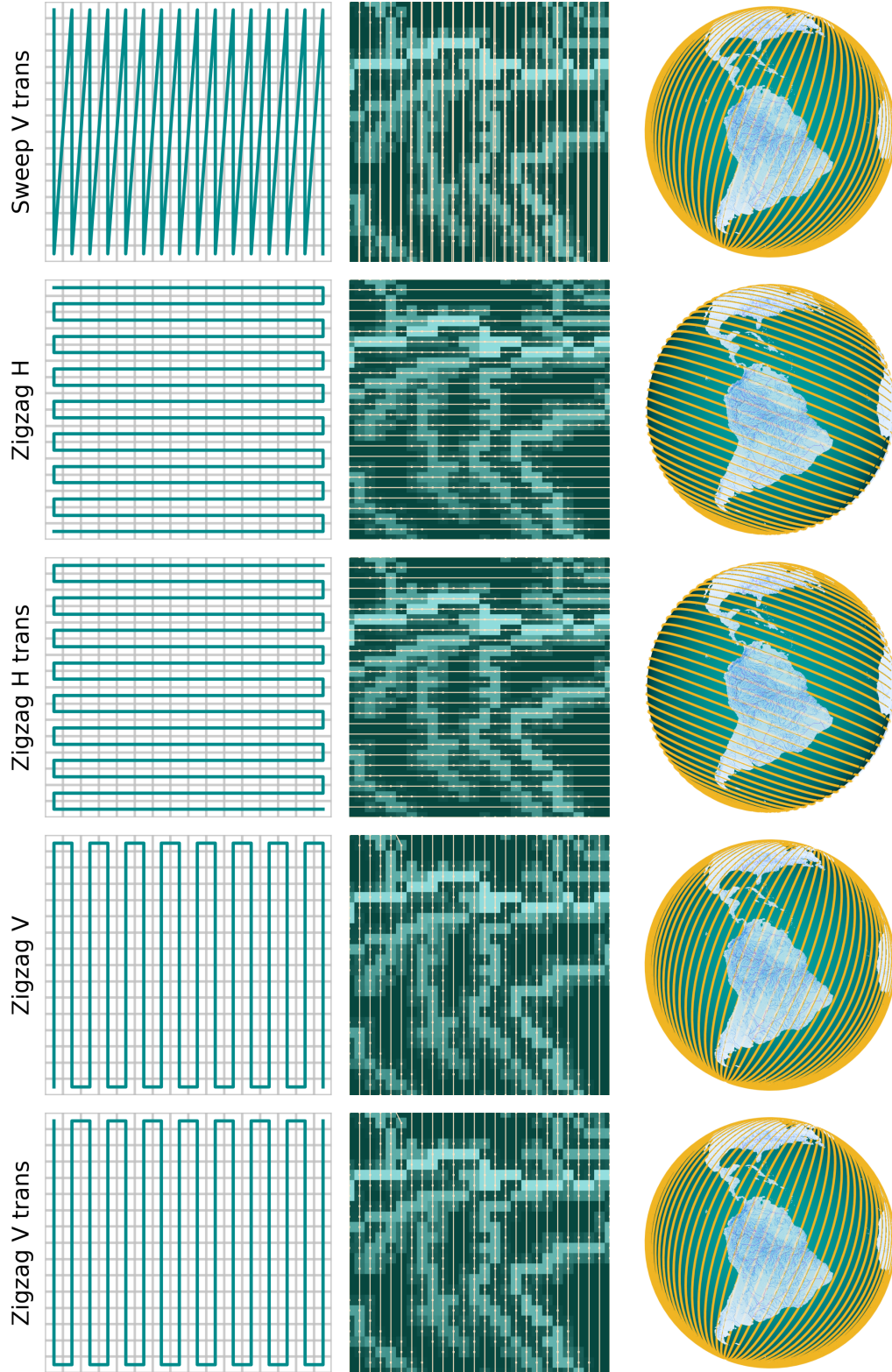


Figure 16: Visualization of different types of space-filling curves. For each type, we show the space-filling curve over a 2D discrete space (left), zoomed in version over the Earth where the points are sorted via a specific serialization order within the space-filling curve (middle), and simplified 3D visualization of the curve over the Earth (right).

I Experiments on HydroRIVERS

HydroRIVERS data are widely used to train deep learning models in hydrology. In this section, we explore the performance of RiverMamba with HydroRIVERS [102, 103]. For this, we obtained static river attributes from (<https://www.hydrosheds.org/products/hydrorivers>). The data is stored as a shape file. To map them onto the GloFAS domain, we first extract the coordinates of the rivers and then project them with the grid points on the WGS-84 ellipsoid (Eq. 9 and 10). Then, for each GloFAS grid point, depending on the attribute type, we either average the attributes or take the most frequent attribute within a radius of 5 km. If no attributes were found, we increase the radius to 12 km, and 24 km, respectively. We processed 299 river feature attributes overall and experimented with 103 features, i.e., we removed the monthly attribute statistics from the static features. Fig.17 gives an overview of the processed HydroRIVERS data.

In Table 17, we compare the LISFLOOD with the HydroRIVERS static maps for prediction on both GloFAS reanalysis and GRDC data. Using HydroRIVERS performs worse than using LISFLOOD static maps.

Table 17: Ablation studies on the validation set over Europe.

HydroRIVERS	LISFLOOD	KGE F1 (↑) (Reanalysis)	KGE F1 (↑) (GRDC Obs)
X	X	90.91 25.05	76.33 11.18
✓	X	91.74 26.22	74.06 12.27
X	✓	92.05 28.75	78.38 13.35

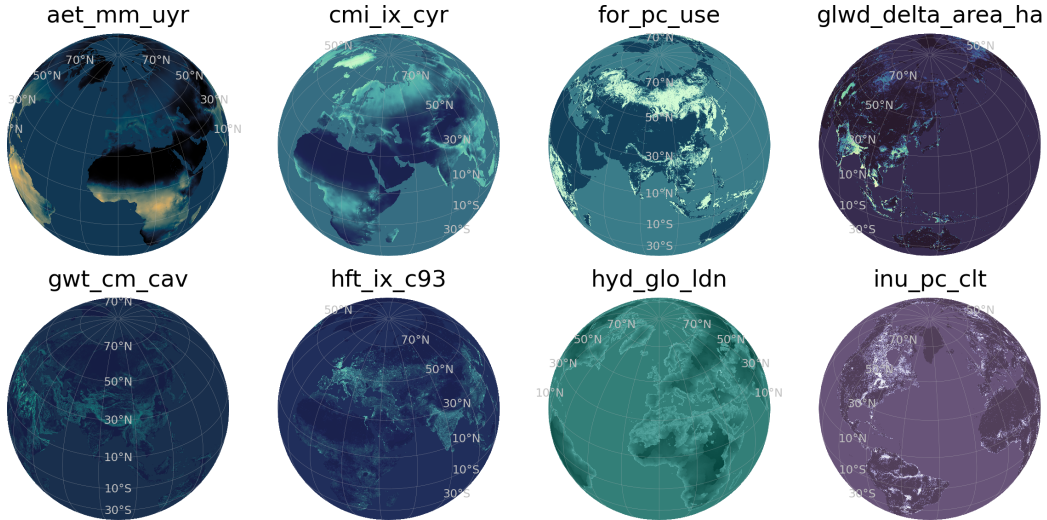


Figure 17: An overview of the processed HydroRIVERS static features. HydroRIVERS is mapped into the GloFAS domain.

J Additional results

J.1 Comparison with Google reforecast on ungauged GRDC

In this section, we evaluate RiverMamba against the published reforecast by [24] and available from [111]. For this, we split our data into 8 folds and evaluate on ungauged stations. All stations were predicted similar to [24] where each station was evaluated out-of-sample in both time and space. Note that the LSTM model for Google reforecast used more stations (~ 5680), while we used much less stations (3366). In addition, LSTM takes one year input as a hindcast, while RiverMamba takes only 4 days as input. Furthermore, RiverMamba does not use weather forecast at the nowcasting and shifts the input initial conditions to mimic an operational forecast. There are also differences in the input initial conditions, i.e., LSTM uses precipitation estimates from the NASA Integrated Multi-satellite Retrievals for GPM (IMERG) early run as input. In addition, it uses HydroATLAS [103] as geophysical and anthropogenic basin attributes. RiverMamba uses GloFAS reanalysis as an initial condition and LISFLOOD as static basin attributes.

Table 18 shows the overall performance for the years 2014-2021. F1-score is averaged for all lead times and 1.5-20 year return periods.

More results are shown in Figs.18-20.

Table 18: Comparison to Google reforecast on ungauged GRDC stations for the years 2014-2021. Shown is the averaged F1-score (\uparrow) for all lead times and 1.5-20 year return periods.

LSTM (Google reforecast from [24])	RiverMamba
21.64	23.55

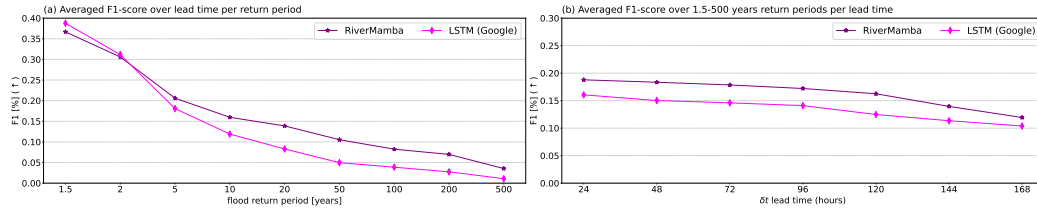


Figure 18: Comparison to Google reforecast on ungauged GRDC stations (test set 2014-2021 out-of-sample in space and time).

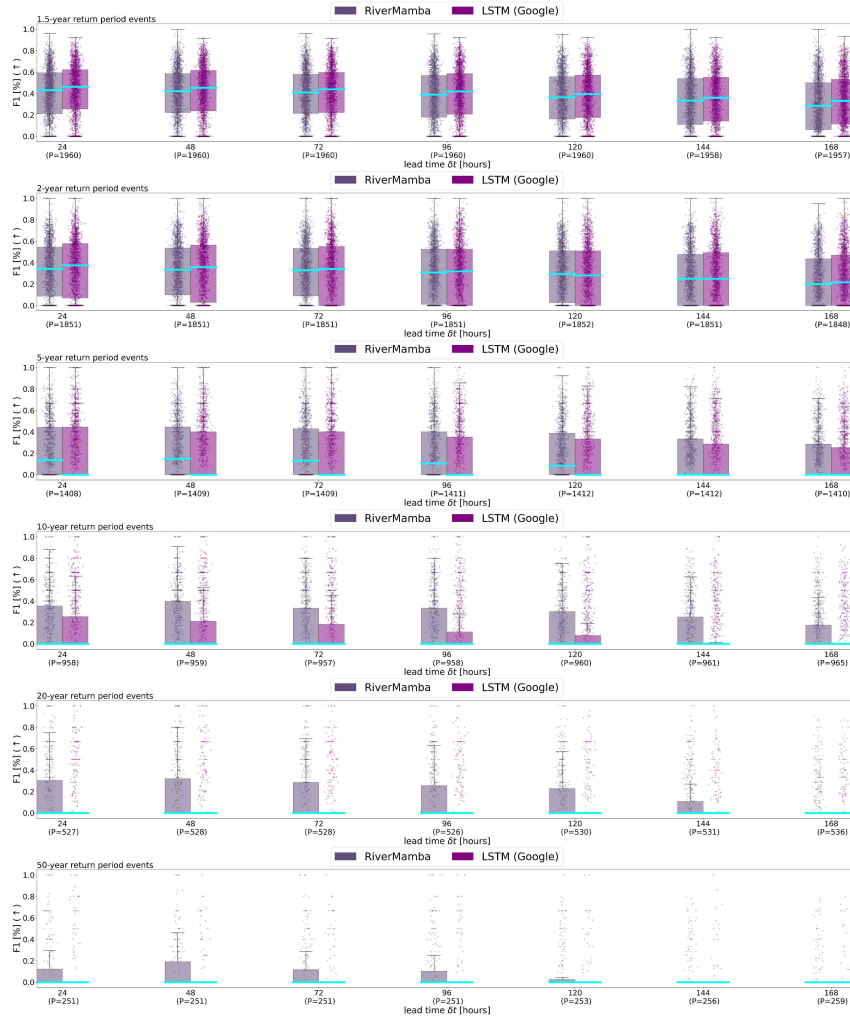


Figure 19: Comparison to Google reforecast. Shown is F1-score of flood forecasting for different return periods with lead time on ungauged GRDC stations (test set 2014-2021 out-of-sample in space and time). Distribution quartiles are displayed in boxes, and the entire range excluding outliers is displayed in whiskers. The median score for the model is shown by the cyan line in the box.



Figure 20: Comparison to Google reforecast. Shown is F1-score of flood forecasting for different lead time with return periods (1.5 - 50 years) on ungauged GRDC stations (test set 2014-2021 out-of-sample in space and time). Distribution quartiles are displayed in boxes, and the entire range excluding outliers is displayed in whiskers. The median score for the model is shown by the cyan line in the box.

J.2 Comparison with Google reforecast on gauged GRDC

Similar to Section J.1, here we compare to the published reforecast by [24] and available from [111] but on gauged stations where all stations were evaluated out-of-sample in time for the years 2019-2021. For the differences between RiverMamba and the LSTM model by [24], see Sec. J.1.

Table 19 shows the overall performance for the years 2019-2021. F1-score is averaged for all lead times and 1.5-20 year return periods. More results are shown in Figs. 21-23.

Table 19: Comparison to Google reforecast on gauged GRDC stations for the years 2019-2021. Shown is the averaged F1-score (\uparrow) for all lead times and 1.5-20 year return periods.

LSTM (Google reforecast from [24])	RiverMamba
23.18	25.87

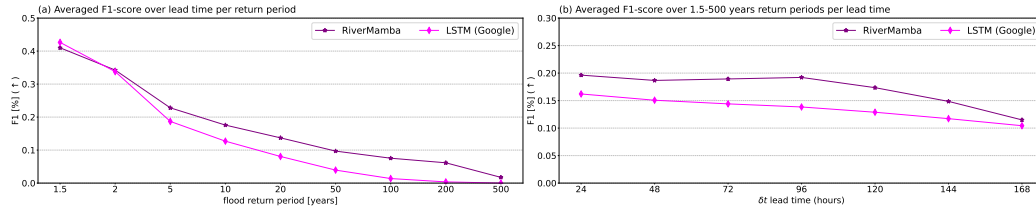


Figure 21: Comparison to Google reforecast on gauged GRDC stations (test set 2019-2021 out-of-sample in time).

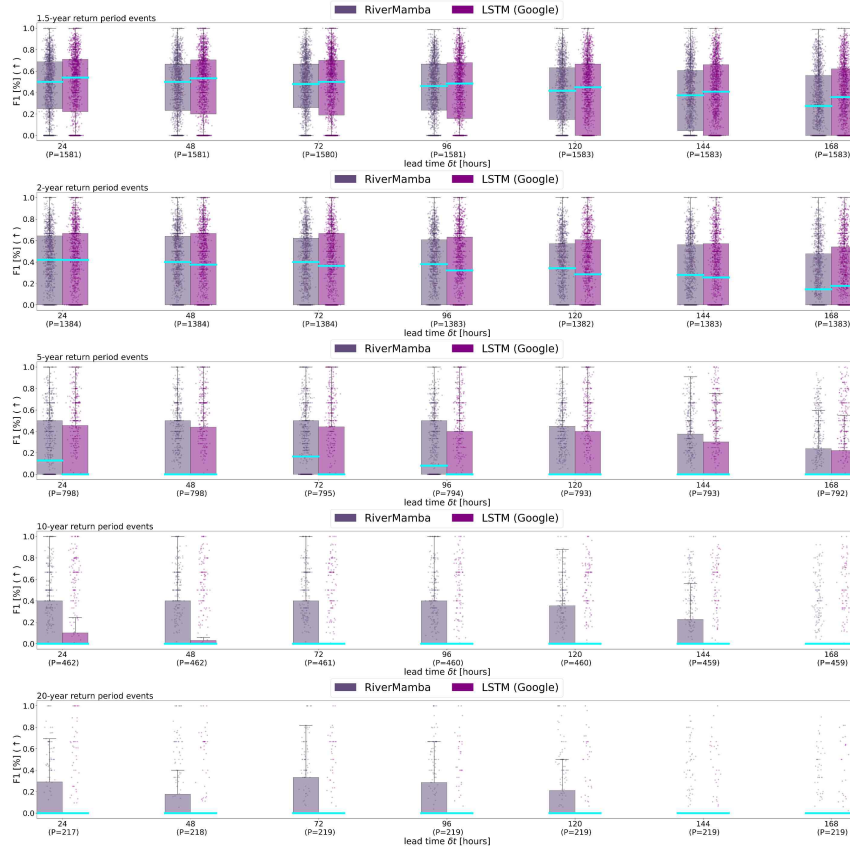


Figure 22: Comparison to Google reforecast. Shown is F1-score of flood forecasting for different return periods with lead time on gauged GRDC stations (test set 2019-2021 out-of-sample in time). Distribution quartiles are displayed in boxes, and the entire range excluding outliers is displayed in whiskers. The median score for the model is shown by the cyan line in the box.

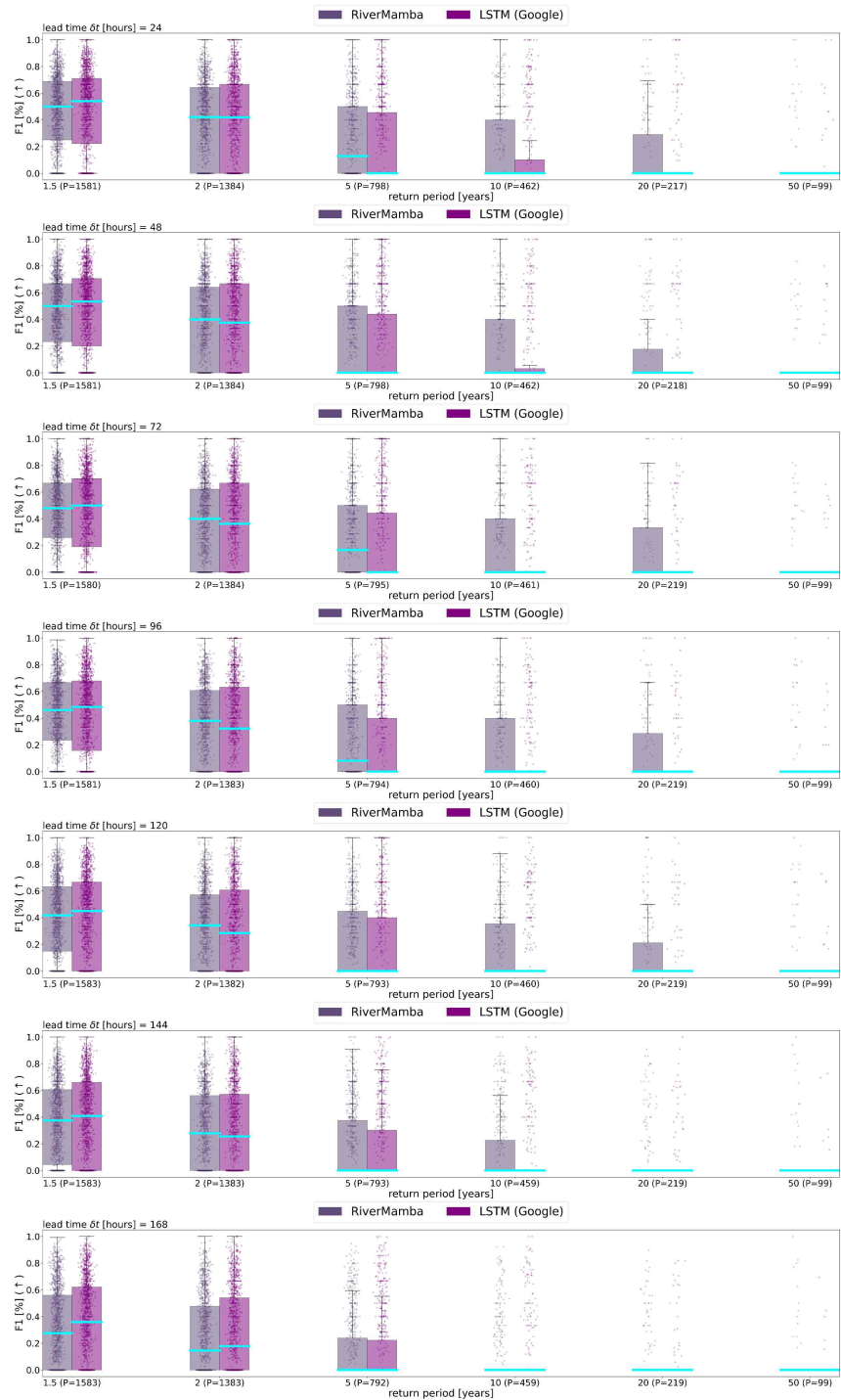


Figure 23: Comparison to Google reforecast. Shown is F1-score of flood forecasting for different lead time with return periods (1.5 - 50 years) on gauged GRDC stations (test set 2019-2021 out-of-sample in time). Distribution quartiles are displayed in boxes, and the entire range excluding outliers is displayed in whiskers. The median score for the model is shown by the cyan line in the box.

J.3 Additional results on gauged GloFAS reanalysis

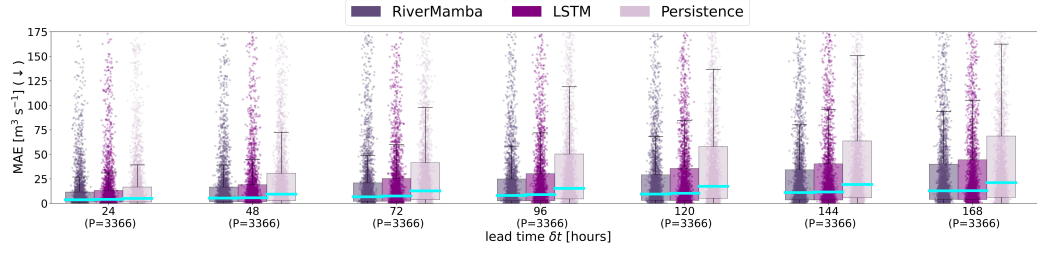


Figure 24: MAE of the river discharge forecasting with different lead time on GloFAS reanalysis (test set 2021-2024 temporally out-of-sample).

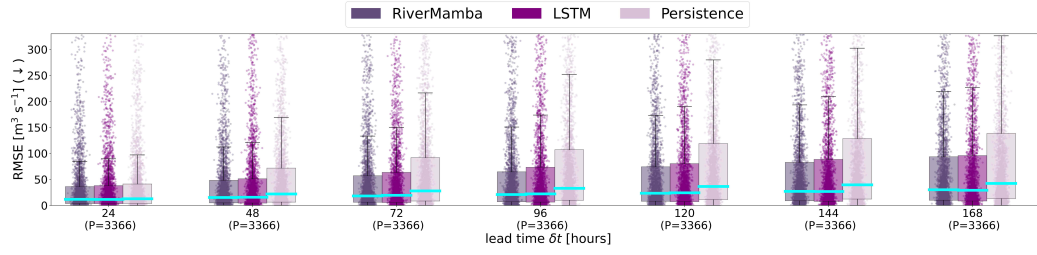


Figure 25: RMSE of the river discharge forecasting with different lead time on GloFAS reanalysis (test set 2021-2024 temporally out-of-sample).

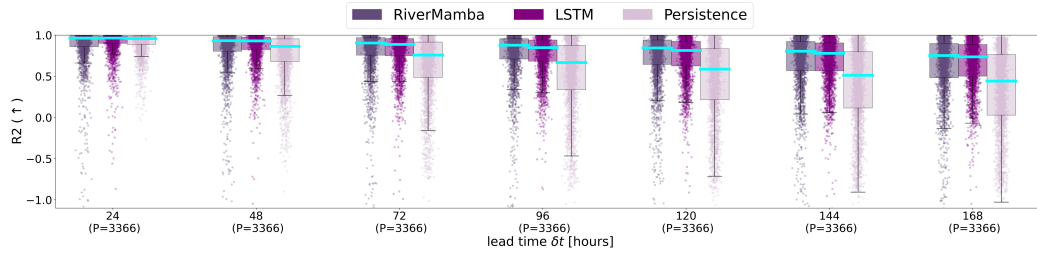


Figure 26: R^2 (NSE) of the river discharge forecasting with different lead time on GloFAS reanalysis (test set 2021-2024 temporally out-of-sample).

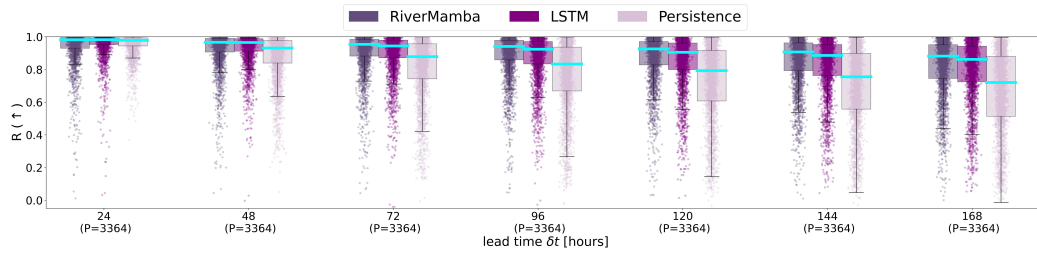


Figure 27: Pearson correlation (R) of the river discharge forecasting with different lead time on GloFAS reanalysis (test set 2021-2024 temporally out-of-sample).



Figure 28: F1-score of flood forecasting for different return periods with lead time on GloFAS reanalysis (test set 2021-2024 temporally out-of-sample). Distribution quartiles are displayed in boxes, and the entire range excluding outliers is displayed in whiskers. The median score for the model is shown by the cyan line in the box.



Figure 29: Precision of flood forecasting for different return periods with lead time on GloFAS reanalysis (test set 2021-2024 temporally out-of-sample). Distribution quartiles are displayed in boxes, and the entire range excluding outliers is displayed in whiskers. The median score for the model is shown by the cyan line in the box.



Figure 30: Recall of flood forecasting for different return periods with lead time on GloFAS reanalysis (test set 2021-2024 temporally out-of-sample). Distribution quartiles are displayed in boxes, and the entire range excluding outliers is displayed in whiskers. The median score for the model is shown by the cyan line in the box.



Figure 31: F1-score of flood forecasting for different lead time with return periods (1.5 - 50 years) on GloFAS reanalysis (test set 2021-2024 temporally out-of-sample). Distribution quartiles are displayed in boxes, and the entire range excluding outliers is displayed in whiskers. The median score for the model is shown by the cyan line in the box.

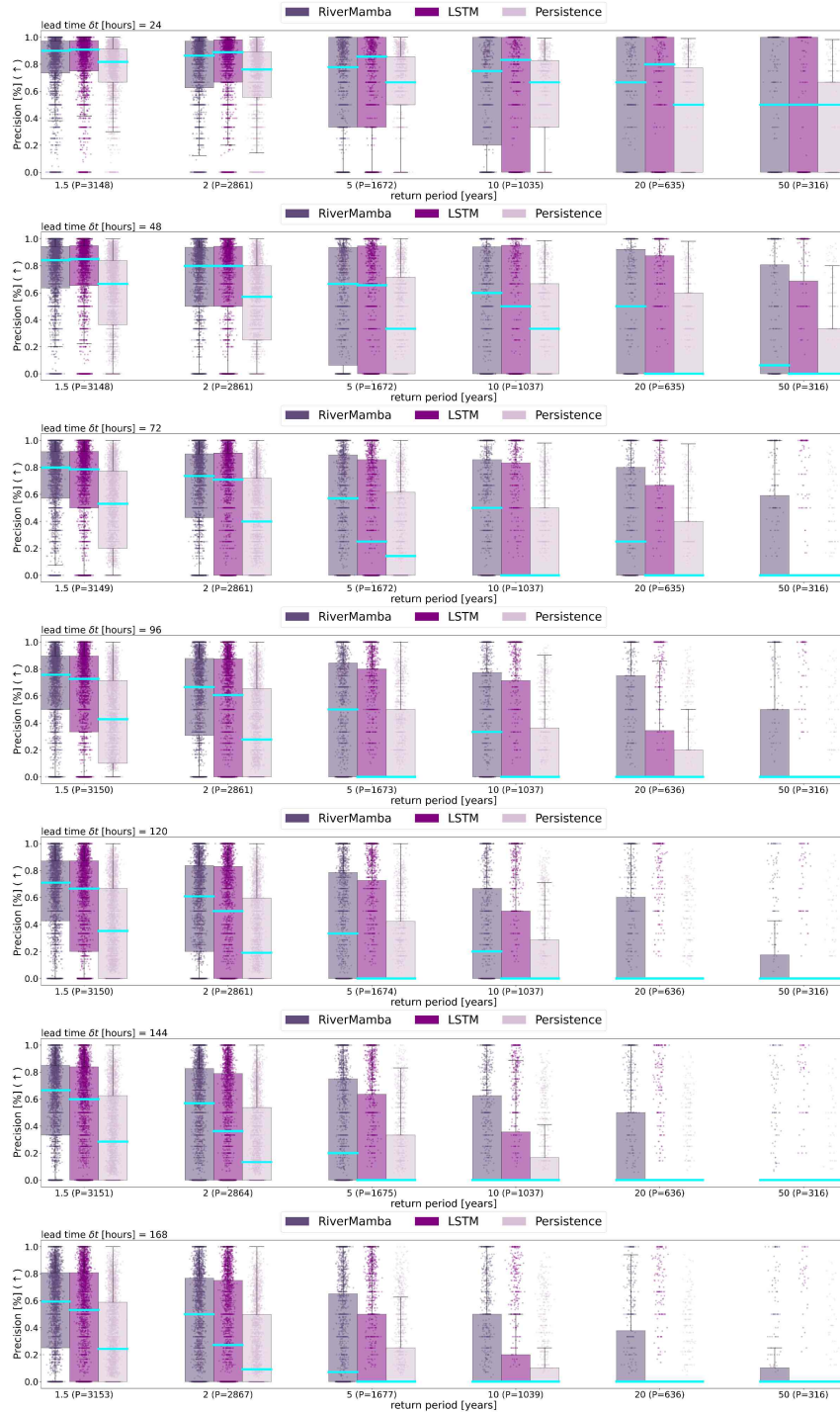


Figure 32: Precision of flood forecasting for different lead time with return periods (1.5 - 50 years) on GloFAS reanalysis (test set 2021-2024 temporally out-of-sample). Distribution quartiles are displayed in boxes, and the entire range excluding outliers is displayed in whiskers. The median score for the model is shown by the cyan line in the box.

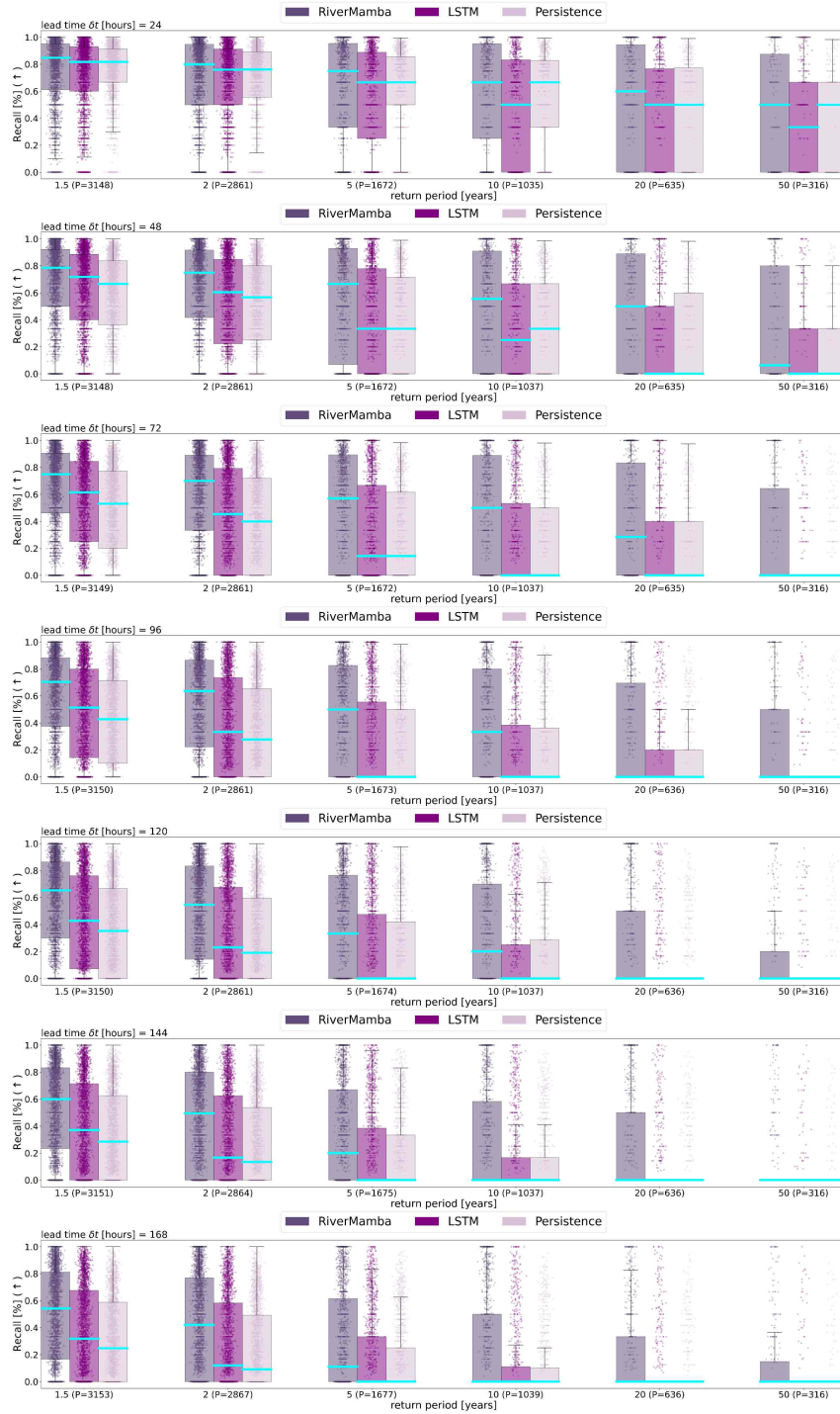


Figure 33: Recall of flood forecasting for different lead time with return periods (1.5 - 50 years) on GloFAS reanalysis (test set 2021-2024 temporally out-of-sample). Distribution quartiles are displayed in boxes, and the entire range excluding outliers is displayed in whiskers. The median score for the model is shown by the cyan line in the box.

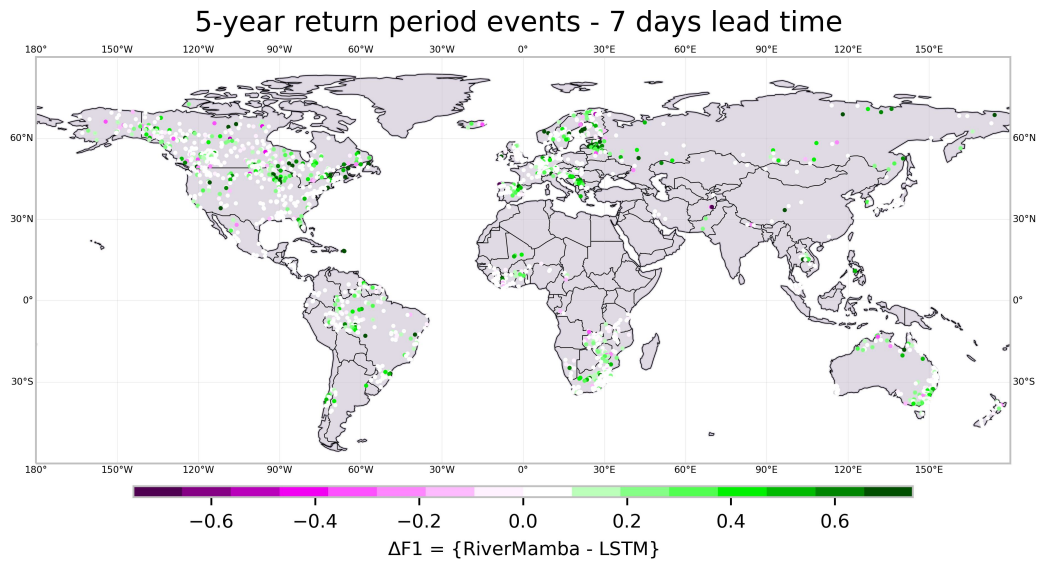


Figure 34: Comparison of F1-score between RiverMamba and LSTM (Google) on GloFAS reanalysis for the 5-year return period events (test set 2021-2024 temporally out-of-sample). RiverMamba improves over LSTM in 41% of the stations ($P=1677$) and being better or equally better in 89% of the stations.

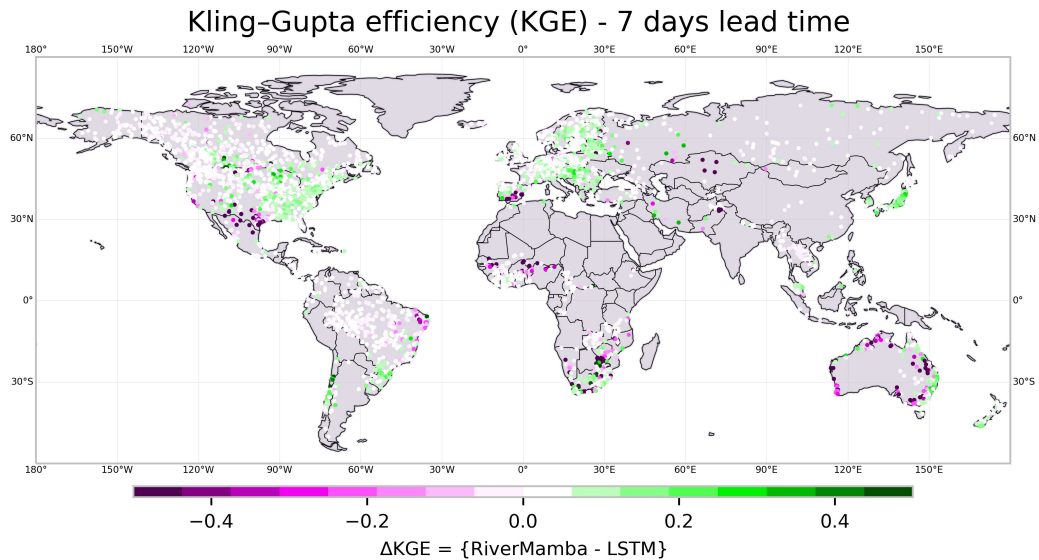


Figure 35: Comparison of KGE between RiverMamba and LSTM (Google) on GloFAS reanalysis (test set 2021-2024 temporally out-of-sample). RiverMamba improves over LSTM in 73% of the stations ($P=3364$).

Confusion matrix - 4 days lead time (P=3366)

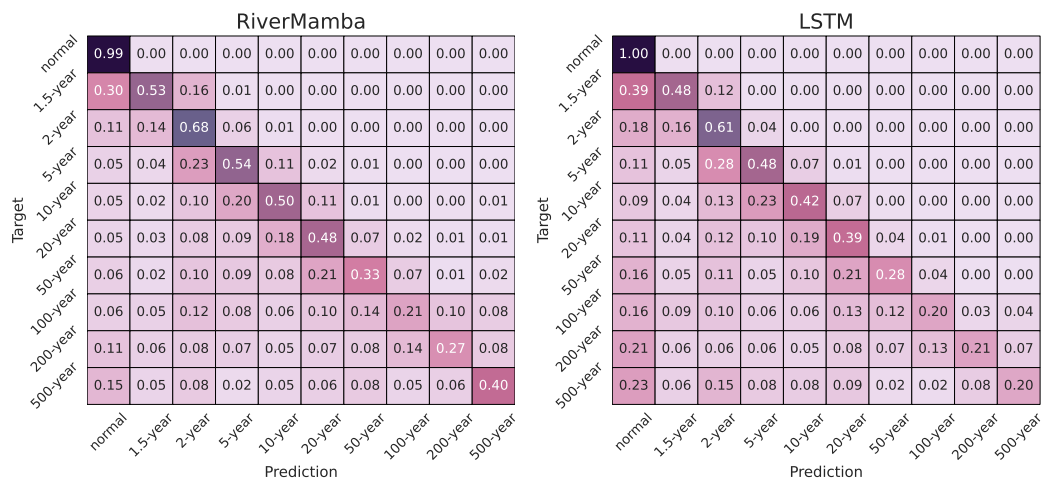


Figure 36: Comparison to LSTM (Google) on GloFAS reanalysis (test set 2021-2024 temporally out-of-sample).

J.4 Additional results on gauged GRDC

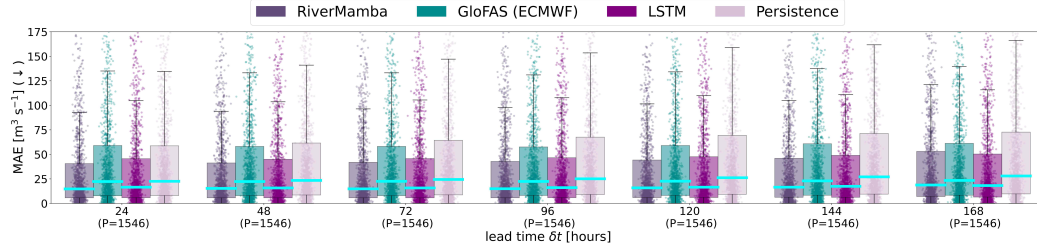


Figure 37: MAE of the river discharge forecasting with different lead time on GRDC observations (test set 2021-2023 temporally out-of-sample).

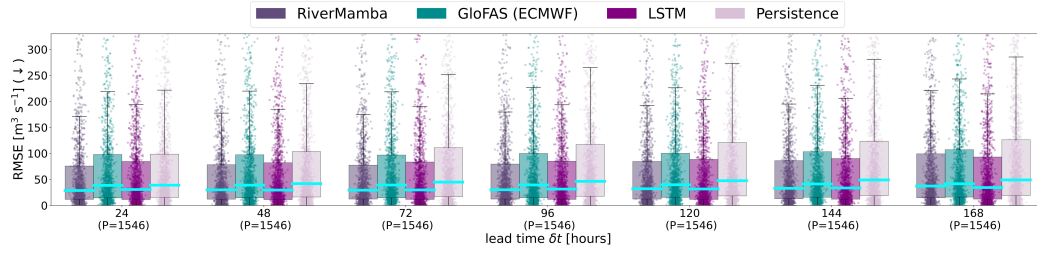


Figure 38: RMSE of the river discharge forecasting with different lead time on GRDC observations (test set 2021-2023 temporally out-of-sample).

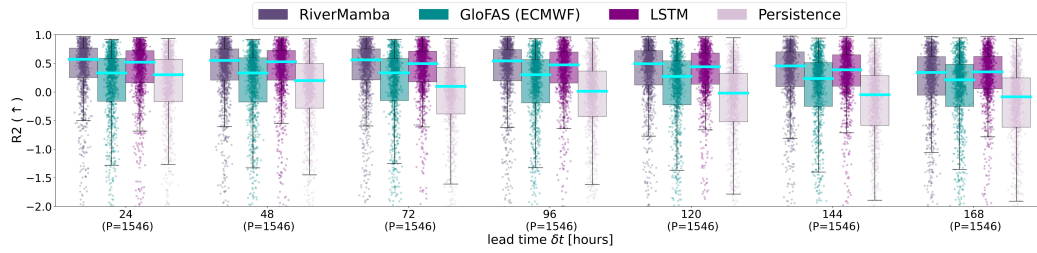


Figure 39: R^2 (NSE) of the river discharge forecasting with different lead time on GRDC observations (test set 2021-2023 temporally out-of-sample).

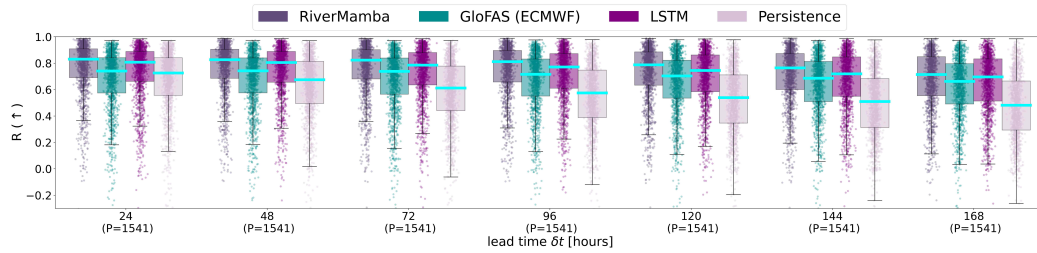


Figure 40: Pearson correlation (R) of the river discharge forecasting with different lead time on GRDC observations (test set 2021-2023 temporally out-of-sample).

Confusion matrix - 4 days lead time (P=1552)

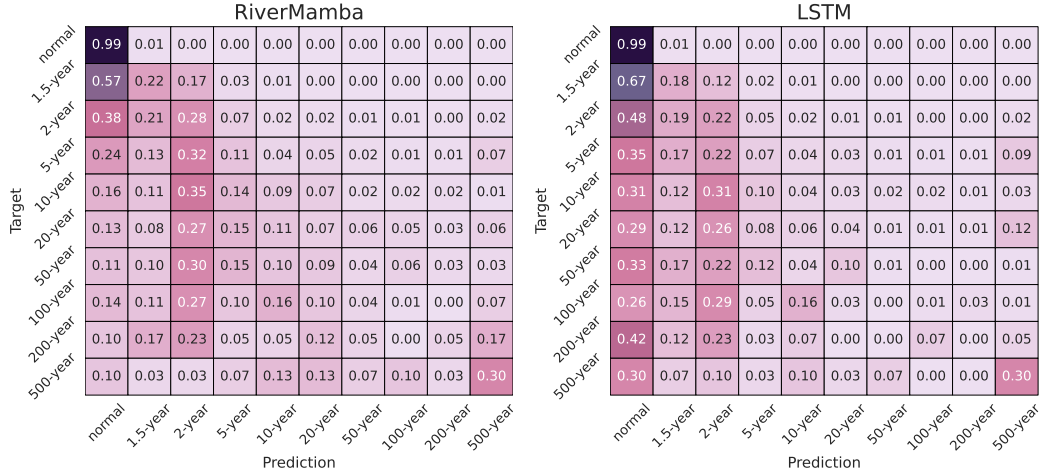


Figure 41: Comparison to LSTM (Google) on GRDC observations (test set 2021-2024 temporally out-of-sample).

Confusion matrix - 4 days lead time (P=1551)

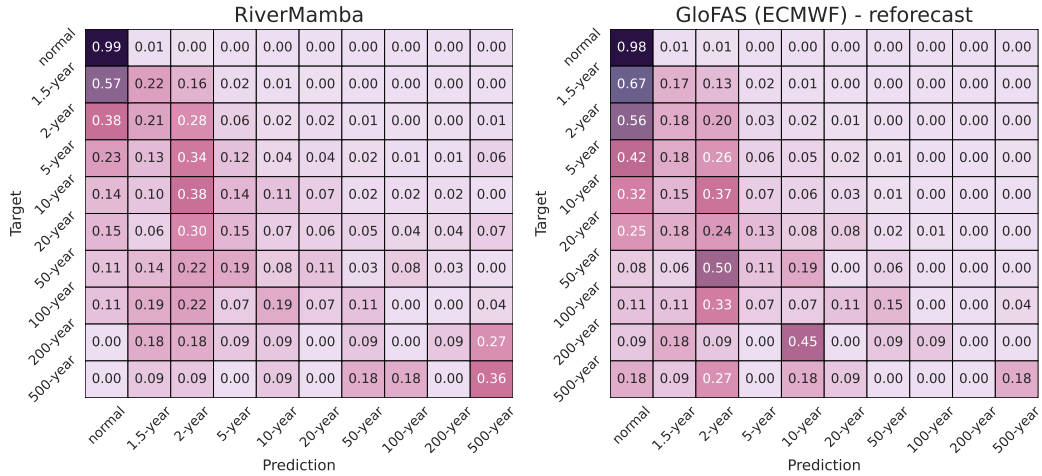


Figure 42: Comparison to GloFAS (ECMWF) - reforecast on GRDC observations (test set 2021-2023 temporally out-of-sample).



Figure 43: F1-score of flood forecasting for different return periods with lead time on GRDC observations (test set 2021-2023 temporally out-of-sample). Distribution quartiles are displayed in boxes, and the entire range excluding outliers is displayed in whiskers. The median score for the model is shown by the cyan line in the box.



Figure 44: Precision of flood forecasting for different return periods with lead time on GRDC observations (test set 2021-2023 temporally out-of-sample). Distribution quartiles are displayed in boxes, and the entire range excluding outliers is displayed in whiskers. The median score for the model is shown by the cyan line in the box.



Figure 45: Recall of flood forecasting for different return periods with lead time on GRDC observations (test set 2021-2023 temporally out-of-sample). Distribution quartiles are displayed in boxes, and the entire range excluding outliers is displayed in whiskers. The median score for the model is shown by the cyan line in the box.



Figure 46: F1-score of flood forecasting for different lead time with return periods (1.5 - 50 years) on GRDC observations (test set 2021-2023 temporally out-of-sample). Distribution quartiles are displayed in boxes, and the entire range excluding outliers is displayed in whiskers. The median score for the model is shown by the cyan line in the box.

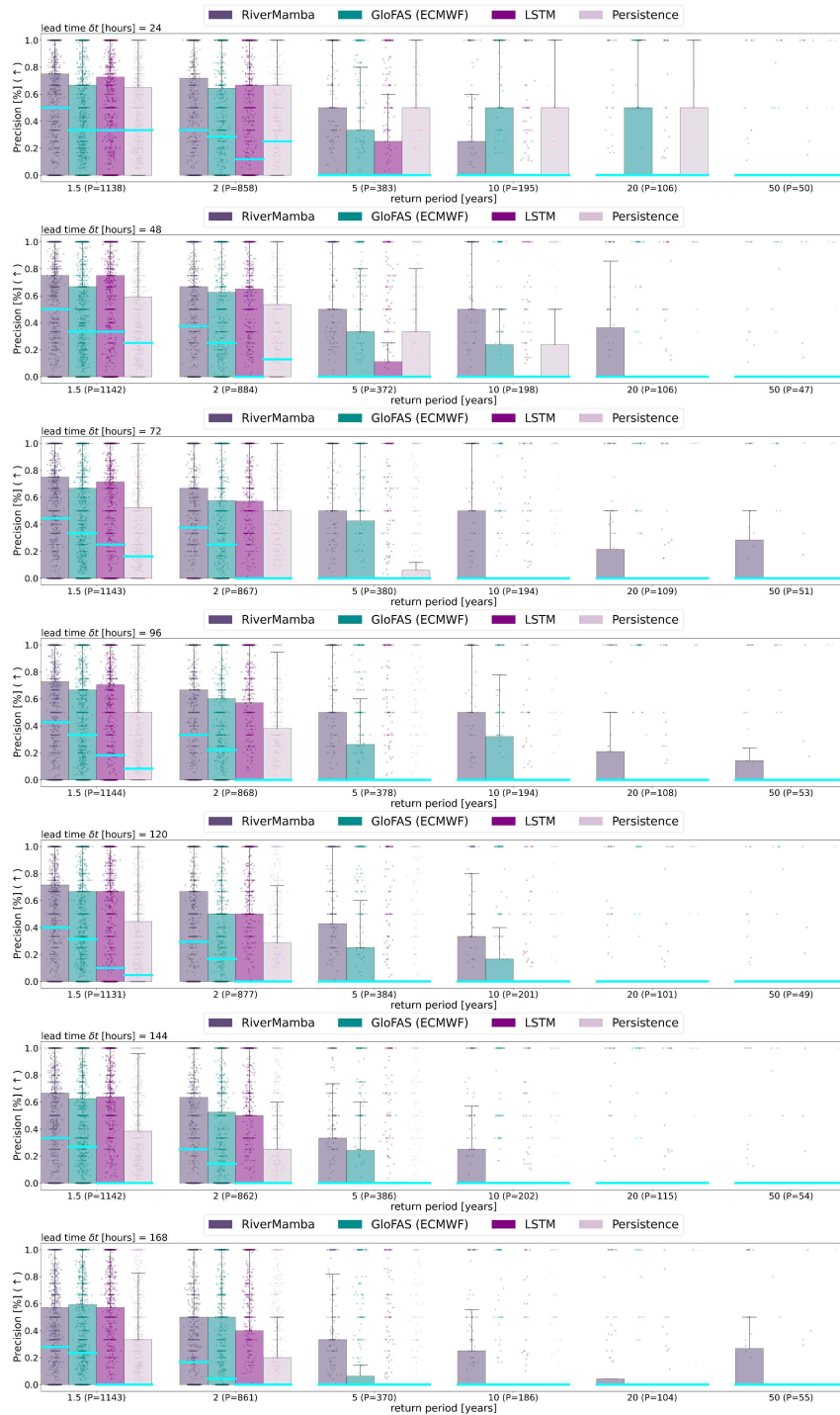


Figure 47: Precision of flood forecasting for different lead time with return periods (1.5 - 50 years) on GRDC observations (test set 2021-2023 temporally out-of-sample). Distribution quartiles are displayed in boxes, and the entire range excluding outliers is displayed in whiskers. The median score for the model is shown by the cyan line in the box.

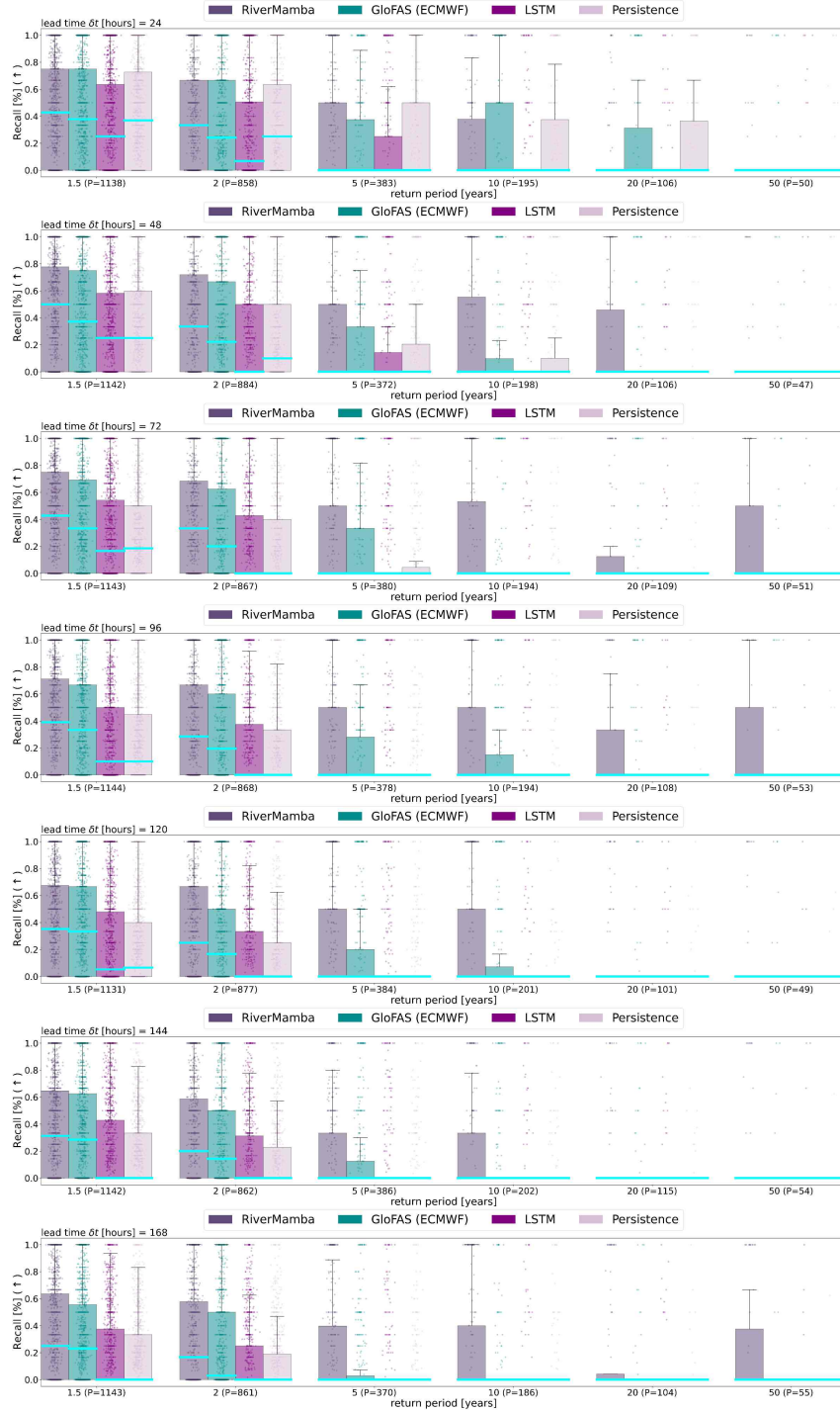


Figure 48: Recall of flood forecasting for different lead time with return periods (1.5 - 50 years) on GRDC observations (test set 2021-2023 temporally out-of-sample). Distribution quartiles are displayed in boxes, and the entire range excluding outliers is displayed in whiskers. The median score for the model is shown by the cyan line in the box.

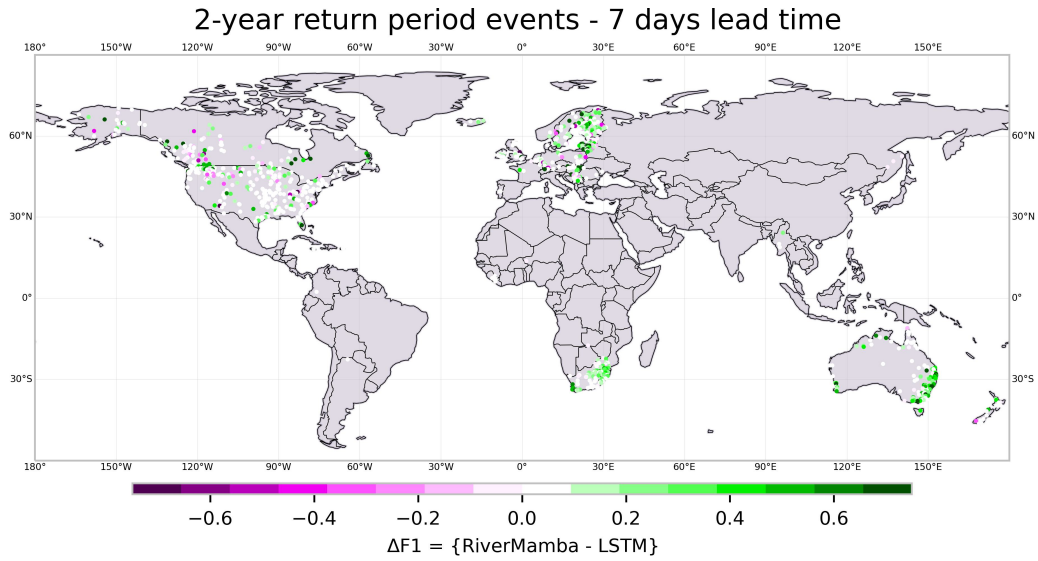


Figure 49: Comparison of F1-score between RiverMamba and LSTM (Google) on GRDC observations for the 2-year return period events (test set 2021-2023 temporally out-of-sample). RiverMamba improves over LSTM in 42% of the stations (P=861) and is better or equally better in 86% of the stations.

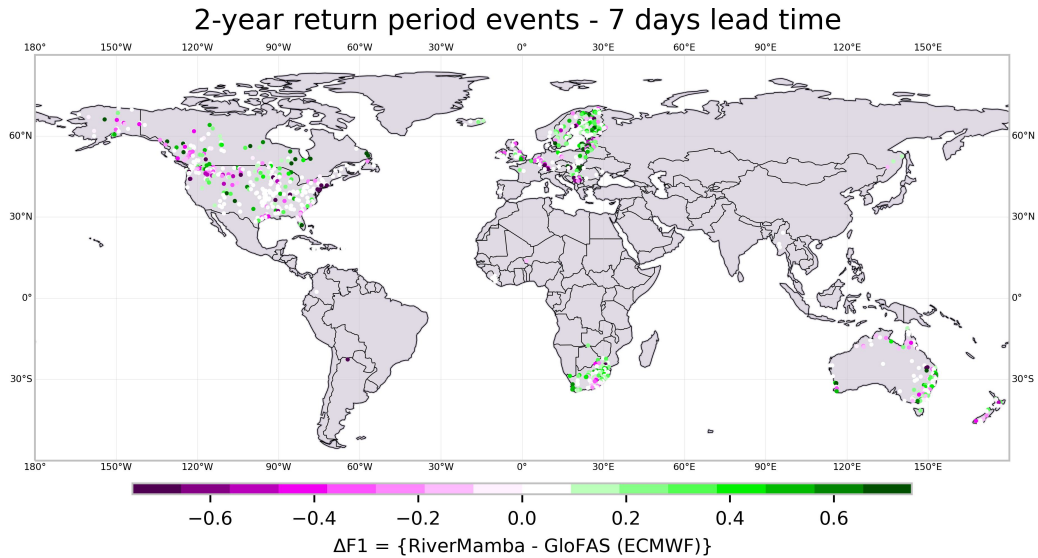


Figure 50: Comparison of F1-score between RiverMamba and GloFAS reforecast on GRDC observations for the 2-year return period events (test set 2021-2023 temporally out-of-sample). RiverMamba improves over GloFAS reforecast in 38% of the stations (P=861) and is better or equally better in 73% of the stations.

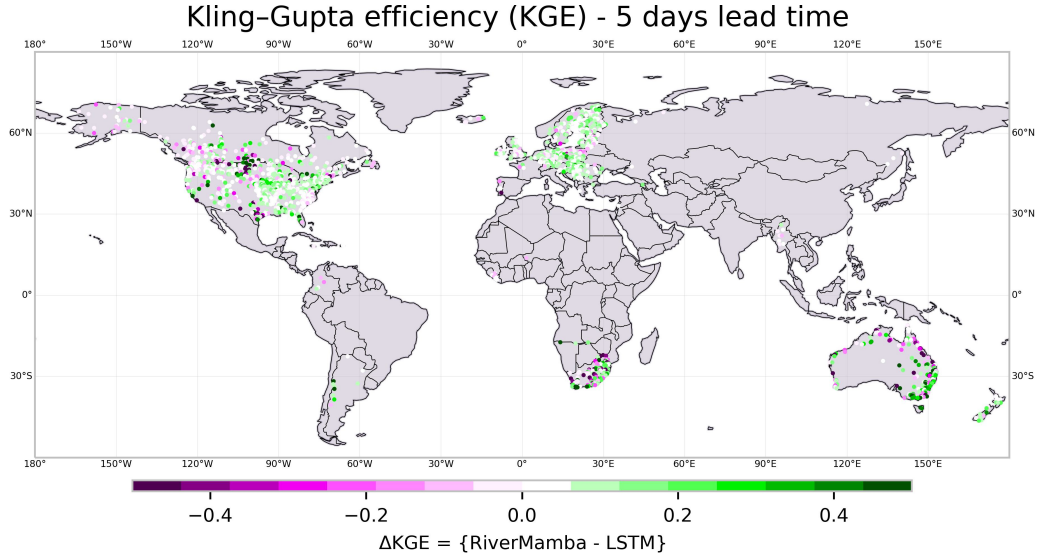


Figure 51: Comparison of KGE between RiverMamba and LSTM (Google) on GloFAS reanalysis (test set 2021-2023 temporally out-of-sample). RiverMamba improves over LSTM in 68% of the stations (P=1542).

J.5 Comparison to operational GloFAS forecast on gauged GRDC

Here, we compare to the archival operational forecast from GloFAS ECMWF (Sec. G.4). This is different from the GloFAS reforecast and gives a more realistic assessment of the physics-based model.

Table 20: Results on GRDC gauged stations. (\pm) denotes the standard deviation for 3 runs.

Test (2023-2024)				
Model	MAE (\downarrow)	R2 (\uparrow)	KGE (\uparrow)	F1-score (\uparrow)
GloFAS* [16]	65.35	-0.6261	04.39	17.95
LSTM [24]	53.07 \pm 0.39	-0.0516 \pm 0.0056	31.47 \pm 0.26	11.20 \pm 0.65
RiverMamba	49.32\pm0.18	0.0118\pm0.0131	38.21\pm0.76	23.58\pm2.11

*GloFAS operational forecast

J.6 Case studies of extreme flood events

J.6.1 2021 Western Europe flood

In this section, we present the daily river discharge at a gauge station on the Sauer River—located at the border of Germany, France, and Luxembourg—for the year 2021. Shown is the the river discharge signal as predicted by RiverMamba, LSTM, and GloFAS reanalysis, and compared against GRDC observations. Particular attention is given to the extreme flood event in July 2021 [14, 113], highlighted by the grey-shaded area in Fig.53. To illustrate the meteorological drivers of this flood, we also show 7-day precipitation from ERA5 reanalysis and ECMWF HRES forecasts in Fig.52.

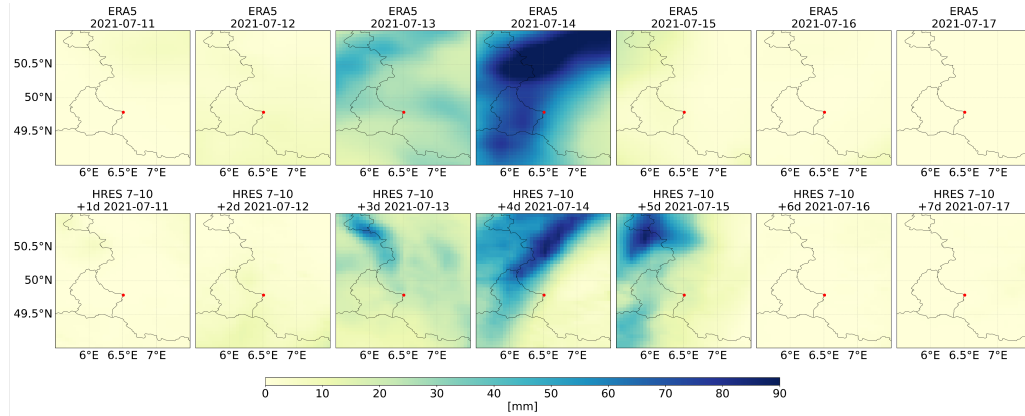


Figure 52: Daily total precipitation from 2021-07-11 to 2021-07-17 during the 2021 flood event in the target domain. First row shows precipitation as it simulated by ERA5 Reanalysis and second row is the ECMWF HRES forecast issued at 2021-07-10 with 7-day lead time. The red dot is the location of the river discharge gauge station.

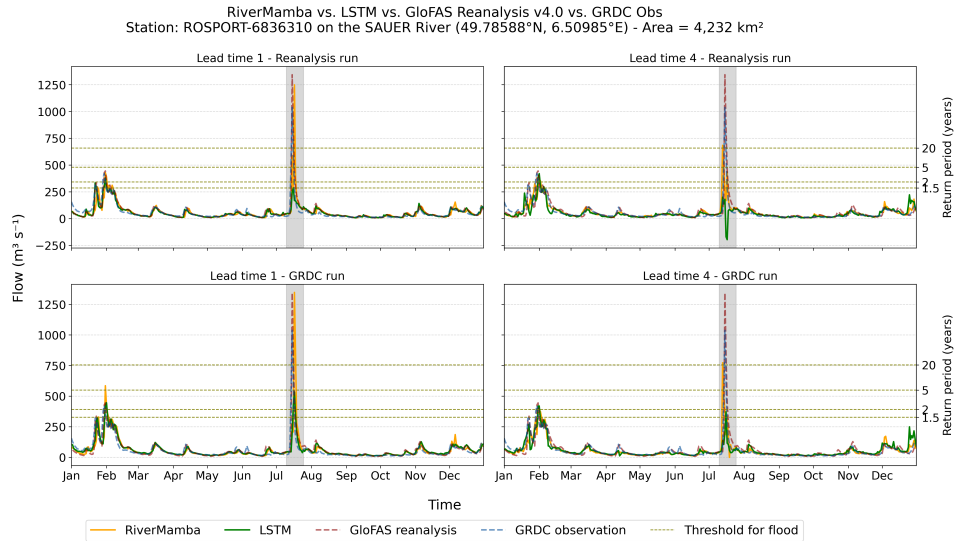


Figure 53: River discharge of the Sauer river in 2021 for RiverMamba (orange), LSTM (green), GloFAS reanalysis (dashed red), and GRDC observation (dashed green). The grey shaded area highlights the 2021 Germany flood between July 10 to July 20. The olive dashed lines represent the 1.5, 2, 5, and 20-year return periods calculated over reanalysis and GRDC observation data, respectively.

J.6.2 2024 Southeast Europe floods

In the following sections, we compare the daily flood severity map from GloFAS reanalysis as a ground truth and RiverMamba model at big flood events with different causes in 2024 and from different places around the Earth. These maps are usually used in the operational flood forecast service like GloFAS to provide a quick overview of the ongoing and upcoming flood events. As shown from these flood severity maps, RiverMamba can provide useful flood risk information at high spatial resolution to support decision-making. To the best of our knowledge, RiverMamba is the first AI model to demonstrate strong performance in predicting flood return periods globally under varying climate conditions at 5 km resolution across Europe, the USA, Africa, and China. This further demonstrates its potential as a valuable component of operational flood early warning systems. It is important to note that the quality of the ECMWF HRES data driving the forecast is a key factor influencing RiverMamba performance.

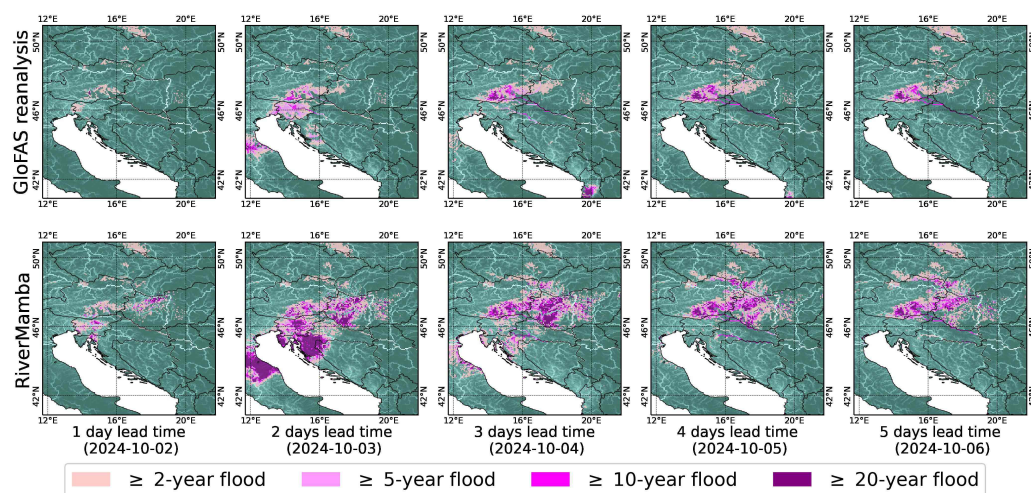


Figure 54: Comparison between GloFAS reanalysis (top, used as reference) and RiverMamba forecast (bottom) during the Southeast European flood in October 2024. Shown are flood severity maps at 5-km resolution where each panel shows flood extent at different lead times from 1 to 5 days.

J.6.3 2024 Central European floods

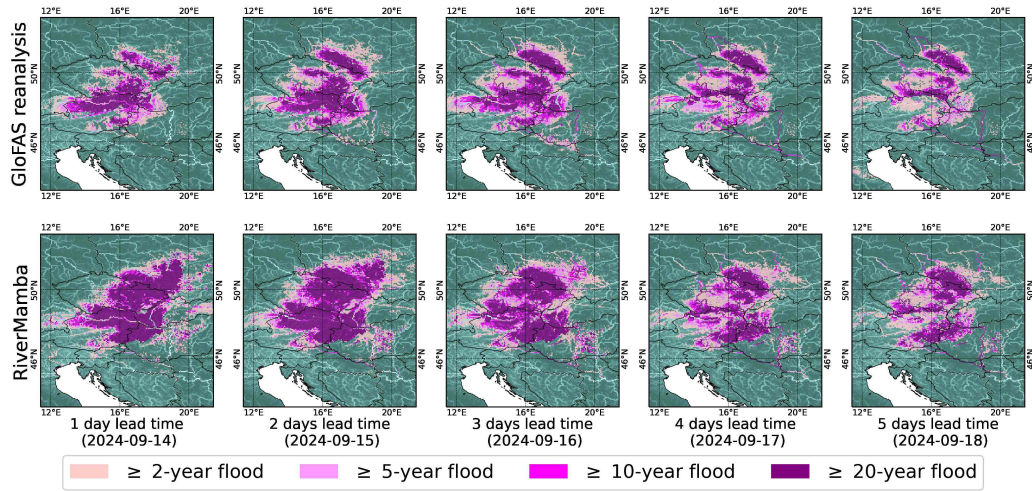


Figure 55: Comparison between GloFAS reanalysis (top, used as reference) and RiverMamba forecast (bottom) during the Central European floods event in 2024 [114]. In September 2024, Storm Boris brought record-breaking rainfall to Central Europe, causing devastating floods across Austria, the Czech Republic, Poland, Romania, Slovakia, Germany, and Hungary. Studies indicate that climate change doubled the likelihood and increased the intensity of such extreme rainfall events, highlighting the growing impact of global warming on severe weather patterns. Shown are flood severity maps at 5-km resolution where each panel shows flood extent at different lead times from 1 to 5 days.

J.6.4 2024 Spanish floods

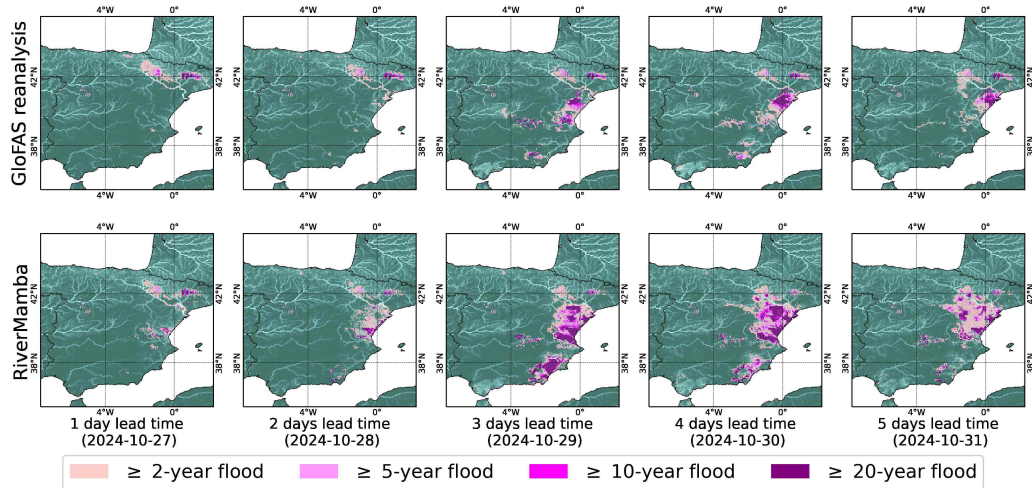


Figure 56: Comparison between GloFAS reanalysis (top, used as reference) and RiverMamba forecast (bottom) during the Spanish flood event in October 2024. The flood event primarily affecting the Valencia region, was caused by a cold drop (DANA) weather system intensified by climate change. Shown are flood severity maps at 5-km resolution where each panel shows flood extent at different lead times from 1 to 5 days.

J.6.5 2024 Saarland Germany flood

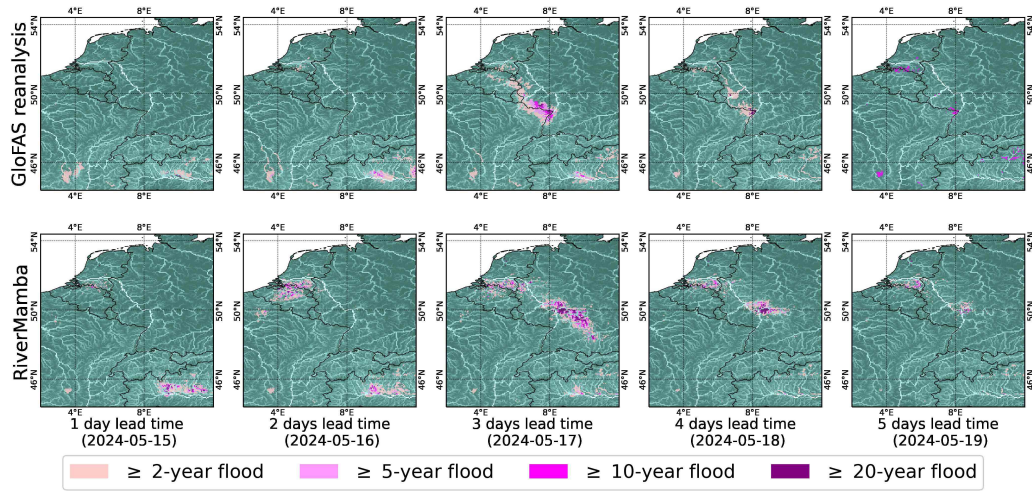


Figure 57: Comparison between GloFAS reanalysis (top, used as reference) and RiverMamba forecast (bottom) during the Saarland Germany flood event in May 2024. It was caused by thunderstorms and extreme rainfall, resulting in deadly floods and landslides across Saarland and Rheinland-Pfalz. However, RiverMamba predicted this flood event at a nearby location in Saarland, and the reason could be attributed to the inaccurate real-time ECMWF HRES forecast that drives the flood forecasting. Shown are flood severity maps at 5-km resolution where each panel shows flood extent at different lead times from 1 to 5 days.

J.6.6 2024 Kenya-Tanzania flood

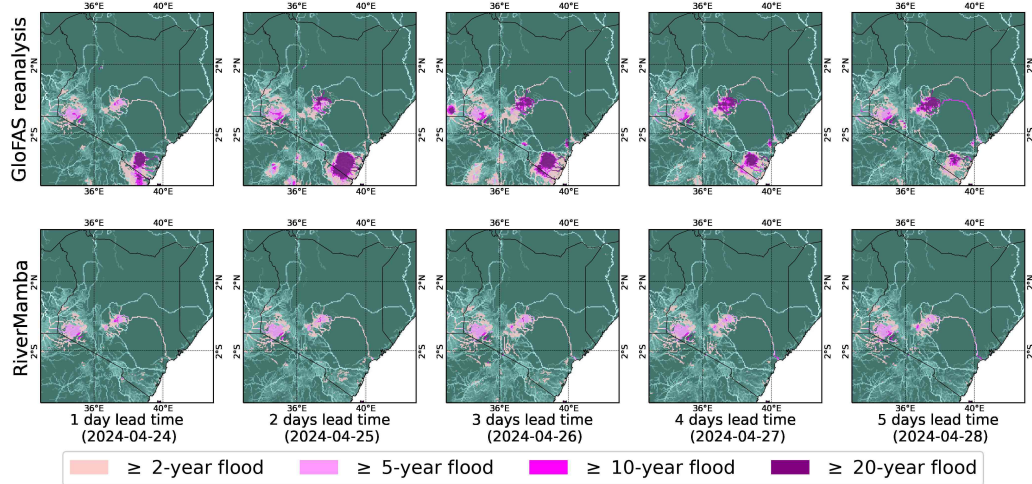


Figure 58: Comparison between GloFAS reanalysis (top, used as reference) and RiverMamba forecast (bottom) during the Kenya-Tanzania flood event in April 2024. This was the consequence of a combination of El Niño and a positive Indian Ocean Dipole, resulting in deaths, widespread displacement, and significant infrastructure damage. Shown are flood severity maps at 5-km resolution where each panel shows flood extent at different lead times from 1 to 5 days. Here points with less than $1 \text{ m}^3/\text{s}$ discharge have been removed to erase artifacts on desert grids.

J.6.7 2024 California flood

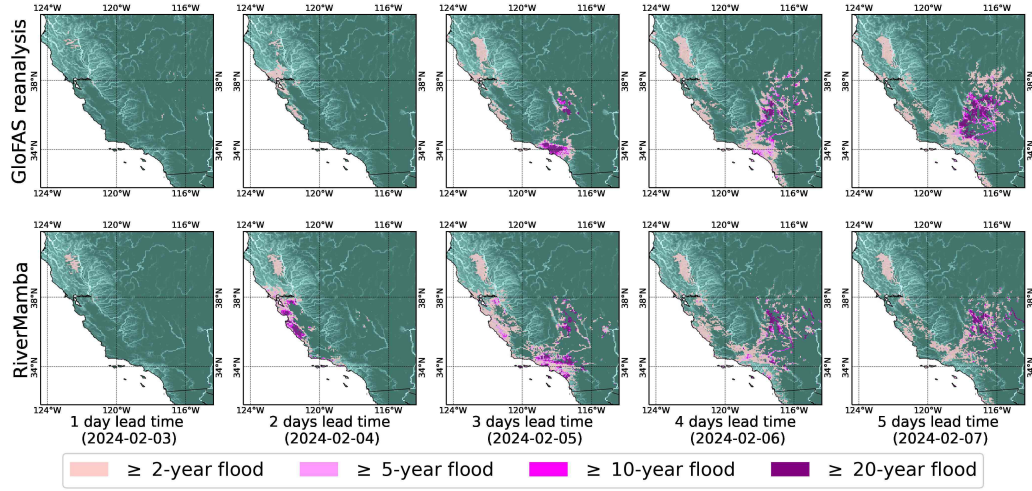


Figure 59: Comparison between GloFAS reanalysis (top, used as reference) and RiverMamba forecast (bottom) during the California, USA flood in February 2024. It was caused by two powerful atmospheric rivers. Shown are flood severity maps at 5-km resolution where each panel shows flood extent at different lead times from 1 to 5 days. Here points with less than $0.01 \text{ m}^3/\text{s}$ discharge have been removed to erase artifacts on desert grids.

J.6.8 2024 Central-South China floods

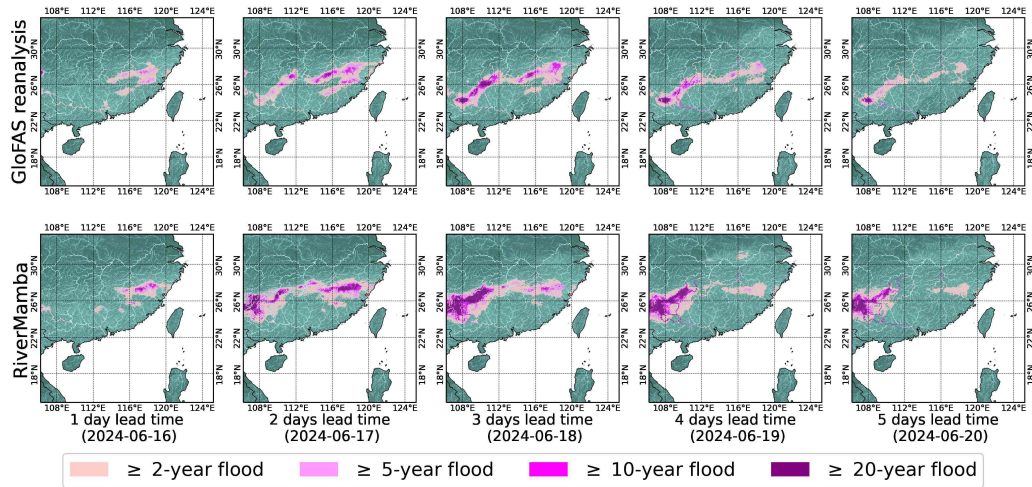


Figure 60: Comparison between GloFAS reanalysis (top, used as reference) and RiverMamba forecast (bottom) during the Central-South China flood event in June 2024 due to unprecedented rainfall. Shown are flood severity maps at 5-km resolution where each panel shows flood extent at different lead times from 1 to 5 days.

K Code and data availability

The code of RiverMamba, processing the data, and evaluation will be made publicly available upon publication. Note that we are not allowed to distribute data like GRDC data, but we will provide instructions how the data can be obtained. The data that has been used is available for researchers after signing a license agreement with the owner of the data.

L Broader impacts

Extreme flood events, characterized by longer return periods, are expected to become more frequent and intense due to climate change. Traditional hydrology models often struggle to accurately predict such events. To improve flood detection, it is crucial to develop computationally efficient and precise deep learning models capable of forecasting key hydrological variables, such as river discharge. In this study, we demonstrated the potential of RiverMamba for predicting extreme riverine floods and in Appendix Sec. J.6, we presented case studies for extreme flood events. We see this as the primary motivation for developing RiverMamba. However, it is important to acknowledge that early warning systems may sometimes fail, leading to inaccurate forecasts. This limitation should be considered when deploying early warning systems.

References

- [89] L. Alfieri, P. Burek, E. Dutra, B. Krzeminski, D. Muraro, J. Thielen, and F. Pappenberger. Glofas - global ensemble streamflow forecasting and flood early warning. *Hydrology and Earth System Sciences*, 17(3):1161–1175, 2013.
- [90] S. Harrigan, E. Zsoter, L. Alfieri, C. Prudhomme, P. Salamon, F. Wetterhall, C. Barnard, H. Cloke, and F. Pappenberger. Glofas-era5 operational global river discharge reanalysis 1979–present. *Earth System Science Data*, 12(3):2043–2060, 2020.
- [91] Gianpaolo Balsamo, Anton Beljaars, Klaus Scipal, Pedro Viterbo, Bart van den Hurk, Martin Hirschi, and Alan K. Betts. A revised hydrology for the ecmwf model: Verification from field site to terrestrial water storage and impact in the integrated forecast system. *Journal of Hydrometeorology*, 10(3):623 – 643, 2009.
- [92] J. M. Van Der Knijff, J. Younis, and A. P. J. De Roo and. Lisflood: a gis-based distributed model for river basin scale water balance and flood simulation. *International Journal of Geographical Information Science*, 24(2):189–212, 2010.
- [93] F. Dottori, M. Kalas, P. Salamon, A. Bianchi, L. Alfieri, and L. Feyen. An operational procedure for rapid flood risk assessment in europe. *Natural Hazards and Earth System Sciences*, 17(7):1111–1126, 2017.
- [94] Grey Nearing, Deborah Cohen, Vusumuzi Dube, Martin Gauch, Oren Gilon, Shaun Harrigan, Avinatan Hassidim, Daniel Klotz, Frederik Kratzert, Asher Metzger, et al. Global prediction of extreme floods in ungauged watersheds. *Nature*, 627(8004):559–563, 2024.
- [95] S. Harrigan, E. Zsoter, H. Cloke, P. Salamon, and C. Prudhomme. Daily ensemble river discharge reforecasts and real-time forecasts from the operational global flood awareness system. *Hydrology and Earth System Sciences*, 27(1):1–19, 2023.
- [96] J. Muñoz Sabater, E. Dutra, A. Agustí-Panareda, C. Albergel, G. Arduini, G. Balsamo, S. Boussetta, M. Choulga, S. Harrigan, H. Hersbach, B. Martens, D. G. Miralles, M. Piles, N. J. Rodríguez-Fernández, E. Zsoter, C. Buontempo, and J.-N. Thépaut. Era5-land: a state-of-the-art global reanalysis dataset for land applications. *Earth System Science Data*, 13(9):4349–4383, 2021.
- [97] Jiawei Zhuang, raphael dussin, André Jüling, and Stephan Rasp. JiaweiZhuang/xESMF: v0.3.0 Adding ESMF.LocStream capabilities, March 2020.
- [98] Pingping Xie, M Chen, and W Shi. Cpc unified gauge-based analysis of global daily precipitation. In *Preprints, 24th Conf. on Hydrology, Atlanta, GA, Amer. Meteor. Soc.*, volume 2, 2010.
- [99] Pingping Xie, Mingyue Chen, Song Yang, Akiyo Yatagai, Tadahiro Hayasaka, Yoshihiro Fukushima, and Changming Liu. A gauge-based analysis of daily precipitation over east asia. *Journal of Hydrometeorology*, 8(3):607–626, 2007.
- [100] Mingyue Chen, Wei Shi, Pingping Xie, Viviane BS Silva, Vernon E Kousky, R Wayne Higgins, and John E Janowiak. Assessing objective techniques for gauge-based analyses of global daily precipitation. *Journal of Geophysical Research: Atmospheres*, 113(D4), 2008.
- [101] M. Choulga, F. Moschini, C. Mazzetti, S. Grimaldi, J. Disperati, H. Beck, P. Salamon, and C. Prudhomme. Technical note: Surface fields for global environmental modelling. *Hydrology and Earth System Sciences*, 28(13):2991–3036, 2024.
- [102] Bernhard Lehner and Günther Grill. Global river hydrography and network routing: baseline data and new approaches to study the world’s large river systems. *Hydrological Processes*, 27(15):2171–2186, 2013.
- [103] Simon Linke, Bernhard Lehner, Camille Ouellet Dallaire, Joseph Ariwi, Günther Grill, Mira Anand, Penny Beames, Vicente Burchard-Levine, Sally Maxwell, Hana Moidu, et al. Global hydro-environmental sub-basin and river reach characteristics at high spatial resolution. *Scientific data*, 6(1):283, 2019.
- [104] Martin Gauch, Frederik Kratzert, Oren Gilon, Hoshin Gupta, Juliane Mai, Grey Nearing, Bryan Tolson, Sepp Hochreiter, and Daniel Klotz. In defense of metrics: Metrics sufficiently encode typical human preferences regarding hydrological model performance. *Water Resources Research*, 59(6):e2022WR033918, 2023. e2022WR033918 2022WR033918.
- [105] Tri Dao, Dan Fu, Stefano Ermon, Atri Rudra, and Christopher Ré. Flashattention: Fast and memory-efficient exact attention with io-awareness. *Advances in neural information processing systems*, 35:16344–16359, 2022.

- [106] Tri Dao. FlashAttention-2: Faster attention with better parallelism and work partitioning. In *International Conference on Learning Representations (ICLR)*, 2024.
- [107] Tri Dao and Albert Gu. Transformers are SSMS: Generalized models and efficient algorithms through structured state space duality. In *International Conference on Machine Learning (ICML)*, 2024.
- [108] Xiaoyang Wu, Li Jiang, Peng-Shuai Wang, Zhijian Liu, Xihui Liu, Yu Qiao, Wanli Ouyang, Tong He, and Hengshuang Zhao. Point transformer v3: Simpler faster stronger. In *Proceedings of the IEEE/CVF Conference on Computer Vision and Pattern Recognition (CVPR)*, pages 4840–4851, June 2024.
- [109] David Hilbert and David Hilbert. Über die stetige abbildung einer linie auf ein flächenstück. *Dritter Band: Analysis· Grundlagen der Mathematik· Physik Verschiedenes: Nebst Einer Lebensgeschichte*, pages 1–2, 1935.
- [110] Jian Zhang, Sei-ichiro Kamata, and Yoshifumi Ueshige. A pseudo-hilbert scan algorithm for arbitrarily-sized rectangle region. In Nanning Zheng, Xiaoyi Jiang, and Xuguang Lan, editors, *Advances in Machine Vision, Image Processing, and Pattern Analysis*, pages 290–299, Berlin, Heidelberg, 2006. Springer Berlin Heidelberg.
- [111] Grey Nearing. Global prediction of extreme floods in ungauged watersheds, December 2023.
- [112] Husain Najafi, Pallav Kumar Shrestha, Oldrich Rakovec, Heiko Apel, Sergiy Vorogushyn, Rohini Kumar, Stephan Thober, Bruno Merz, and Luis Samaniego. High-resolution impact-based early warning system for riverine flooding. *Nature communications*, 15(1):3726, 2024.
- [113] Magdalena Kracheletz, Ziyu Liu, Anne Springer, Jürgen Kusche, and Petra Friederichs. Would the 2021 western europe flood event be visible in satellite gravimetry? *Journal of Geophysical Research: Atmospheres*, 130(3):e2024JD042190, 2025. e2024JD042190 2024JD042190.
- [114] C Hauer, M Paster, U Pulg, T Ofenböck, and H Habersack. Critical flows at the wien river during the 1000-years event in september 2024—causes, consequences and possible management options for urban river flood management. *Natural Hazards*, pages 1–13, 2025.